2018

# The structure of a perturbed vortex and its interaction with a wing

Greg Fishman
*Lehigh University*

# THE STRUCTURE OF A PERTURBED VORTEX AND ITS INTERACTION WITH A WING

by

Gregory Fishman

Presented to the Graduate Research Committee

Of Lehigh University

In Candidacy for the Degree of

Doctor of Philosophy

in

Mechanical Engineering

Lehigh University

May, 2018

**REPORT ON THE DOCTORAL DISSERTATION EXAMINATION**

Approved and recommended for acceptance as a dissertation in fulfillment of the requirements for the degree of Doctor of Philosophy.

_____

Date

_____

Donald Rockwell

Dissertation Advisor

_____

Accepted Date

Committee Members:

_____

Professor Donald Rockwell

_____

Professor Justin Jaworski

_____

Professor Alparslan Oztekin

_____

Professor Daniel Ou-Yang

*To Nicole*

## ACKNOWLEDGEMENTS

There are a large number of people that I have to thank, without them this would not have been possible. First of all, I would like to acknowledge my utmost appreciation for my advisor, Dr. Donald Rockwell. Professor Rockwell has provided me with immeasurable guidance and wisdom throughout my study and working with him has been a great experience. His dedication and collaboration has helped this project immensely. I have learned an incredible amount from him that I know will serve me well in my future endeavors.

I would also like to thank the members of my doctoral committee, Dr. Justin Jaworski, Dr. Alparslan Oztekin and Dr. Daniel Ou-Yang for their guidance, advice and time throughout my research experience.

I would like to thank my fellow lab mates Dr. Maxwell Wolfinger and Dr. Matthew Bross for their support throughout the PhD process. Their insights have helped shape the course of this research project. I would also like to thank Dr. Chris McKenna for his friendship, collaboration and keen insights. It was a pleasure to work so closely with him.

This work would not have been possible without the help of the people of the Mechanical Engineering and Mechanics department. In particular, the construction of my experimental apparatus would not have been possible without the technical expertise

from the skilled staff of the machine shop. I would like to thank Mr. Richard Towne, Mr. James Bunderla and Mr. Eli Towne for their hard work and support towards the completion of this project. I would also like to thank the administrative support of Mrs. JoAnn Casciano, Ms. Allison Marsteller, Ms. Brianne Lisk, Mrs. Jennifer R. Smith and Mrs. Barbara McGuire.

I am very thankful for my friends and family who have kept me motivated throughout my time in graduate school. Most of all, I would like to thank Nicole for her constant support, positivity and motivation throughout this process, despite only seeing her on weekends. I cannot thank her enough and I couldn't have done this without her.

## TABLE OF CONTENTS

**Pages**

## LIST OF FIGURES

**Pages**

## NOMENCLATURE

| | |
|---|---|
| $A$ | Displacement amplitude |
| $a^{-1}$ | Time scale |
| $AR$ | Aspect ratio |
| $b$ | Span length |
| $C$ | Chord length |
| $C_{fw}$ | Chord length |
| $c_\tau$ | Centroid constant |
| $d_\tau$ | Particle image diameter |
| $d_o$ | Vortex diameter |
| $d_r$ | Pixel pitch |
| $d_p$ | Particle diameter |
| $e$ | Grow factor |
| $e_r$ | Error ratio |
| $F$ | Focus |
| $f$ | Frequency |
| $f\#$ | f-number of camera lens |
| $M_o$ | Image magnification |
| $q$ | Swirl ratio |
| $Q$ | Q-criterion |
| $r_{1/2}$ | Radial half-width |
| $r_c$ | Corner radius of wing |
| $r_o$ | Vortex radius |
| $Re$ | Reynolds number |
| $SP$ | Saddle point |
| | Half saddle point |
| $St$ | Strouhal number |
| $t$ | Plate/wing thickness |
| | Time |
| $u$ | Streamwise component of velocity |
| $u_\theta$ | Azimuthal component of velocity |
| $U_\infty$ | Free-stream velocity |
| $v$ | Spanwise component of velocity |
| $\boldsymbol{V}$ | Three-dimensional velocity field |
| $V$ | Velocity magnitude |
| $w$ | Vertical component of velocity |
| $x$ | Coordinate in the streamwise direction |
| $x'$ | Distance from reference location |
| $x_M$ | Streamwise mirror location |
| $x_{LP}$ | Streamwise laser plane location |

| | |
|---|---|
| $\Delta x$ | Streamwise distance between two wings |
| $y$ | Coordinate in the spanwise direction |
| $\Delta y$ | Spanwise distance between two wings |
| $z$ | Coordinate in the vertical direction |

**Greek Symbols**

| | |
|---|---|
| $\alpha_o$ | Geometric angle of attack |
| $\alpha$ | Angle between the lens plane and the image plane |
| $\beta_o$ | Geometric angle of attack |
| $\Gamma$ | Circulation |
| $\Delta$ | Rate of change |
| $\delta z$ | Depth of field |
| $\theta$ | Angle between the lens plane and the object plane |
| | Stereo half angle |
| $\lambda$ | Wavelength |
| $\upsilon$ | Kinematic viscosity |
| $\sigma$ | Smoothing kernel |
| $\sigma_{\Delta X}$ | RMS random in-plane displacement error |
| $\sigma_u$ | RMS random in-plane velocity error |
| $\sigma_{\Delta Z}$ | RMS random out of plane displacement error |
| $\Phi$ | Phase angle |
| $\boldsymbol{\omega}$ | Three-dimensional vorticity field |
| $\omega_x$ | Streamwise component of vorticity |
| $\omega_y$ | Spanwise component of vorticity |
| $\omega_z$ | Vertical component of vorticity |
| $\omega_\theta$ | Azimuthal component of vorticity |

**Acronyms**

| | |
|---|---|
| CCD | Charge-Coupled Device |
| MAV | Micro aerial vehicle |
| PIV | Monoscopic Particle Image Velocimetry |
| RMS | Root Mean Square |
| SPIV | Stereoscopic Particle Image Velocimetry |

## ABSTRACT

The study of wingtip vortices and their evolution has been an important topic due to the wide range of applications where they occur. In the present investigation, the evolution of a vortex from an oscillating wing, as well as its subsequent interaction with a downstream (follower) flat plate (wing), is characterized using particle image velocimetry, which leads to patterns of velocity, vorticity, swirl ratio and streamlines on cross-flow planes along the undulating vortex formed from an isolated wing undergoing controlled oscillation. For the case where the undulating vortex impinges upon a downstream wing, similar crossflow representations are used to characterize the flow structure. Additionally, a reconstruction technique is utilized to provide volumetric, global patterns of the streamwise development of the unsteady vortex, as well as its interaction with, and distortion along a downstream plate.

The evolution of the vortex from an oscillating wing undergoing small amplitude perturbations shows large fluctuations of axial velocity deficit and circulation during the oscillation cycle. Correspondingly, large variations of swirl ratio occur and the onset of pronounced azimuthal vorticity arises. At a given cross-section of the vortex, the pattern of azimuthal vorticity moves around its axis in an ordered fashion as both it and the pattern of velocity defect increase in magnitude and scale. When the swirl ratio attains its minimum value during the oscillation cycle, and this value lies below the theoretically-established critical threshold for amplification of azimuthal modes, the magnitude and

scale of the pattern of azimuthal vorticity is maximized. Subsequent increase of the swirl ratio yields attenuation of the azimuthal vorticity. Onset of pronounced azimuthal vorticity when the swirl ratio decreases, involves rapid amplification, then disruption, of the axial vorticity fluctuation.

The onset and development of orbital motion of a trailing vortex from an oscillating wing has also been characterized; its response is frequency dependent. At low Strouhal number, the amplitude of the unidirectional excursion of the vortex remains essentially constant with streamwise distance and has a magnitude of the order of the amplitude of the wing oscillation. At moderate Strouhal number, the initial region of the vortex motion is unidirectional, but at larger streamwise distance, excursions of the vortex occur orthogonal to its initial unidirectional motion, thereby giving rise to an elliptical orbital trajectory oriented in the opposite direction to the circulation of the vortex. At high Strouhal number, the amplitude of the vortex undulation increases by nearly an order of magnitude with streamwise distance, and pronounced orbital motion of the vortex has the same sense as the vortex circulation at all streamwise distances. The genesis of orbital motion is small amplitude lateral motion of the forming vortex at the trailing edge of the wing during its controlled vertical motion; moreover, the phase shift of the vortex development relative to the wing motion is altered with respect to that at lower values of Strouhal number. Irrespective of the value of either the Strouhal number of excitation or the streamwise location along the undulating vortex, generic physical mechanisms occur. Changes in curvature along the vortex are closely related to changes

in the axial velocity deficit, axial vorticity and swirl ratio, as well as, the onset and attenuation of pronounced azimuthal vorticity.

Additionally, large time-dependent variations of the flow structure of the perturbed trailing vortex that impinges upon and develops along a flat plate located downstream are evident, relative to a steady vortex-wing interaction. The nature of the vortex-wing interaction is influenced by the spanwise location of vortex impingement on the wing and the time-dependent variations of the structure and position of the incident vortex. When the incident vortex is aligned with the tip of the wing, the upwash of the incident vortex gives rise to separation at the tip of the wing and an opposite-signed tip vortex is induced, thereby forming a dipole with the incident vortex. Contrary to the mode of the steady vortex dipole interaction with the wing, the dipole structure rotates around the tip of the wing in an ordered manner. Variations in the upwash of the incident vortex alter the strength of the induced vortex. When the incident vortex impinges inboard of the tip of the wing, it induces a vortex of same sign vorticity at the wingtip due to the downwash of the incident vortex, which causes separation at the tip. At the leading edge of the wing the incident vortex bifurcates and an induced vortex at the tip of the wing is evident. Moreover, vorticity of opposite sign, relative to that of the incident vortex, is evident across the wing surface during this bifurcation. It is also evident when the incident vortex is positioned above the wing. This occurs as a result of the gradient of spanwise velocity in the vertical direction; in other words, the change in spanwise velocity extending over the vertical distance from the surface of the wing to the center of the incident vortex.

# CHAPTER 1

# INTRODUCTION

## 1.1 MOTIVATION

The evolution of wingtip vortices has been a topic of considerable study due to their prevalence over a wide range of applications. An encounter with the wake of an aircraft can be hazardous for a following aircraft. On the other hand, controlled encounters with the wake of a preceding aircraft can offer enhanced aerodynamic performance, as seen in the formation flight of birds and aircraft. In other scenarios, a vortex from an upstream surface of an aircraft can impinge on a downstream structure, such as a fin or tail which can lead to undesired buffeting. In each of these examples, the unsteady nature of a vortex governs the flow physics of its interaction with a body. The focus of this dissertation is on the detailed analysis of the physics of unsteady vortices and their interactions with a wing.

## 1.2 OVERVIEW OF APPLICATIONS

Wingtip vortices play an important role in a wide variety of relevant applications. It is commonly known that aircraft produce vortices in their wake, as indicated in Figure

1.1. These vortices take considerable time to dissipate in a flow field and are susceptible to instability; this creates problems for air travel around the world. Transient encounters of subsequent aircraft with the wake of a preceding aircraft can result in unsteady loading and even loss of control of the aircraft. These hazardous situations restrict the throughput of airports globally, as the time between consecutive landings or takeoffs is limited by this effect, as described by Spalart (1998).

On the other hand, controlled encounter of a wingtip vortex with a downstream wing, shown in Figure 1.2, can offer aerodynamic benefits, resulting in energy savings. Birds and some aircraft are known for taking advantage of this concept. A variety of different formations are shown in Figure 1.3. A study by Weimerskirch et al. (2001) confirmed that pelicans flying in formation expended less overall energy, relative to a single pelican, by measuring their heart rates which are shown in Figure 1.4.

Furthermore, interactions of vortices from upstream structures that impinge on downstream structures are inherent in other practical flight scenarios; this includes blades in turbomachinery and rotorcraft, shown in Figure 1.5, as well as tails or fins of delta wing aircraft, shown in Figure 1.6. These potentially detrimental interactions can lead to buffeting of the structure, with the possibility of inducing resonance at the natural frequencies of the structural components of the aircraft, with the potential for structural failure.

For all of the foregoing applications, the unsteady flow physics of the vortex is associated with its spatial and temporal evolution, as well as its interaction with a

downstream body. The following sections review the literature pertaining to the physics of an unsteady vortex and its interaction with a secondary wing or aerodynamic surface.

## 1.3 FLOW STRUCTURE OF UNSTEADY VORTICES

Several investigations have provided valuable insight into the unsteady flow structure of a trailing vortex from a wing subjected to controlled motion. Moreover, there is considerable literature regarding the persistence of trailing vortices and the various classes of instability that can occur. The following section provides an overview of existing literature, with emphasis on the unsteady structure, including the onset of instabilities, of vortices from wings subjected to controlled motion.

### *1.3.1 Vortices from Oscillating Wings*

The unsteady evolution of a vortex from a wing or control surface subjected to controlled motion, in absence of a downstream follower wing, has been addressed in a wide range of investigations. Distributions of velocity, vorticity and circulation of a tip vortex from a pitching wing were characterized by Ramaprian & Zheng (1998) using laser Doppler velocimetry. They found that, at a streamwise location 0.7 chords downstream of the wing, the average trajectory and normalized circulation of the vortex displayed the same behavior as the vortex behind a stationary wing. Chang & Park (2000) used triple-hot-film probe measurements to analyze the near field of a trailing vortex behind a pitching wing and characterized hysteresis of velocity profiles and circulation.

Birch & Lee (2005) investigated the effect of perturbation frequency on the three-dimensional flow structure of a tip vortex behind a pitching wing for attached flow, light stall, and deep stall oscillations using a triple-hot-wire probe. They found that the azimuthal velocity profiles exhibited self-similar structure in the core of the vortex and were unaffected by the reduced frequency of the wing perturbation.

Trailing edge flaps or tabs have been utilized to alter the vortex structure from stationary or oscillating wings. Gerontakos & Lee (2006) employed an actuated trailing-edge flap across the entire span of a pitching wing in order to control the characteristics of the wingtip vortex, which was documented using a miniature triple hot-wire probe. The trailing edge flap effectively altered the strength, axial velocity and axial vorticity of the tip vortex. Similarly, a movable trailing edge tab was employed by Panagakos & Lee (2006) to control the structure of a tip vortex from a pitching wing using a triple hot-wire probe. Moreover, the tab significantly altered the position of the vortex. Lee (2007) investigated different amplitudes and velocity profiles of a vortex from a movable trailing edge tab using triple hot-wire probe measurements. Upward tab deflections were more effective in controlling the hysteresis of the vortex.

Recently, Garmann & Visbal (2016a), Garmann & Visbal (2016b) and Garmann & Visbal (2017) employed high-fidelity computations to investigate the flow structure of a tip vortex from a wing undergoing small amplitude, heaving oscillations. Figure 1.7 shows the flow structure of a vortex from a wing undergoing this type of oscillation, as depicted by Garmann & Visbal (2016b). The effects of oscillation frequency and amplitude were examined with emphasis on the formation of the vortex along the

wingtip. Oscillation of the wing induced large fluctuations of the vortex core structure along its tip, which persisted downstream into the wake. Enhanced separation and stretching along the wingtip occurred as a result of such fluctuations. This separation of the vortex from the wing is associated with the formation of spiraling substructures around the periphery of the vortex, which also persists into the wake, as shown in Figure 1.8. The vertical amplitude of the vortex trajectory was shown to increase considerably with increasing streamwise distance. Moreover, the vortex trajectory developed spanwise excursions that also increased in amplitude with streamwise distance. The rate of increase of the vertical and spanwise excursions depended on the parameters of the wing oscillation; namely, oscillations with the higher frequency and amplitude produced more rapid amplification.

When relatively large amplitude heaving or pitching motions of a wing occur, in contrast to the small amplitude wing perturbations of interest herein, the development of the flow structure along the wing is expected to influence the evolution of the tip vortices in the near wake region. Visbal (2011) employed high-fidelity numerical simulations to investigate the flow structure along a heaving flat plate. Spiraling undulations in the structure of the wingtip vortices were observed along the wing and into the wake. The wingtip vortices undergo breakdown and reformation over the course of the heaving cycle and are associated with the formation and transport of an arch-like vortex along the plane of symmetry of the wing.

Experimental investigations of the flow structure along plunging wings undergoing large amplitude or high frequency motion have been carried out by Yilmaz &

Rockwell (2010) using particle image velocimetry in conjunction with dye visualization. This investigation focuses primarily on the axial flow associated with the formation of the leading edge vortex which is found to reorient to form streamwise-oriented vortices along the wing. Due to the large scale motion of the wing, significant changes in the wingtip vortices occur. Cleaver et al. (2011) employed force measurements and particle image velocimetry to examine the effect of oscillation frequency on the flow structure of along a plunging wing. In general, small-amplitude wing oscillations effectively enhanced the lift to drag ratio of the wing. Different modes of flow structure were observed as a function of Strouhal number. Effects of planform geometry on plunging wings were analyzed by Calderon et al. (2013) using volumetric three-dimensional velocimetry. The formation and evolution of the leading edge vortex was found to be dependent on the Strouhal number; at higher Strouhal numbers the vortex remains near the tip of the wing. Furthermore, formation of a tip vortex ring is evident at high Strouhal number.

### *1.3.2 Vortex Instabilities*

There is a large body of literature that details the unsteady nature of a pair of vortices or a single vortex in relation to instability mechanisms and their evolution. For a pair of vortices, two major classes of instability have been studied extensively, commonly known as long-wave instability (or Crow instability) and short-wave instability (or elliptical instability). Other hydrodynamic instabilities can also occur in a vortex, which are independent of external influences. This section will provide an overview of the major findings related to these classes of instability.

The long-wave Crow instability occurs when a pair of counter-rotating vortices, which are typically found in the wake of aircraft, are subjected to a strain field as described by Crow (1970). Figure 1.9 shows the time development of the vortex wake from a B-47 described in Crow (1970). Small disturbances cause displacement perturbations to form and amplify. Eventually, the amplitudes of the vortices and become sufficiently large and connect to form vortex rings and dissipate further downstream. This class of instability cannot develop in the case of co-rotating vortices as shown by Bristol et al. (2004). However, a pair of co-rotating vortices can develop a short-wave instability. Short-wave instabilities arise in the presence of a strain field that resonates with the rotating vortex flow field, as indicated by Kerswell (2002). Figure 1.10 from Roy et al. (2011) shows flow visualization of an elliptical instability within a vortex. Wavelengths of elliptical or short-wave instabilities can be on the order of the vortex diameter, which is considerably smaller than the previously described long-wave instability.

Other instabilities of a vortex can arise, apart from the influence of an external strain field. Leibovich & Stewartson (1983) addressed the stability of a Batchelor (1964) (columnar) vortex with respect to three-dimensional perturbations. Their theory employed asymptotic instability analysis that led to a stability criterion related to the swirl ratio $q$ of the vortex, which relates the peak swirl (azimuthal) velocity and the defect of axial velocity. According to Jacquin & Pantano (2002), it is defined as $q = \Gamma/2\pi r_o \Delta u \approx 1.576 V_o/\Delta u$ where $\Gamma$ is circulation, $r_o$ is the vortex radius, $V_o$ is the maximum swirl component of velocity and $\Delta u = U_\infty - u_{min}$ is the deficit of axial velocity in the vortex core. They showed that for small values of q, the vortex is unstable with respect to

azimuthal wavenumbers. Specifically, the amplification of small wavelength perturbations is precluded when $q \geq \sqrt{2}$. The consequence is that, below this threshold value of $q$, severe destabilization can occur for each of the azimuthal modes.

Viola et al. (2016) reviewed the evolution of investigations since the landmark contribution of Leibovich & Stewartson (1983), including Mayer & Powell (1992), Delbende et al. (1998) and Eckhoff (1984). Viola et al (2016) also summarized advances on the topics of viscous core modes and the occurrence of absolute instabilities. In general, it is important to determine whether there is potential for the occurrence of an absolute instability (AI) as opposed to a convective instability (CI). In this regard, the work of Olendraru & Sellier (2002) defined absolute-convective transition curves for a range of Reynolds number.

Computations have revealed the consequences of harmonic forcing of azimuthal modes. For the case of a parallel swirling jet flow, Delbende & Rossi (2005) observed several effects, among them the occurrence of flow relaminarization during part of the oscillation cycle. Viola et al. (2016) employed DNS, along with theoretically-based approaches, to examine the effects of harmonic forcing of a globally stable, non-parallel Batchelor vortex for extreme cases of initially infinitesimal and finite amplitude levels of forcing. The forcing acted on all three velocity components. The azimuthal mode structure of the vortex was found to be a strong function of the forcing frequency and, furthermore, influenced by the amplitude of the forcing.

Another class of theoretical approaches involves the effects of self-induction. The analyses of Hama & Nutant (1961), Hama (1962) and Hama (1963) employed this approach for a curved vortex filament, and described the temporal evolution of a vortex subjected to an initial perturbation. Their analyses demonstrate that the self-induction effects occur as a result of induced velocity, which is most prominent in the region with the largest curvature along a curved vortex. Moreover, the induced motion acts in the opposite direction to that of the circulation of the vortex.

## 1.4 STREAMWISE VORTEX-BODY INTERACTIONS

There are several classes of vortex-body interactions defined by the orientation of the incident vortex with respect to the interacting body. They are generally classified as streamwise, parallel and normal vortex interactions. Rockwell (1998) has reviewed the literature characterizing the relationship between vortex impingement on a body and the induced loading. The following section is solely focused on the streamwise vortex-body interaction and its applications.

### *1.4.1 Wing-Vortex Interaction*

Vortex-wing interaction is prevalent in the formation flight of birds and aircraft. Lissaman & Schollenberger (1970) showed that the aerodynamic performance of a flock of birds flying in a vee formation improves as a result of a reduction in induced drag. Analysis by Hummel (1983, 1995) using a line vortex demonstrated that with proper

positioning of the wings, follower birds are able to capture the upwash of upstream birds, which increases the lift to drag ratio. This effect can provide significant energy savings as a result of the increased aerodynamic performance. A study by Weimerskirch et al. (2001) confirmed that pelicans flying in formation, shown in Figure 1.4, expended less overall energy, relative to a single pelican; this was confirmed by measuring their heart rates.

The increase in aerodynamic performance of birds flying in formation, as found in nature, can be applied to aircraft. Similar studies as those related to the formation flight of birds have been performed. Schlichting (1951) demonstrated benefits could be achieved by modelling aircraft in formation using horseshoe vortices. More recently, Bangash et al. (2006) characterized the aerodynamics of different arrangements of formation flight using wind tunnel tests. These formation arrangements are shown in Figure 1.3. Echelon and chevron formations provided an increase in the lift to drag ratio, however the echelon formation produced a rolling moment on the follower aircraft. Spanwise overlap between the wings greatly influenced the enhanced lift. Analysis of the aerodynamic performance of aircraft flying in extended formation was carried out by Ning et al. (2011). Significant reductions of induced drag can be achieved in formations of two and three aircraft with streamwise separation distances less than 30 wingspans. They found that tracking the incident vortex produced the largest variation in savings of induced drag. Inviscid analysis of extended formation flight was performed by Kless et al. (2013). Using ailerons as roll-trim, they found that optimal performance is attained with a 10% spanwise overlap between wings.

While several studies have characterized the performance of aircraft and birds flying in formation, others have looked closer at the detailed, underlying flow physics that occur in these scenarios. Recently, high-fidelity numerical computations by Garmann & Visbal (2015) showed the influence of spanwise impingement location of a steady vortex incident upon a finite wing on the modes of interaction. With outboard positioning of the incident vortex, a vortex dipole formed along the wingtip. With tip-aligned positioning, the two vortices become entrained with one another. Inboard positioning resulted in unsteady fluctuations of the incident vortex pinching off the top and bottom surfaces of the wing. In the time-mean sense, a bifurcated vortex was apparent. In all cases, the incident vortex was shown to develop a spiral instability; however, it amplified more quickly at impingement locations inboard of the wingtip. Experiments by McKenna & Rockwell (2016) agree well with the modes of interaction highlighted in the foregoing and provide further insight into their topological features. Similarly, Barnes et al. (2015) used high-fidelity numerical computations to investigate the flow structure along wings in close formation. Modes of interaction that were revealed were similar to those of Garmann & Visbal (2015), in relation to spanwise impingement location, shown in Figure 1.11. Using the same technique, Barnes et al. (2016) explored the consequences of vertical offset at a constant spanwise impingement location for this class of interaction.

McKenna et al. (2017) used stereo particle image velocimetry to investigate the upstream influence of a downstream wing on an impinging vortex, as a function of spanwise impingement location. They showed that inboard impingements can induce instability in the vortex. The foregoing investigations highlight the effect of impingement

location on the interaction mode of the flow structure along the follower wing, as well as the upstream influence on the development of the incident vortex. These effects, in turn, influence the steady and unsteady loading experienced by the follower wing.

The sensitivity of the structure of the incident vortex to the spanwise impingement location is responsible for the various modes of interaction described in the foregoing. Therefore, unsteady motion of the follower wing in the form of bending oscillations due to wing flexibility or controlled oscillations can greatly influence the wing-vortex interaction. Barnes et al. (2014a) and Barnes et al. (2014b) used high-fidelity numerical computations to investigate the effect of wing flexibility on the flow structure of ortex-wing interaction. Barnes et al. (2015) explored the effects of forced bending oscillations on these interactions; the aforementioned spiral instability is alleviated and amplified as a result of the vertical position of the follower wing. McKenna et al. (2017b) employed stereo particle image velocimetry to investigate the effect of location of impingement of the incident vortex on the flow structure and topology along a follower wing undergoing small amplitude heaving oscillations.

Unsteadiness of the incident vortex due to control surface or wing oscillations, vortex wandering, mechanical vibration and instability can greatly influence its interaction with a stationary follower wing. A wide range of dynamics occurs when unsteadiness is present in a vortex impinging on a follower wing as shown by the computations of Garmann & Visbal (2014). They considered the effects of large-scale unsteadiness on a vortex interacting with a follower wing. Imposed wandering of the vortex was prescribed in the form of large amplitude sinusoidal motion in the spanwise

direction. As the vortex approached the wing, it developed an orbital motion. That is, vertical excursions of the vortex trajectory developed despite the imposed lateral motion of the vortex. Thus, variations of the vortex impingement location occurred and had a pronounced effect on the flow structure along the follower wing. Figure 1.12 depicts these large variations of flow structure over the course of one oscillation cycle. These variations, in turn, influenced the loading experienced by the follower wing.

### *1.4.2 Vortex-Blade Interaction*

Interaction of a vortex with a blade is common in rotorcraft and turbomachinery where a vortex(ices) shed from an upstream blade(s) impinge on a downstream blade(s) or another component(s). Wittmer & Devenport (1999) used three-component hot-wire anemometry to characterize the turbulence of a vortex and development of its core structure as it passes along a helicopter blade. Particle image velocimetry was employed by Zanotti et al. (2014) to investigate the interaction between a perpendicular vortex and an oscillating blade. In this case, an impinging vortex can create a stalled region along the blade reducing its performance. Bhagwat et al. (2015) investigated the effect of an impinging vortex on the aerodynamic loading and pressure fluctuation along a hovering rotor wing. Significant asymmetry in the induced loading along the wing can occur as a result of pressure fluctuations arising due to the vortex impingement.

### *1.4.3 Vortex-Fin Interaction*

The vortex-fin interaction is a phenomenon that occurs when a vortex impinges on a downstream structure of an aircraft, such as a tail or fin. It induces buffeting of the

surface. Washburn et al. (1993) demonstrated the effect of the tail location on vortex-induced buffeting for a vortex-fin interaction. The aerodynamic loads were more sensitive to chordwise location along the tail as opposed to spanwise location. Wolfe et al. (1995) investigated the impingement of a streamwise-oriented vortex on a thin plate and the associated pressure fluctuations in relation to patterns of vorticity. The largest pressure fluctuation peaks were evident when the center of the vortex was aligned with the leading edge of the plate. Lambert & Gursul (2004) further characterized the vortex-fin interaction using particle image velocimetry. The computations of Gordnier & Visbal (1999) found that the frequency of surface pressure fluctuations at the leading edge of a flat plate corresponds to the spiral mode of breakdown of the impinging vortex. Moreover, they revealed that impinging vortices can induce bifurcation and leading edge separation along the plate, which is depicted in Figure 1.13.

## 1.5 UNRESOLVED ISSUES

The foregoing studies have provided substantial insight into the unsteady flow physics of a tip vortex along an oscillating wing, its evolution in the near wake of the wing and interaction with a downstream wing. However, a number of aspects remain, however, unresolved:

*The three-dimensional unsteady flow structure of a wingtip vortex from an oscillating wing.* The preceding investigations have provided valuable insight into the flow structure along wings subjected to controlled motions and the development of a columnar vortex

susceptible to the onset of instability and/or in response to applied perturbations. To date, quantitative experimental insight via global imaging into the structure of a perturbed trailing vortex has received little attention. In order to gain a deep understanding of the perturbed wingtip vortex, advanced quantitative measurement techniques, such as stereoscopic PIV, are required.

*The effect of dimensionless frequency on flow structure of a tip vortex.* The effect of the kinematic parameters on the flow structure along an oscillating wing or airfoil has been well documented for the case of large-amplitude perturbations, which are generally of the order of the chord of the wing. Limited insight is available for kinematic parameters associated with perturbation amplitudes on the order of, or an order of magnitude smaller than, the diameter of the wingtip vortex. In order to properly characterize the evolution of a perturbed wingtip vortex, the parameters of the perturbation should include properly formulated versions of the dimensionless Strouhal number and the displacement amplitude.

*The evolution of the trajectory of a vortex from an oscillating wing in relation to the dimensionless frequency.* Limited insight is available regarding the nature of the vortex trajectory from an oscillating wing; namely, the onset of orbital motion of the vortex and its evolution in the streamwise direction in relation to time-dependent flow features.

*The interaction of an unsteady vortex from an oscillating wing with a follower wing.* Several studies have investigated the flow structure and aerodynamic forces for the interaction of an unperturbed incident vortex with a follower wing, blade or fin.

However, the interaction of an unsteady vortex from a wing undergoing controlled oscillations with a follower wing has remained largely uninvestigated. Perturbed vortex-wing interaction is expected to induce patterns of vorticity distortion distinctly different from those of the steady vortex-wing interaction.

*Interaction of a perturbed vortex with a follower wing: sensitivity of flow structure to spanwise location of vortex impingement.* For the case of a steady incident vortex, the mechanism of vortex-wing interaction is highly sensitive to the spanwise location of vortex impingement. The degree to which the location of impingement of the incident vortex affects the mechanism of the perturbed vortex-wing interaction has not been adequately explored. These considerations will likely lead to identification of new mechanisms of interaction.

## 1.6 RESEARCH OBJECTIVES

This investigation will focus on the flow physics of a vortex from an oscillating wing, including its interaction with a downstream wing. To interpret the flow physics, three-dimensional representations of axial vorticity, axial velocity deficit and swirl ratio are employed in conjunction with sectional representations of foregoing, as well as sectional patterns of azimuthal vorticity and streamline topology. Additionally, theoretical concepts of vortex instability will be utilized for further interpretation of experimental findings. The objectives of this investigation are as follows:

*Design and construct a novel experimental system that facilitates PIV and SPIV experiments.* A system that can independently or simultaneously control the motion of a single and tandem wing configuration is required. The system will be capable of interfacing with the existing PIV and SPIV software and hardware, such that synchronized wing motion and image capture is possible.

*Reveal generic physical mechanisms of a tip vortex from an oscillating wing.* The effect of wing oscillation on the flow structure of a tip vortex will be explored, including the onset of orbital motion of the vortex and its evolution in the streamwise direction.

*Identify basic physical mechanisms of interaction of a perturbed vortex with a wing.* Patterns of vortex distortion and flow topology will be explored for a perturbed vortex impinging on a downstream wing.

**Figure 1.1:** Red smoke visualization of a tip vortex formed from the wing of an airplane (May, 2015).

**Figure 1.2:** Smoke visualization of vortex interaction of F/A-18's flying in formation. (Thomas, 2001).

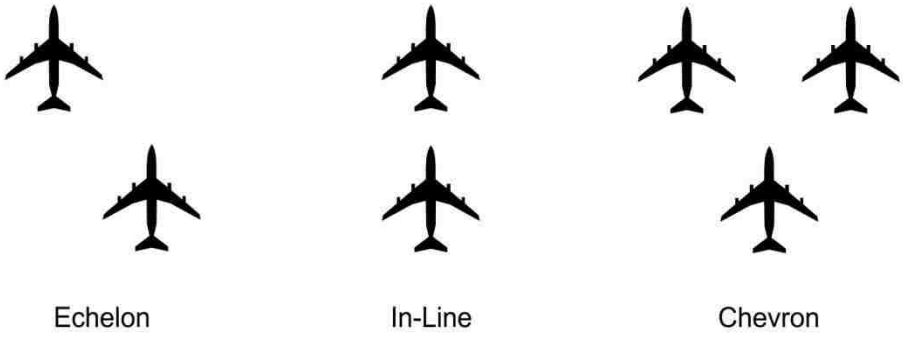


**Figure 1.3:** Traditional formation patterns of aircraft or birds.

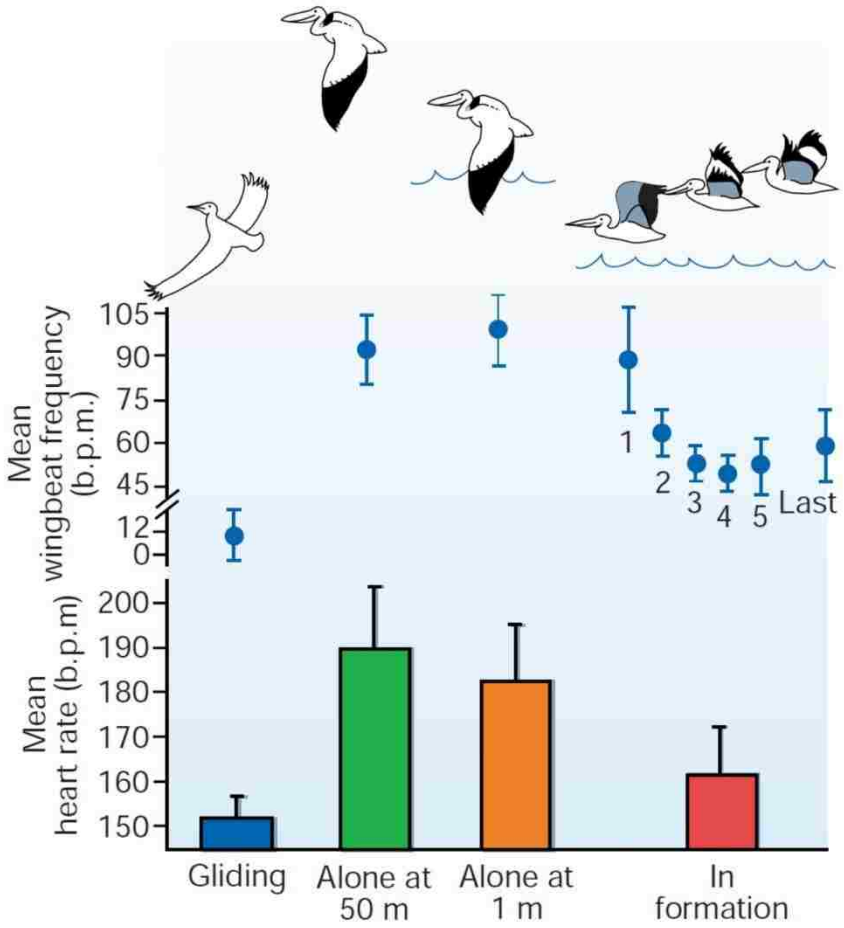


**Figure 1.4:** Measured heart rates and wingbeat frequencies for single pelicans and pelicans in formation. (Weimerskirch et al., 2001).

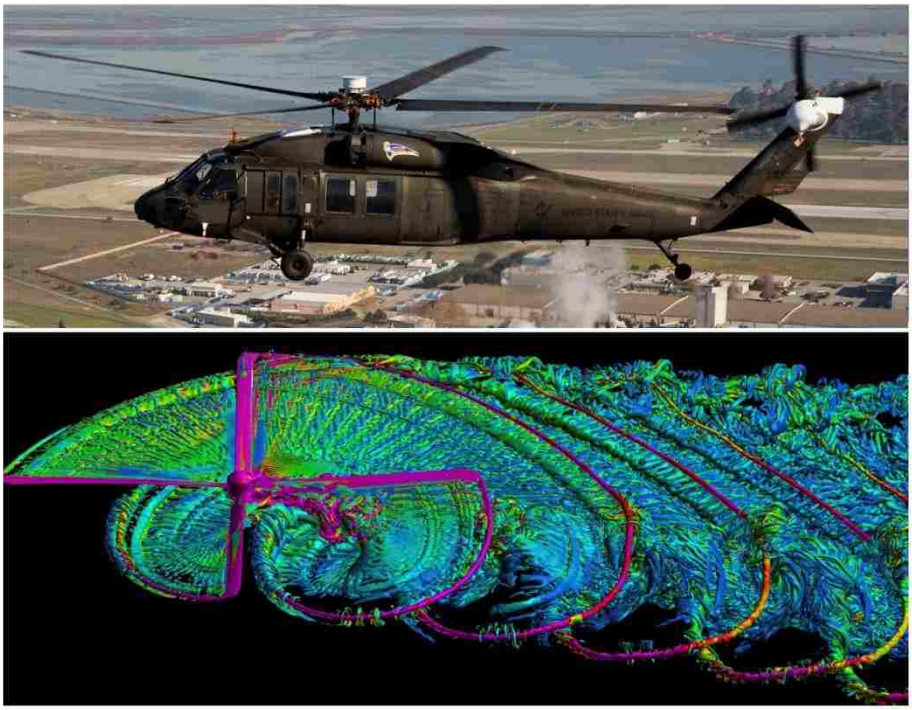

**Figure 1.5:** UH-60 Blackhawk helicopter (top) and corresponding Computational simulation of the flow field from its rotor in forward flight (bottom). (Sandstrom, 2014).


**Figure 1.6:** Smoke visualization of a tip vortex impinging on a vertical tail fin. (Conner, 1989).

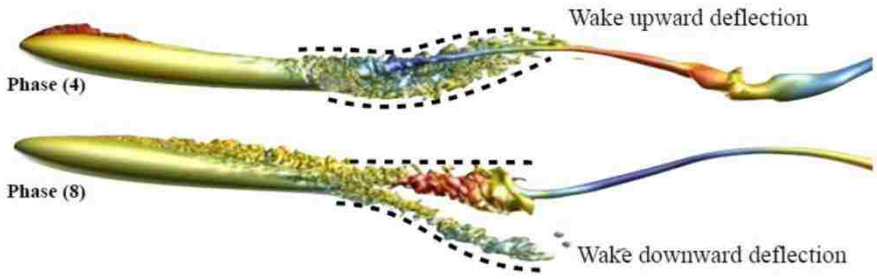


**Figure 1.7:** Flow structure of a tip vortex at two different phases from a wing undergoing small amplitude, heaving oscillations depicted in Garmann & Visbal (2016b).

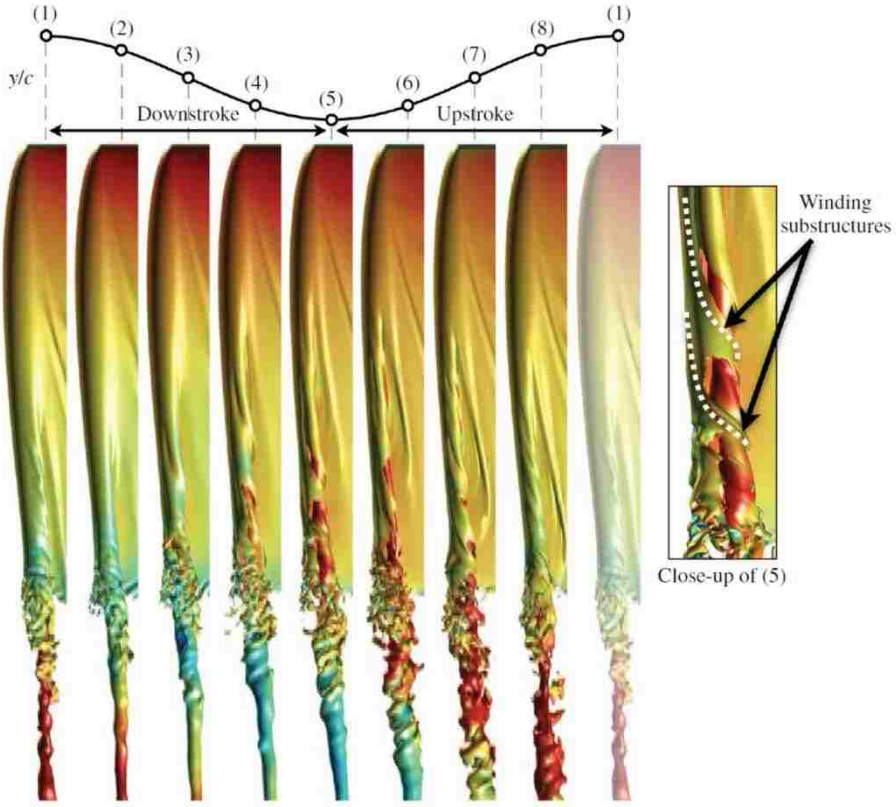


**Figure 1.8:** Flow structure of the tip vortex formation along a wing undergoing small amplitude, heaving oscillations depicted in Garmann & Visbal (2017).

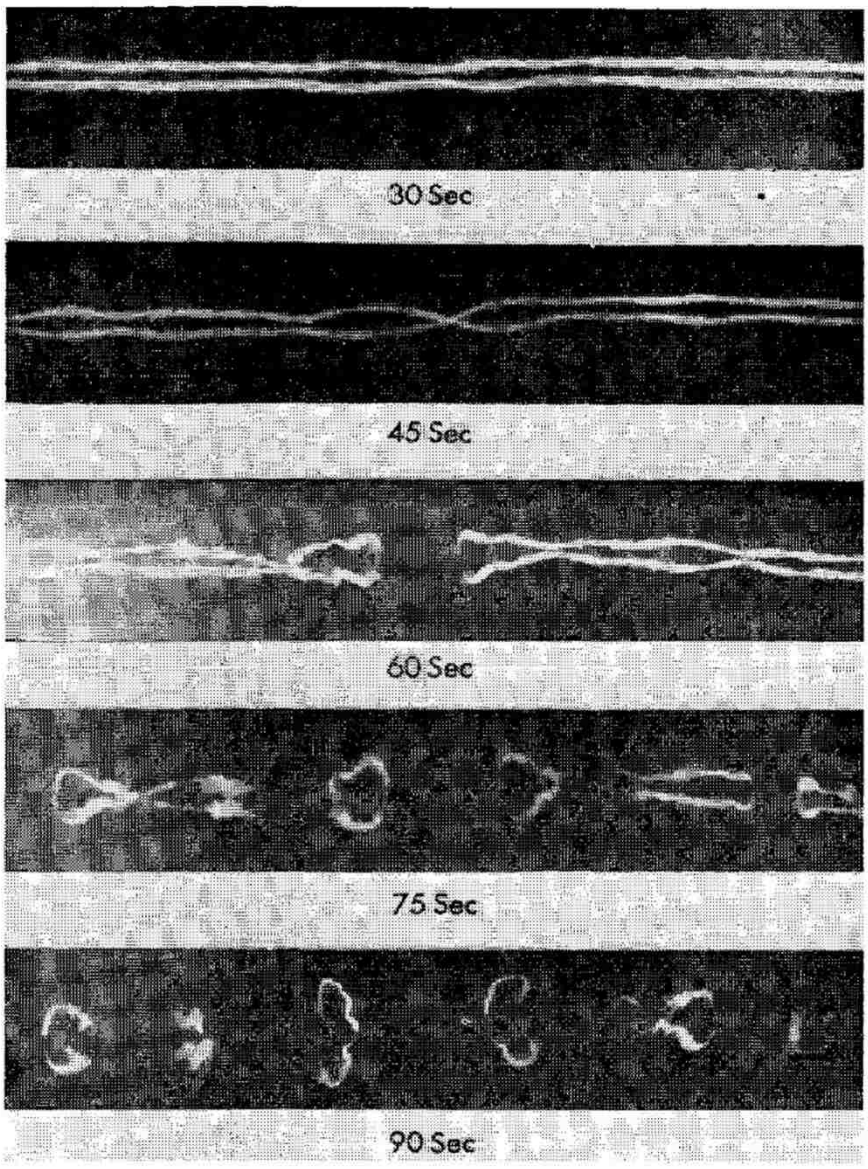


**Figure 1.9:** Time-elapsed development of long-wave instability in a vortex trail of a B-47 shown in Crow (1970).

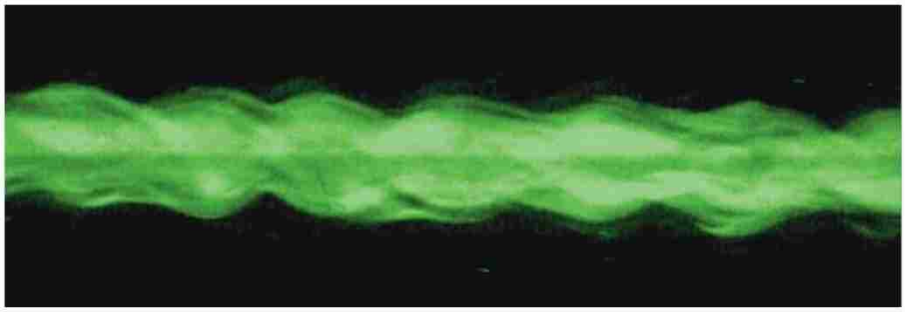

**Figure 1.10:** Flow visualization of elliptical instability from (Roy et al.,1970).

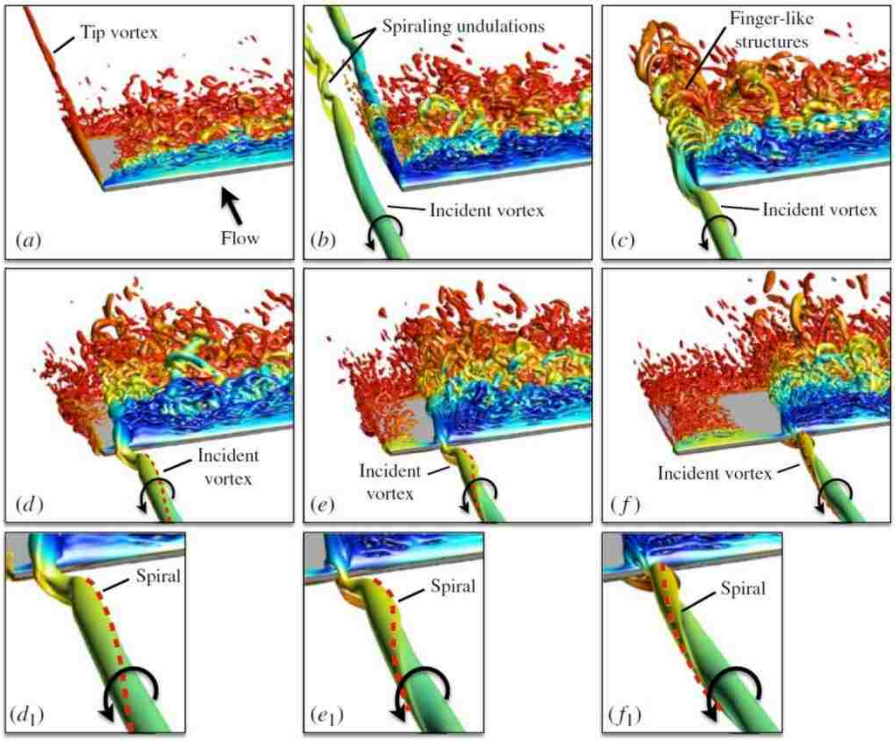


**Figure 1.11:** Instantaneous isosurfaces of the Q-criterion for increasingly inboard impingemnt locations from (a) – (f). Additional details of the impingement are provided as insets for (d-f) denoted with subscript 1. (Garmann & Visbal, 2015).

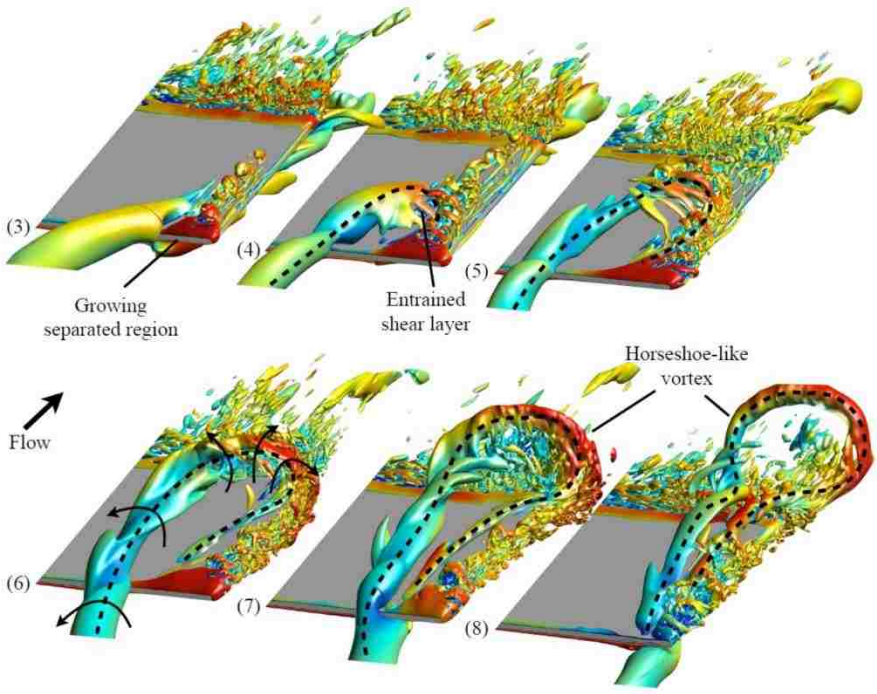


**Figure 1.12:** Isosurfaces of Q-criterion depicting the vortex structure on the underside of the wing over a portion of the vortex oscillation cycle. (Garmann & Visbal, 2014).

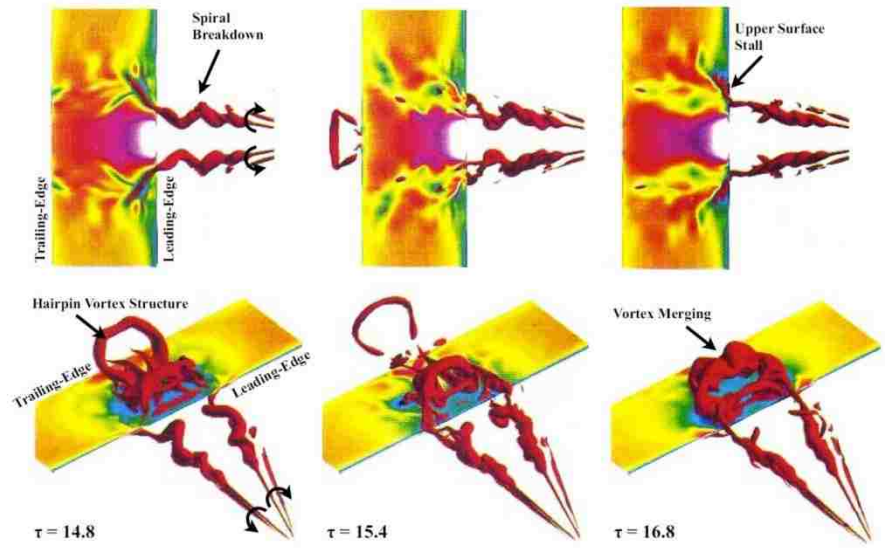


**Figure 1.13:** Unsteady flow structure of vortex impinging on a flat plate. (Gordnier & Visbal, 1999).

# CHAPTER 2

# EXPERIMENTAL SYSTEMS AND TECHNIQUES

An overview of the experimental systems and techniques employed in this research program can be found in this chapter. The experimental system descriptions include the water channel facility, the monoscopic and stereoscopic particle image velocimetry arrangements and the novel experimental rig including motion control. In addition, processing and post-processing techniques of the data, as well as, error analysis are described. Further specifics pertaining to each of the types of experiments are given in Chapters 3 through 5.

## 2.1 WATER CHANNEL

Experiments were conducted in a large-scale, recirculating free-surface water channel located in room 172 of Lehigh University's Packard Laboratory. Figure 2.1 shows a diagram of the water channel. The main test section of the facility is 594 mm in depth, 613 mm in width and 5,345 in length. The walls of the channel are made of Plexiglas which provides optical transparency for the cameras. The height of the water was maintained at a height of 559 mm for experiments. The channel is filled with water that passes through four 5 micron filters. A recirculating pump is used to create the

inflow for the test section and a sequence of honeycomb meshes and screens are arranged upstream of it in order to attain a turbulence intensity less than 0.3 percent. The flow speed is controlled by the pump and was maintained at a speed of 152 mm/s and 160 mm/s for all experiments.

## 2.2 WING CONFIGURATIONS

### *2.2.1 Single Wing Setup*

A rectangular flat plate constructed from brass was employed in all experiments. The model of the wing is a rectangular flat plate of aspect ratio $AR$ = 2, with a chord $C$ = 102 mm and span $b$ = 203 mm. The thickness of the wing is $t$ = 1.6 mm and the corner radius $r_c$ = 0.5 mm. The wing was fixed at an angle of attack $\alpha_o$ = 6° in all experiments. The wing is affixed to a traverse system which allows precision positioning and an oscillation mechanism that provides motion control. The blockage ratio of the wing with respect to the cross-sectional area of the channel, taking into account the maximum amplitude of excursion of the wing motion, is 0.01 or 1%, which is well within the acceptable range for quality wind tunnel tests, as described by West & Apelt (1982). Further details of these systems are discussed in section 2.3.

### *2.2.2 Tandem Wing Setup*

The tandem wing setup includes the leader wing described in section 2.2.1, as well as a secondary wing positioned downstream of it. This wing is a rectangular flat

plate of aspect ratio $AR$ = 4, with a chord $C_{fw}$ = 51 mm and span $b$ = 203 mm. The wing was fixed at an angle of attack $\beta_o$ = 0° in all experiments. The wing is constructed from Plexiglas to allow transmission of the laser sheet through its surface, thereby providing optical transparency. It is affixed to a secondary translation stage, which allows for different streamwise spacing between it and the leader wing. This system is discussed in detail in section 2.3.

## 2.3 MOTION CONTROL

### *2.3.1 Experimental Traverse System*

The experimental traverse system consists of two stages, one for each wing, shown in Figure 2.2. These stages are situated on a rail system which extends the length of the water channel. The stages can be linked together in order to move the entire system together through the laser sheet. The position of the two stages along the water channel is controlled by a stepper motor; it drives a traverse that is attached to the first stage.

As shown in Figure 2.3, the leader wing stage is affixed to a two axis traverse that precisely controls the wing position in the vertical and horizontal directions. Two Compumotor stepper motors controlled by National Instruments P70530 micro-stepper drives are used to position the wing. This system also includes National Instruments PCI-7344 4-card, and a UMI-7764 indexer box. The mechanism used to oscillate the wing is affixed to the first stage. The follower wing stage can only move in the streamwise

direction along the previously described rail system. The follower wing is fixed on this stage such that one of the wingtips is at the center of the water channel.

### *2.3.2 Wing Oscillation Mechanism*

The oscillation mechanism is positioned on the leader wing stage and is used to oscillate the wing in the vertical direction. A schematic of the oscillation mechanism is shown in Figure 2.4. It employs a computer-controlled motor that drives a scotch-yoke mechanism, which is attached to the vertically-oriented sting of the wing. The sting is affixed to the center of the wing and also fastened to a sliding bar coupled to a vertically-oriented traverse. A connecting rod is used to link the sliding bar to a wheel that is attached to the motor. This mechanism converts the linear motion to rotational motion. The oscillation amplitudes and frequencies of the wing varied throughout the experiments and will be discussed in their respective chapters. An encoder attached to the motor is used to determine the position of the wing. A 5V trigger signal is utilized to trigger the particle imaging acquisition system. When a specific step is reached, a signal is sent to the synchronizer, which triggers image acquisition. This technique allows for images to be acquired at specific instants along the cycle of the wing motion, thereby allowing phase averaging of acquired images.

### *2.3.3 Wing Kinematics*

The leader wing was oscillated using the mechanism described in section 2.3.2. Sinusoidal heaving motion, whereby the vertical position $A(\Phi)$ is varied, was prescribed according to the following equation:

$$A(\Phi) = A_o cos(\Phi),\ \text{where}\ \Phi = 2\pi ft$$

$A_o$ is the displacement amplitude of the oscillation, $\Phi$ is the phase angle, $f$ is the frequency and $t$ is the elapsed time.

## 2.4 QUANTITATIVE IMAGING TECHNIQUES

Particle image velocimetry was used to quantitatively analyze the flow field in the present experiments. It is a non-intrusive measurement technique that allows capture of the whole velocity field. This technique employs the use of micron-sized tracer particles that are embedded in the flow field. A laser sheet in conjunction with charged coupled device (CCD) cameras are utilized to capture the illuminated flow field in the form of particle images at distinct time intervals. These images are processed, particle displacements are measured and the velocity field is computed. This technique has been used extensively and a comprehensive review is given by Adrian & Westerweel (2011).

In all experiments, a dual-pulsed New Wave Nd:YAG laser, with a maximum output energy of 120 mJ at a wavelength of 532 nm, was employed to illuminate the flow field. It operated at frequencies $f$ = 1, 3, 8 and 15 Hz throughout the course of the experiments. The laser was located underneath the water channel and mounted to a traverse system which extended the length of the channel. A laser sheet was formed through a series of cylindrical and spherical lenses; it had a thickness of 1.5 mm in the field of view. The laser sheet was projected through the water channel floor using an angled mirror and oriented such that it was perpendicular to the flow field.

The flow was seeded with 11 μm metallic coated hollow plastic spheres which have a density of 1.9589 g/cm$^3$. TSI PowerView 2M Plus cameras were utilized in these experiments. Each of the CCD cameras used to capture the particle images contains an array of 1600 pixels × 1192 pixels. Two different camera arrangements were employed in these experiments; the first used a single camera, designated as monoscopic particle image velocimetry (PIV) and the second employed two cameras to allow stereoscopic particle image velocimetry (SPIV). Insight 4G software is utilized to perform all experiments and image pre-processing.

*2.4.1 Monoscopic PIV*

Monoscopic PIV (PIV) utilizes a single CCD camera to capture the velocity field perpendicular to the flow direction; Figure 2.5 shows a rendered model and a schematic of this system. This technique was employed for the tandem wing setup discussed in Section 2.2.2 and was used to acquire particle images along the upper and lower sides of the follower wing. Using this approach, it was possible to obtain data near the surface of the wing, which would not be attainable with the constraints of the stereoscopic camera configuration. To acquire images that were orthogonal to the direction of flow, a mirror was inserted 12 wing chords downstream of the trailing edge of the follower wing. This mirror was angled at 45° with respect to the streamwise centerline of the water channel. The CCD camera was positioned perpendicular to the water channel wall and was aligned with the mirror such that the field of view was looking upstream along the follower wing. The calibration process employed the use of a calibration target which has precisely spaced markers on its surface. This target was placed in the field of view and an image

was captured. The measured distance between markings on the plate was then used to determine the magnification of the image in Insight 4G. The lack of significant upstream influence of the mirror on the flow field is discussed in Appendix A.

### *2.4.2 Stereoscopic PIV*

Stereoscopic PIV (SPIV) utilizes two CCD cameras to capture the velocity field perpendicular to the flow direction; Figure 2.6 shows a rendered model and a schematic of this system. The two perspectives allow for the determination of all three velocity components. Details of this process are discussed in section 2.4.3. This technique was employed for the single wing setup discussed in section 2.2.1. Cameras were positioned behind the wing and looked upstream at a 40° angle. The cameras were arranged in an angular displacement configuration shown in Figure 2.7. This setup employs the Scheimpflug condition shown in Figure 2.8. According to Prasad & Jensen (1995), this condition requires that the object plane, image plane and lens plane be coplanar in order to ensure uniform focus across the image plane. In order to lessen the effects of refraction, two plexiglass prisms filled with distilled water were positioned on the channel walls and arranged such that the camera axis is perpendicular to the incident face of the prism.

An intensive calibration procedure is performed for each set of experiments. This procedure utilizes the previously described calibration target. The cameras are positioned and oriented with a view in the upstream direction of the laser sheet, which is oriented perpendicular to the flow direction. The calibration target is placed at the laser sheet

location and aligned precisely in the flow field. Each camera is adjusted such that all of the markers on the plate are in focus and satisfy the Scheimpflug condition described previously. Particle images are taken and stereo-automapping is employed to correct any misalignments during calibration. This procedure generates a mapping function which maps physical to digital locations of the calibration markers, giving an evenly spaced grid containing all three velocity components. The effective resolution of this system is 14.92 pixels/mm. A calibration file is then produced, which is used in the processing of particle images.

### *2.4.3 Image Processing*

Figure 2.9a show a sample of a raw particle image and Figure 2.9b shows the pipeline of image processing for SPIV images. Two raw images were taken for each camera, left and right, at times $t_o$ and $t_o + \Delta t$, where $t_o$ is an instant in time and $\Delta t$ is the time between image captures. The incremental $\Delta t$ is selected based on the one-quarter rule described in Adrian & Westerweel (2011), which states that the value of $\Delta t$ should be at least twenty-five percent less than the laser sheet thickness divided by the maximum out-of-plane velocity. This is to ensure that particles will not leave the interrogation window, which is used to determine particle displacements, between the two frames.

A pre-processing technique was employed; it subtracts the minimum background intensity from each image. This procedure eliminates noise in the data. A standard PIV algorithm was employed for processing. Interrogation windows of 32 pixels × 32 pixels are used and contain 15-20 particles. A 50% overlap between camera frames was used

and the particle images were processed using a frame-to-frame cross-correlation technique. This produced a two-dimensional vector field for each camera. This correlation technique to determine particle displacements was developed by Hart (1998) which only considers the most significant pixels in the interrogation window utilizing bilinear peak finding. This method reduces computation time, as well as background noise. First order differencing was then utilized to calculate the average velocities in each interrogation window given the calculated particle displacements.

Post-processing of the velocity vector fields employed a local vector validation algorithm which identified spurious vectors. Essentially, a median test was performed to compare vectors with its surrounding neighbors. Spurious vectors were then eliminated and replaced using the local mean of the $5 \times 5$ vector field surrounding it. Less than 1% of vectors failed the medial test. Lastly, smoothing was performed using a Gaussian weighting function that uses the $5 \times 5$ surrounding vectors and a smoothing kernel $\sigma = 0.8$.

The foregoing process was utilized for both PIV and SPIV image processing. However, an additional step was required for SPIV. This process uses the calibration file, containing the mapping functions previously described, to determine the two in-plane velocity components, as well as, the out-of-plane velocity component from the four processed velocity components (two from each camera). This produced an evenly spaced grid containing all three velocity components.

Instantaneous images were then averaged to eliminate random error. Both time and phase averaging techniques were utilized. Particle images were acquired sequentially according to the wing motion described in section 2.3.3. Image capture was triggered by this motion control system over many cycles of wing oscillation. This procedure allowed images to be acquired repeatedly at a given wing position, i.e. phase, during the oscillation cycle. R. Images taken at a given phase (vertical position) of the wing were grouped together and averaged; this process provided phase-averaged images. Additionally, instantaneous vortex centers were made coincident before performing phase-averaging. The same process of vortex re-centering was employed for time averaging. Further discussion of averaging techniques is given in Appendix A.

*2.4.4 Volumetric Reconstruction*

Two types of volumetric reconstructions were employed: spatial and temporal. Both techniques took consecutive planes of the velocity field, in either the spatial or temporal domain, and arranged them in the out-of-plane direction. Volumetric reconstruction of the planar velocity field was performed using in-house software which interpolated and smoothed data between planes. Iso-surfaces of axial vorticity were smoothed using a method employed by Kim & Gharib (2010). The smoothed vorticity was calculated by $\omega_{new} = (\omega_{old} + \omega_{4avg})/2$, where $\omega_{4avg}$ is the mean of the four neighboring vorticity values. This process was done one time. Smoothing was only carried out for the spatially reconstructed data. In order to assess the uncertainty in the volumetric reconstruction process, the theoretical solution of the Batchelor vortex, where viscous decay was incorporated as a function of streamwise distance, was used to compute

theoretical patterns of velocity and vorticity. Over the continuous domain of the Batchelor vortex, sectional cuts of the vortex were taken at the equivalent streamwise intervals employed in the acquisition of experimental data. Linear interpolation between these planes was then performed to reconstruct volumes of velocity and vorticity. The foregoing smoothing method was then applied over the domain for axial vorticity. Corresponding deviations from the complete theoretical solution were then computed for velocity and vorticity. This process resulted in a maximum error of 1.1% from the theoretical solution along the vortex.

## 2.5 ERROR ANALYSIS

### *2.5.1 Random Error*

Random error is commonly present in any experimental system and in general comes from an unpredictable source such as electrical noise. Random error follows a normal distribution and therefore can be reduced using averaging techniques containing a sufficient number of measurements. Reduction of this type of error is discussed in section 2.5.3. Uncertainty analysis of the random error associated with the in-plane velocity measurements was performed using the procedure described in Adrian & Westerweel (2011). The primary equation utilized in these calculations is given as $\sigma_u = \sigma_{\Delta X}/(M_o \Delta t)$, where $\sigma_{\Delta X}$ is the error in determining the centroid of the particle image, $M_o$ is the image magnification and $\Delta t$, as previously defined, is the time between image captures. The image magnification is determined from the equation $M_o = \tan(\alpha)/\tan(\theta)$, where $\alpha$ is the

angle between the lens plane and the image plane and $\theta$ is the angle between the lens plane and the object plane. These angles are determined from the geometry of the camera setup. The foregoing values are: $\Delta t = 2250$ μs, $\alpha = 5°$, $\theta = 40°$ and $M_o = 0.11$. The error in determining the centroid of the particle image is calculated from $\sigma_{\Delta X} = c_\tau d_\tau$, where $c_\tau$ is a constant used to determine the particle displacement between images, and $d_\tau$ is the diameter of the particle on the image plane. A value between 0.05 and 0.07 is used for $c_\tau$ based on an estimate utilizing the particle displacement in pixels. The diameter of a particle on the image plane comes from the equation $d_\tau = M_o(1.5\delta z\lambda + d_p^2)$ where $\delta z$ is the depth of field, $\lambda$ is the operating wavelength of the laser and $d_p$ is the physical particle diameter. The physical particle diameter $d_p$ = 11μm. The depth of field is calculated using the equation $\delta z = 4f^{\#}\lambda(1+1/M_o)^2$ where $f^{\#}$ is the f-stop of the lens used in image acquisition; the f-stop $f^{\#} = 8$. Evaluating all of the foregoing equations yields an in-plane error $\sigma_u$ = 1.5% to 2.1% of the freestream velocity.

*2.5.2 Out-of-plane Error*

The foregoing analysis in section 2.5.1 describes the random error associated with in-plane displacements. Additionally, error in the out-of-plane displacements must also be considered. Lawson & Wu (1997) developed a method which can predict the out-of-plane error from the calculated in-plane error and the camera arrangement. They showed that this error ratio $\sigma_{\Delta X}/\sigma_{\Delta Z}$ between in-plane and out-of-plane displacement error is equal to $\tan^{-1}(\alpha)$, where $\alpha$ is the angular separation of the cameras. This relationship is depicted in Figure 2.10. It yields an out-of-plane random velocity error that is 1.8 to 2.5% of the freestream velocity.

### *2.5.3 Bias Error*

In PIV, bias error is inherent due to the physical limitations in resolution of a system; due to the size of the particle image relative to the size of the digital pixel. No length scale smaller than the pixel size can be resolved and pixel locking can occur, where measured displacements are biased toward integer pixel values. Adrian & Westerweel (2011) show that the bias error is a function of the parameter $d_\tau/d_r$, where $d_\tau$ and $d_r$ are the diameters of the particle on the image plane and the pixel pitch, respectively. Figure 2.11 depicts this relationship. In the present experiments the parameter $d_\tau/d_r$ is equal to 1.6, which gives a maximum bias error of 1% of the particle pitch for a parabolic fit.

### *2.5.4 Convergence of Flow Structure*

Phase averaging was employed as a method to reduce random error in instantaneous images. This technique will not, however, reduce bias error. To determine the convergence of the primary flow structure, different sample sizes were used in determining phase averages. Figure 2.12 shows examples of phase averaged images of (a) axial vorticity $\omega_x C/U_\infty$ and (b) axial velocity deficit $1 - u/U_\infty$. Two different phase angles of the wing cycle are shown for a streamwise distance $x'/C = 5$. This streamwise location is the furthest downstream location explored in these investigations. In Figure 2.12, phase averages of sample sizes of 2, 6, 10, 14, 18 and 24 images are shown. Initially, there is some disagreement in flow structure between the images containing averages of 2 and 6

images. However, with an increasing number of images, these differences become negligible. Additionally, differences in peak values lie within experimental uncertainty.

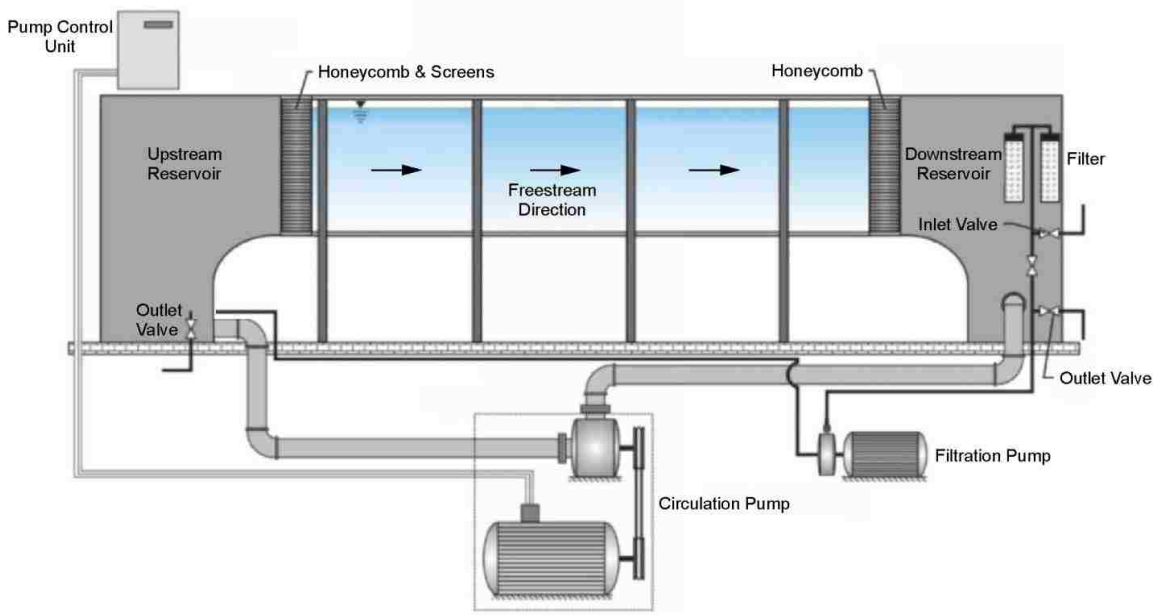


**Figure 2.1:** Water channel system in Packard Lab room 172 at Lehigh University.

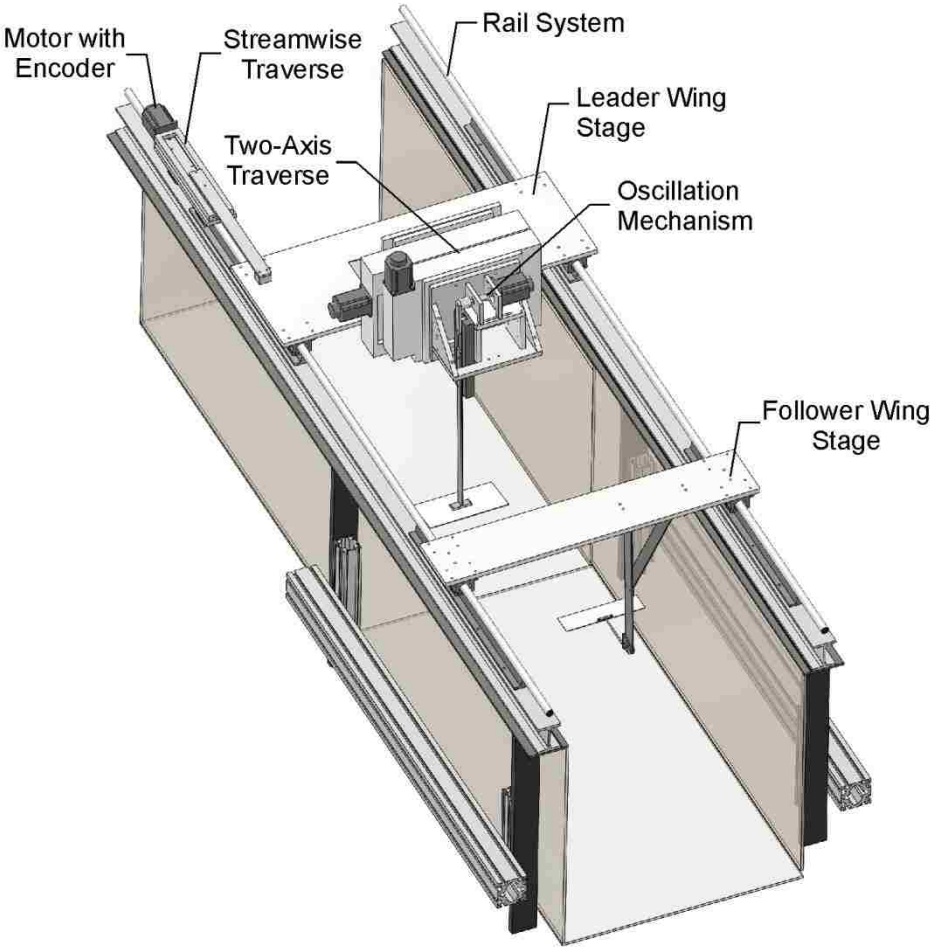


**Figure 2.2:** Overview of experimental motion control system.

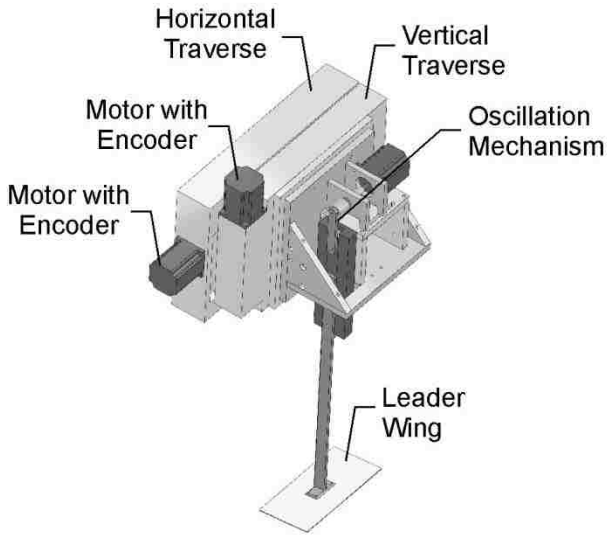


**Figure 2.3:** Detailed view of leader wing stage traverse system.

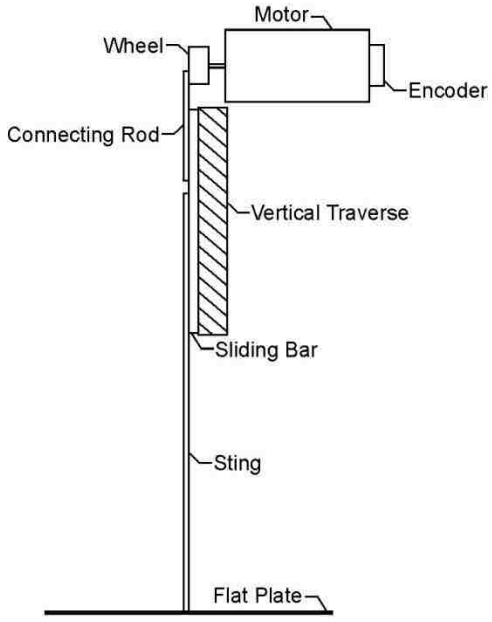


**Figure 2.4:** Schematic of wing oscillation mechanism.

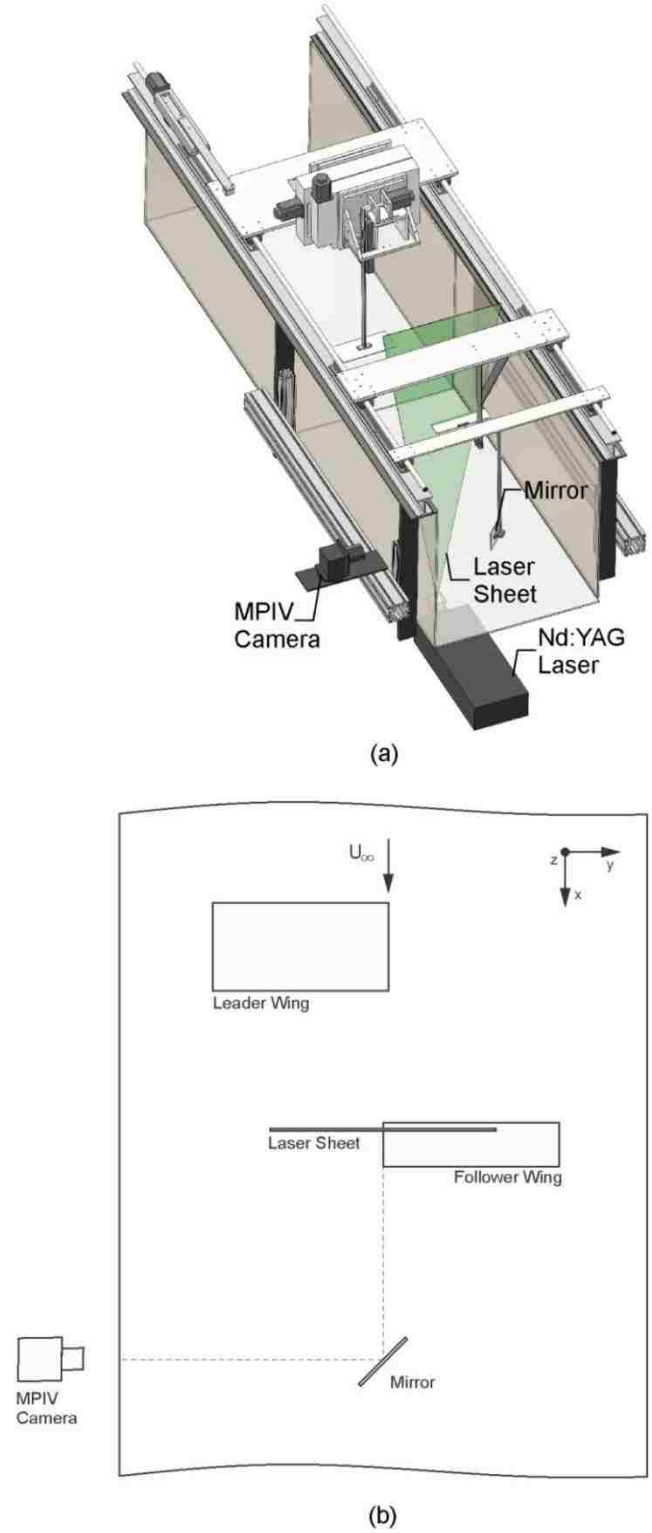


**Figure 2.5:** Overview of experimental apparatus for SPIV. (a) Three-dimensional model and (b) schematic of PIV system.

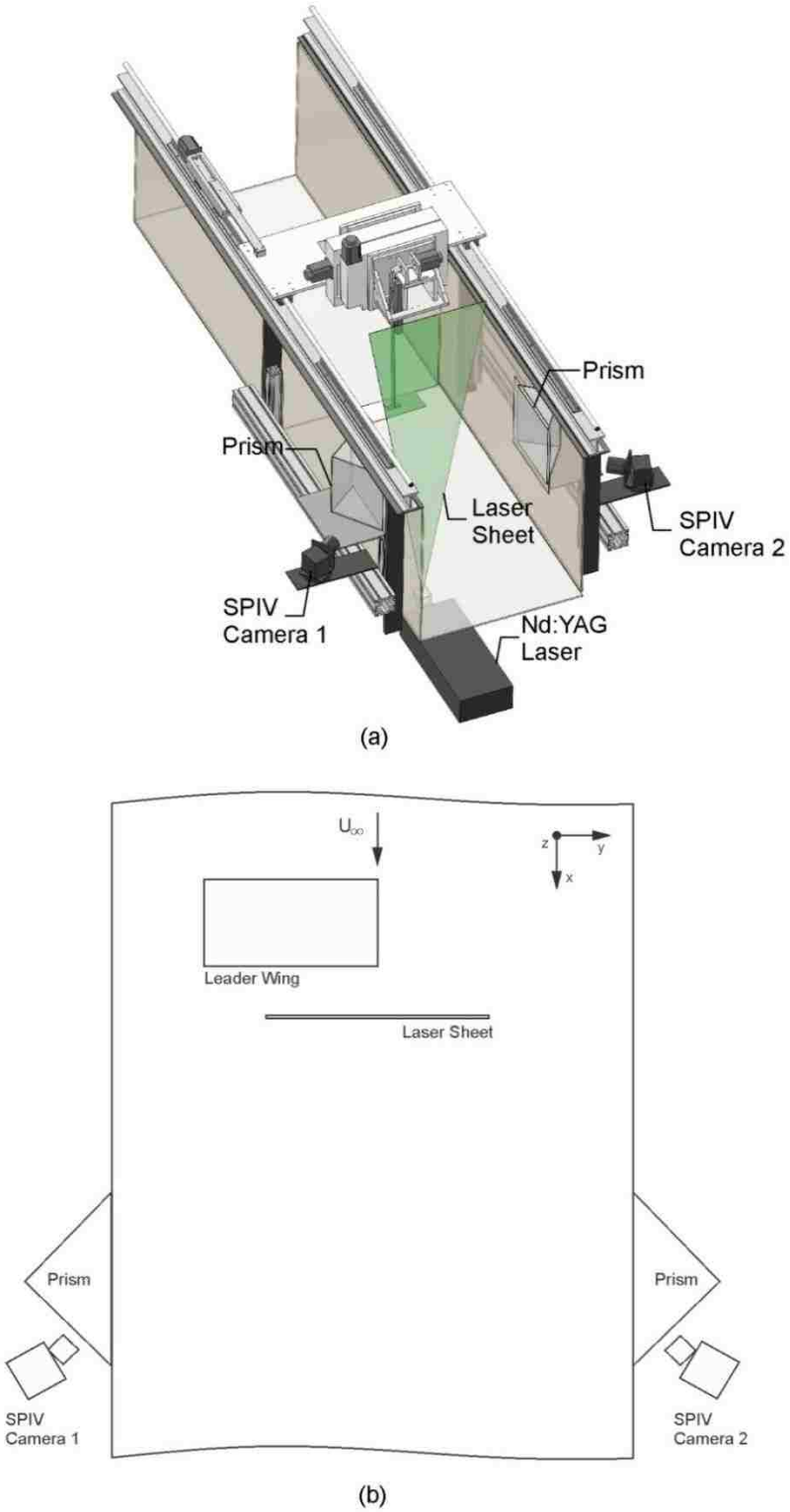


**Figure 2.6:** Overview of experimental apparatus for PIV. (a) Three-dimensional model and (b) schematic of SPIV system.

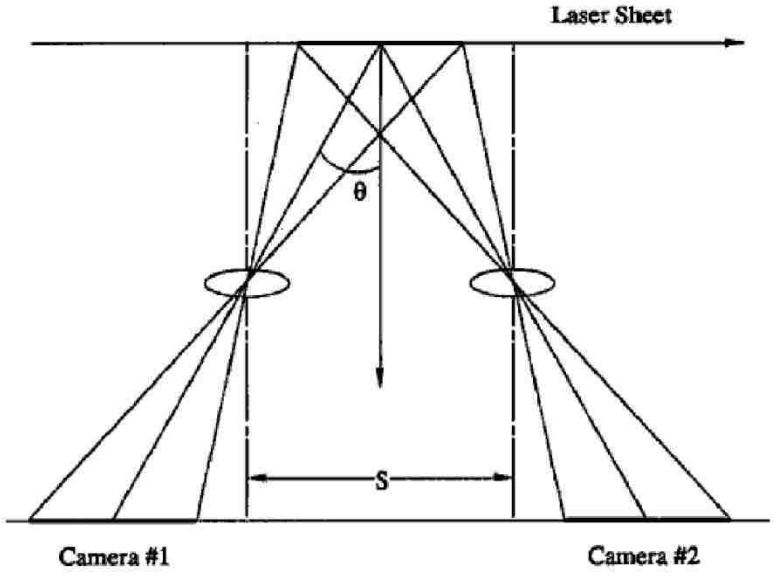


(a) Translation system

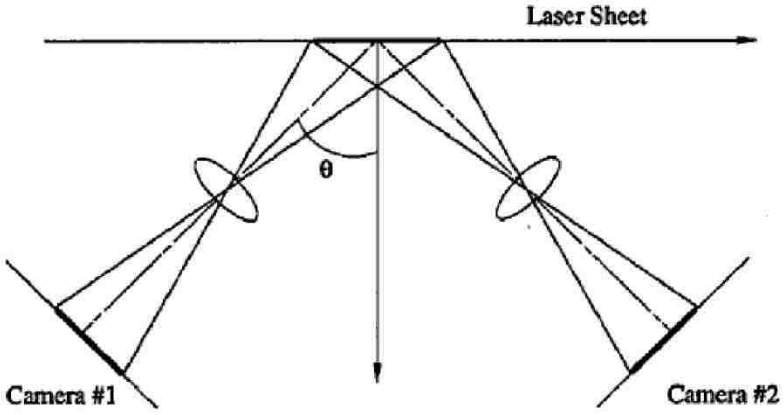


(b) Angular displacement system

**Figure 2.7:** Two configurations for stereoscopic PIV systems: (a) translation method, (b) angular displacement method. (Prasad & Jensen, 1995).

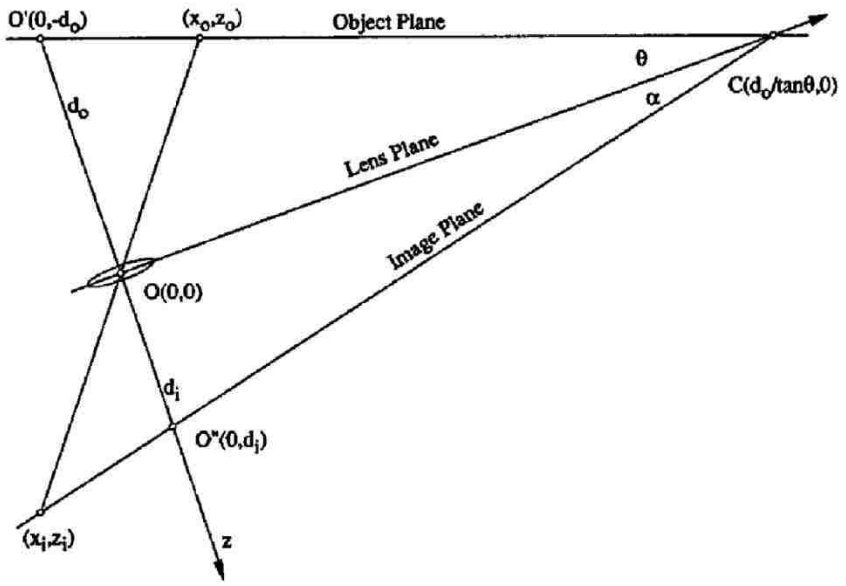


**Figure 2.8:** Schematic of the Scheimpflug condition. (Prasad & Jensen, 1995).

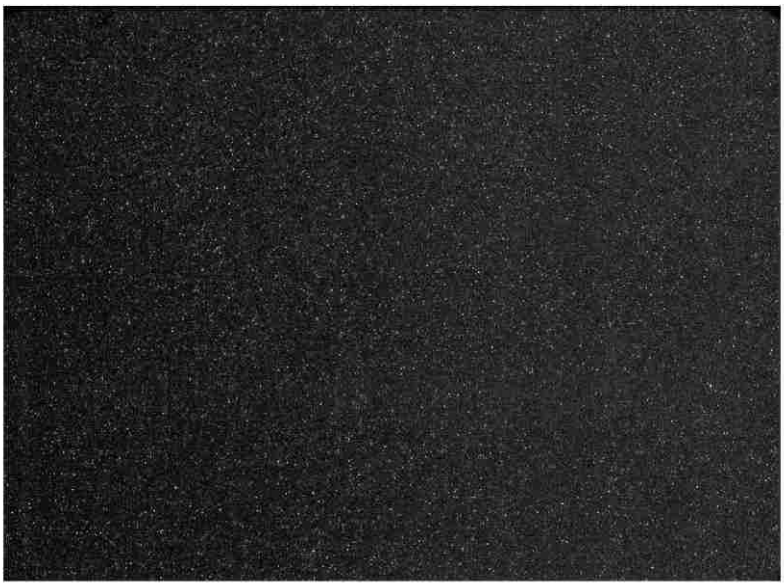

**Figure 2.9:** Overview of particle image acquisition. (a) Sample particle image.

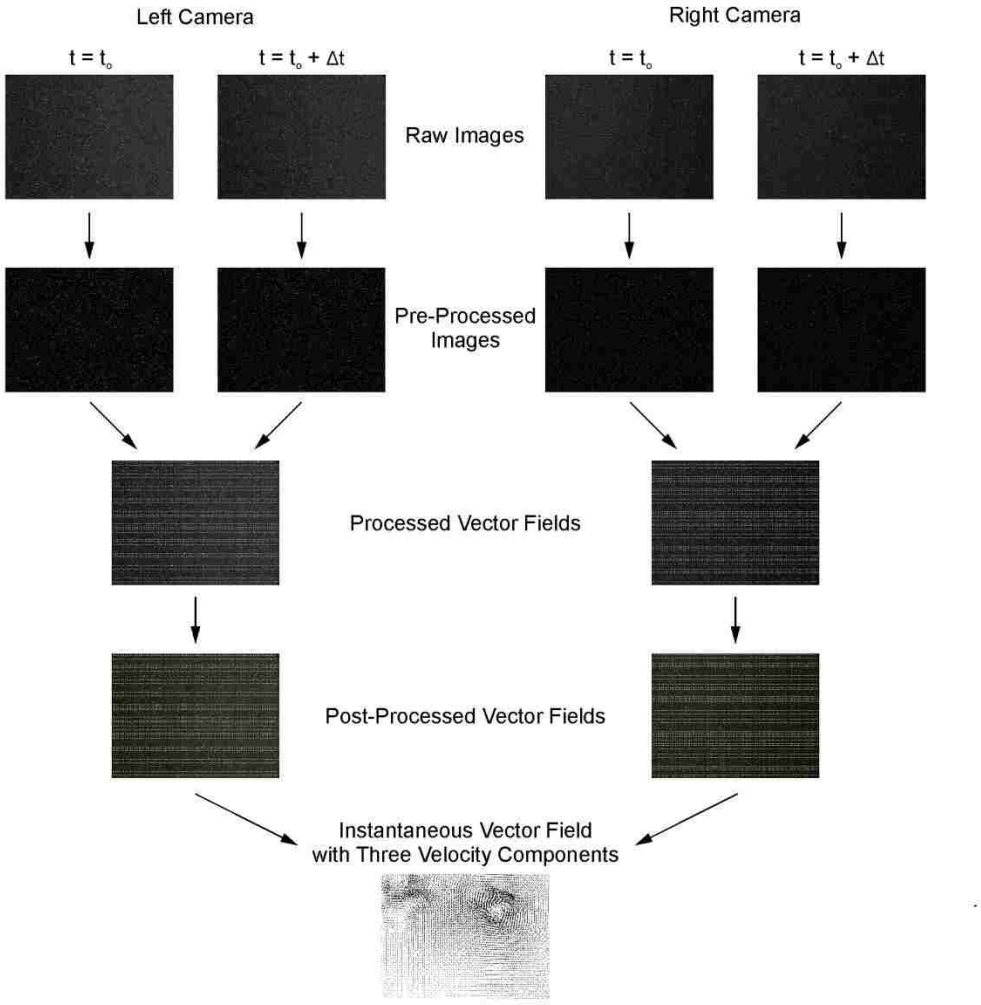


**Figure 2.9:** Overview of particle image acquisition. (b) Image processing pipeline.

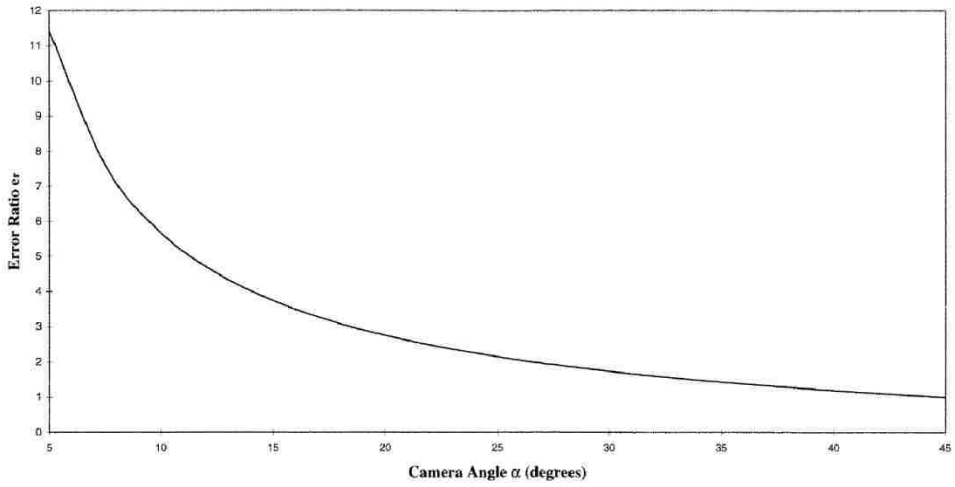


**Figure 2.10:** Error ratio between in-plane and out-of-plane displacement error. (Lawson & Wu, 1997).

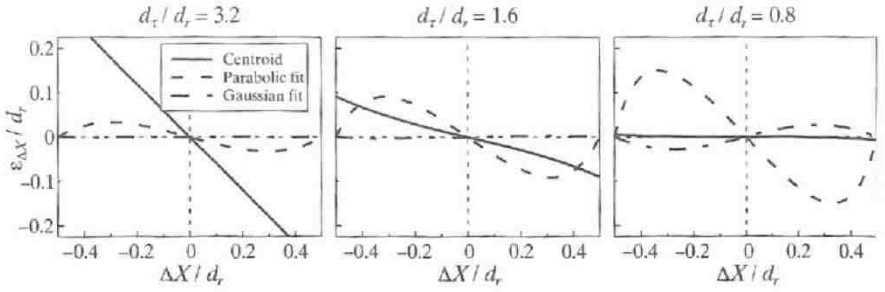


**Figure 2.11:** Bias error as a function of particle diameter and pixel pitch. (Adrian & Westerweel, 2011).

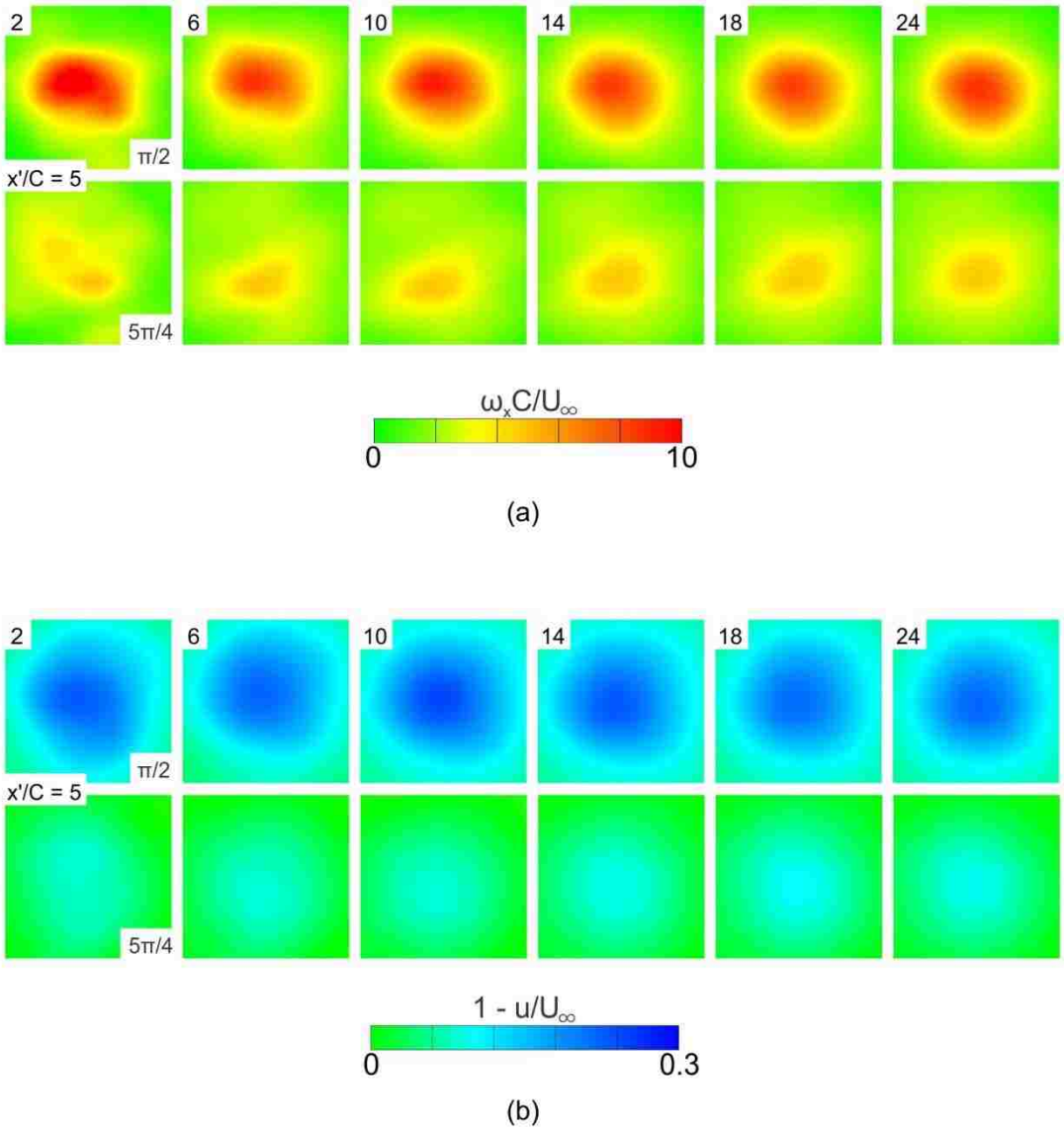


**Figure 2.12**: Phase averaged images of (a) axial vorticity $\omega_x C/U_\infty$ and (b) axial velocity deficit $1- u/ U_\infty$. Two different phase angles $\Phi$ of the wing cycle are shown for a streamwise distance $x'/C = 5$.

# CHAPTER 3

# STRUCTURE OF A TRAILING VORTEX FROM A PERTURBED WING

## 3.1 INTRODUCTION

### *3.1.1 Objectives*

Previous investigations have provided valuable insight into the flow structure along wings subjected to controlled motions and the development of a columnar vortex susceptible to the onset of instability and/or in response to applied perturbations. To date, quantitative experimental insight via global imaging into the structure of a perturbed trailing vortex has received little attention. The focus of this chapter is on the previously unexplored aspects of the physics of a trailing vortex subjected to a periodic, small amplitude perturbation having a wavelength much larger than the characteristic radius of the vortex: (i) the potential for large amplitude undulations of transverse displacement and circulation of the trailing vortex relative to small amplitude perturbation of the wing; (ii) associated variations of patterns of axial vorticity and axial velocity deficit, as well as the phase shift between them, along the vortex; (iii) the interrelationship between the onset of patterns of pronounced azimuthal vorticity in relation to patterns of axial vorticity and axial velocity deficit; (iv) the link between the foregoing aspects and the

time-dependent variation of swirl ratio along the vortex; and (v) interpretation of the vortex response in terms of concepts of stability theory, in particular the role of the theoretical threshold condition of Leibovich & Stewartson (1983) in predicting the occurrence of elevated levels of azimuthal vorticity and the degree of its persistence in downstream regions of the trailing vortex, in relation to streamwise variations of axial velocity deficit and swirl ratio. These concepts are addressed via volumetric and cross-sectional representations of the vortex structure acquired from stereo particle-image velocimetry (SPIV).

### *3.1.2 Overview*

The evolution of the vortex shows large fluctuations of axial velocity deficit and circulation during the oscillation cycle. Correspondingly, large variations of swirl ratio occur and onset of pronounced azimuthal vorticity arises. At a given cross-section of the vortex, the pattern of azimuthal vorticity moves around its axis in an ordered fashion as both it and the pattern of velocity defect increase in magnitude and scale. When the swirl ratio attains its minimum value during the oscillation cycle, and this value lies below the theoretically-established critical threshold for amplification of azimuthal modes, the magnitude and scale of the pattern of azimuthal vorticity is maximized. Subsequent increase of the swirl ratio yields attenuation of the azimuthal vorticity. Onset of pronounced azimuthal vorticity when the swirl ratio decreases, involves rapid amplification, then disruption, of axial vorticity fluctuation.

## 3.2 EXPERIMENTAL SYSTEM AND TECHNIQUES

Experiments were conducted in a large-scale, recirculating water channel at Lehigh University. The main test section of the facility is 594 mm in depth and 613 mm in width. A sequence of honeycomb meshes and screens are arranged upstream of the test section in order to attain a turbulence intensity less than 0.3 percent. The freestream velocity was maintained at $U_\infty$ = 160 mm $s^{-1}$ which yields a chord based Reynolds number $Re_C = U_\infty C/\nu$ = 16000, where $C$ is the chord of the wing and $\nu$ is the kinematic viscosity of water. The Reynolds number based on the scale of the vortex circulation is $Re_\Gamma = \Gamma/\nu$ = 2300, where $\Gamma$ is the circulation of the vortex.

Stereoscopic particle image velocimetry was employed to determine the flow structure of a trailing vortex from a continuously heaving wing. Figure 3.1a depicts a schematic of the system. The blockage ratio of the wing with respect to the cross-sectional area of the channel, taking into account the maximum amplitude of excursion of the wing motion, is 0.01 or 1%, which is well within the acceptable range for quality wind tunnel tests, as described by West & Apelt (1982). A laser sheet oriented in the spanwise direction, in conjunction with two charged coupled device (CCD) cameras, are used to capture the three-dimensional velocity field at successive crossflow oriented planes. The cameras are arranged in an angular displacement configuration as shown in Figure 3.1a. This arrangement employs the Schiempflug condition, which requires that the image plane, object plane and lens plane be coplanar as described by Prasad (2000). This condition ensures uniform focus across the image plane. Additionally, two prisms

filled with distilled water are placed on the sides of the channel walls in order to mitigate the effects of refraction.

Figure 3.1b shows a schematic of the mechanism used to perturb the wing. It involves a computer-controlled motor that drives a scotch-yoke mechanism attached to the sting of the wing. The sting is located at the mid-span and mid-chord of the wing. It is fastened to a sliding bar that is coupled to a vertically-oriented traverse. A connecting rod is used to fix the sliding bar to a wheel attached to the motor. The position of the wing is controlled through the feedback of an encoder attached to the motor.

Figure 3.1c is a rendered model of the test section that includes the SPIV system, the wing perturbation mechanism and the wing positioning system. The laser head is positioned underneath the channel and the laser sheet is oriented in the spanwise direction. The wing positioning system consists of several motors with encoders that allow for precise positioning of the wing in all three directions, in addition to the controlled perturbation described previously. In order to capture images at successive planes in the streamwise direction, the motion control system is translated along a rail system which extends the length of the channel.

Plan and side view schematics of the experimental system can be seen in Figure 3.2a. The model of the wing is a rectangular flat plate of aspect ratio $AR = 2$, with a chord $C = 102$ mm and span $b = 203$ mm. The thickness of the wing $t = 1.6$ mm and the corner radius $r_c = 0.5$ mm. The wing is fixed at an angle of attack $\alpha_o = 6°$ and is subjected to continuous heaving motion in the vertical direction as indicated in the side view

schematic. The region of interest extends 5 chords into the wake of the wing. Figure 3.2b depicts the sinusoidal displacement amplitude $A(\Phi)$ of the wing as a function of phase angle $\Phi$. The oscillation cycle consists of the downstroke of the wing which occurs between $\Phi = 0$ to $\Phi = \pi$ and the upstroke between $\Phi = \pi$ to $\Phi = 2\pi$.

The non-dimensional Strouhal number of the continuous wing motion, indicated in Figure 3.2b, is $St_C = fC/U_\infty = 0.24$, or $St_A = fA_o/U_\infty = 0.007$, where $f$ is the oscillation frequency of the wing and $A_o$ is the amplitude of the wing motion. This corresponds to a wavelength $\lambda/C = U_\infty/fC = 4.2$ or $\lambda/d_o = 42$, where $d_o$ is the diameter of the vortex from a stationary wing. That is, the wavelength associated with the wing motion is nearly two orders of magnitude larger than the vortex diameter. The vortex diameter $d_o$ is defined as twice the vortex radius $r_o$, where $r_o$ is the circumferentially averaged radial location where the maximum value of swirl velocity $(u_\theta)_{max}$ occurs. The displacement amplitude of the wing motion is $A_o/C = 0.03$ or $A_o/d_o = 0.3$ and the corresponding velocity amplitude is $w_o/U_\infty = 0.04$.

The structure of the vortex from the tip of the stationary wing is given in Figure 3.3, which provides experimental distributions of azimuthal velocity $u_\theta$ and axial velocity deficit $U_\infty - u$ in comparison with the theories of Batchelor (1964) and Moore & Saffman (1973). The axial component of velocity is normalized by the peak axial velocity deficit $(U_\infty - u_{min})$ in the vortex core and the half-width $r_{1/2}$, that is, the radius at which the axial velocity deficit is half of its peak value. The azimuthal component of velocity is normalized by the peak value $(u_\theta)_{max}$ and $r_o$, that is, the circumferentially averaged radial location where $(u_\theta)_{max}$ occurs. The normalized distributions of axial and azimuthal

velocity for the present vortex agree well with the theoretical distributions of Moore & Saffman (1973). The distributions of Batchelor (1964) show deviations from the data in the outer region of the vortex.

The water is seeded with 11 μm metallic coated hollow plastic spheres. The density of the particles is 1.9589 g/cm$^3$. A dual pulsed Nd:YAG laser system is employed to generate a laser sheet of 1.5 mm thickness which illuminates the particles. Each of the CCD cameras used to capture the particle images contains an array of 1600 pixels × 1192 pixels. Interrogation windows of 32 pixels × 32 pixels are used and contain 15-20 particle images. A 50% overlap between camera frames is utilized and the particle images are processed using a frame-to-frame cross-correlation technique. The effective resolution of the SPIV system employed is 14.92 pixels mm$^{-1}$. Uncertainty analysis of the in-plane velocity measurements was performed using the procedure described in Adrian and Westerweel (1997). The calculations yielded an in-plane velocity random error $\sigma_{\Delta V}$ that is 2.1% of the freestream velocity. Lawson and Wu (1997b) provides a relationship between the in-plane and out-of-plane errors. This yielded an out-of-plane random velocity error $\sigma_{\Delta U}$ that is 2.5% of the freestream velocity.

During experiments, the laser sheet was oriented in the crossflow direction, as previously indicated. Images were acquired at evenly spaced intervals in the streamwise direction for a total of 20 planes. The dimensionless distance between planes in the streamwise direction was $x'/C = 0.25$. A phase-referencing technique was employed, which grouped together images taken at a given vertical position of the wing; this process provided phase-averaged images. Instantaneous vortex centers were made coincident

before performing time-averaged and phase-averaged calculations. Each plane yielded 7424 vectors, for a total of 148480 vectors for volumetric reconstruction.

Volumetric reconstruction of the planar velocity field was performed using in-house software which interpolated and smoothed data between planes. Iso-surfaces of axial vorticity were smoothed using a method employed by Kim and Gharib (2010). The smoothed vorticity was calculated by $\omega_{new} = (\omega_{old} + \omega_{4avg})/2$, where $\omega_{4avg}$ is the mean of the four neighboring vorticity values. This process was done one time. In order to assess the uncertainty in the volumetric reconstruction process, the theoretical solution of the Batchelor vortex, where viscous decay was incorporated as a function of streamwise distance, was used to compute theoretical patterns of velocity and vorticity. Over the continuous domain of the Batchelor vortex, sectional cuts of the vortex were taken at the equivalent streamwise intervals employed in the acquisition of experimental data. Linear interpolation between these planes was then performed to reconstruct volumes of velocity and vorticity. The foregoing smoothing method was then applied over the domain for axial vorticity. Corresponding deviations from the complete theoretical solution were then computed for velocity and vorticity. This process resulted in a maximum error of 1.1% from the theoretical solution along the vortex.

## 3.3 UNSTEADY VORTEX STRUCTURE

### *3.3.1 Sectional Patterns of Axial Vorticity, Axial Velocity Deficit and Azimuthal Vorticity*

Figure 3.4 shows cross-sectional patterns of normalized axial vorticity $\omega_x C/U_\infty$, axial velocity deficit $1 - u/U_\infty$ and azimuthal vorticity $\omega_\theta C/U_\infty$ as functions of phase angle $\Phi$ for streamwise distances (a) $x'/C = 0.25$, (b) $x'/C = 1$, (c) $x'/C = 3$ and (d) $x'/C = 5$. The cross-sectional patterns are oriented such that the streamwise direction is perpendicular to the page. Azimuthal vorticity is dominated by the in-plane derivatives of the velocity components; the contribution of out of plane components is negligible, as verified by detailed computations involving variable spacing between successive planes in the streamwise direction. The vertical position of the wing defined in Figure 3.2b is used as a phase reference in these images. The oscillation cycle consists of the downstroke of the wing which occurs between $\Phi = 0$ to $\Phi = \pi$ and the upstroke between $\Phi = \pi$ to $\Phi = 2\pi$.

All of the foregoing variations are a strong function of the swirl ratio $q$, which is plotted as a function of phase angle $\Phi$ at the bottom of Figure 3.4. The stability properties of a vortex are dependent upon the swirl ratio $q$. As shown by Jacquin & Pantano (2002) it is defined as $q = \Gamma/2\pi r\Delta u = 1.567V_\theta/\Delta u$, where $V_\theta$ is the maximum azimuthal velocity and $\Delta u$ is the peak axial velocity deficit within the vortex core. Leibovich & Stewartson (1983) determined the critical value of $q = \sqrt{2}$ for which excitation of azimuthal modes can occur. For larger values, when $q > \sqrt{2}$, rotation suppresses the perturbations and stabilizes the vortex, as indicated by Jacquin & Pantano (2002). As indicated by Viola et

al. (2016), the entire range of azimuthal wave numbers can be amplified when the condition $q < \sqrt{2}$ is attained, and the vortex becomes massively unstable. It is therefore anticipated that a substantial component of azimuthal vorticity may occur.

The images in Figure 3.4a, acquired at the location $x'/C = 0.25$, close to the trailing-edge of the wing, indicate that the vertical displacement of the concentrations of axial vorticity, axial velocity deficit and azimuthal vorticity approximately follow the displacement of the wing, with a phase offset of $\pi/4$. That is, the displacement of the vortex center position decreases from $\Phi = \pi/4$ to $\Phi = \pi$ and then increases from $\Phi = 5\pi/4$ back to $\Phi = 0$. At larger values of $x'/C = 1$, 3 and 5, the occurrence of maximum displacement shifts to larger values of $\Phi = \pi/2$, $5\pi/4$, and $7\pi/4$, respectively. This shift is associated with the convective speed of the induced disturbance along the axis of vortex which is on the order of the freestream velocity.

Furthermore, at $x'/C = 0.25$, the structure of the axial velocity deficit involves, for all values of phase angle, two regions: the core of trailing vortex, which has an approximately circular cross-section; and the wake of the wing associated with a nominally horizontal layer of velocity deficit. This combination results in distortion of the axial velocity deficit of the vortex, such that it is not completely circular. Additionally, it is evident that the increase and decrease of the strength of axial vorticity, axial velocity deficit and azimuthal vorticity are directly related to the position of the wing. During the downstroke, the magnitude and scale of the axial vorticity increase. However, during the upstroke, the converse occurs. This is also evident in the patterns of the axial velocity deficit and azimuthal vorticity. Significant levels of the magnitude and

scale of the axial velocity deficit are present during the downstroke, yet decreased levels are apparent during the upstroke. While these features are approximately in phase, there is a discernable phase shift between occurrences of peak values of axial vorticity and axial velocity deficit, which will be further addressed in conjunction with Figure 3.6.

The images at $x'/C = 0.25$ indicate that rings of azimuthal vorticity form around the center of the vortex for phases $\Phi = 0$ to $\Phi = \pi$ in conjunction with enhanced levels of axial vorticity and axial velocity deficit. These developments occur below the critical value of swirl ratio $q = \sqrt{2}$. The temporal evolution, that is, the evolution with increasing phase $\Phi$, of the azimuthal vorticity distribution is directly correlated to the magnitude and scale of the axial velocity deficit. A further observation is that at $\Phi = 0$, the concentration of azimuthal vorticity is not evenly distributed across the vortex. Enhanced azimuthal vorticity is evident along the top portion of the concentration indicated by darker levels of red. This region moves as an organized pattern around the vortex with increasing phase. When $\Phi = 3\pi/4$, the region of highest level azimuthal vorticity is located along the bottom portion of the concentration. Subsequently, the level of azimuthal vorticity is attenuated during portions of the downstroke, from $\Phi = \pi$ to $3\pi/2$. However, at $\Phi = 7\pi/4$, when the value of swirl ratio falls below the critical value $q = \sqrt{2}$, re-formation of the region of peak azimuthal vorticity occurs along the top portion of the vortex. In essence, large magnitudes of the axial velocity deficit are associated with enhanced azimuthal vorticity, which evolve in an organized manner around the vortex. In fact, this observation holds for all streamwise distances $x'/C$ as evident in subsequent image layouts.

At $x'/C$ = 1, corresponding to the sets of images in Figure 3.4b, the structure and trajectory of the vortex, with respect to axial vorticity, are comparable to that at $x'/C$ = 0.25. However, the nature of the axial velocity deficit has changed considerably. It is evident that its magnitude is not sufficiently large to be clearly detectable at all values of phase angle $\Phi$, as is the case at $x'/C$ = 0.25. That is, when $\Phi = 0$ and $\Phi = 7\pi/4$, the axial velocity deficit tends to zero. A pronounced axial velocity deficit is, however, present from $\Phi = \pi/4$ to $\Phi = 3\pi/2$. During these phases, the concentration of axial velocity deficit becomes detached from the wake of the wing and is elongated in the spanwise direction during the continuation of vortex rollup. Considering the entire oscillation cycle, it is evident that the phase shift between the magnitude and scale of the concentrations of axial vorticity and axial velocity deficit are approximately equivalent to that at $x'/C$ = 0.25. In fact, this relationship also holds for larger values of $x'/C$ = 3 and $x'/C$ = 5, which are addressed in the following.

Moreover, the organized nature of the azimuthal vorticity patterns is also evident. When $\Phi = 0$, low-level azimuthal vorticity occurs along the top portion of the vortex. With increasing phase, it is evident that the region of peak azimuthal vorticity moves in a counter-clockwise orientation around the center of the vortex. The significant changes of azimuthal vorticity are a consequence of the variation of swirl ratio. From $\Phi = 0$ to $\Phi = \pi/2$, the value of swirl ratio decreases below the critical value $q = \sqrt{2}$, and remains lower than $\sqrt{2}$ through $\Phi = \pi$. Correspondingly, the development of enhanced values of azimuthal vorticity is evident and the largest magnitude concentration occurs at $\Phi = \pi$.

Conversely, from $\Phi = \pi$ to $\Phi = 7\pi/4$, the strength of azimuthal vorticity decreases as the swirl ratio value increases.

Common observations can be made for the images at $x'/C = 3$ and $x'/C = 5$, which are shown respectively in Figures 3.4c and 3.4d. It is apparent that the levels of axial vorticity within the vortex are attenuated relative to the levels at $x'/C = 0.25$ and $x'/C = 1$. Furthermore, the magnitude of the axial velocity defect is not discernable across a substantial share of the oscillation cycle. At values of $\Phi$ where the axial velocity deficit is evident, it has increased considerably in scale (spatial extent) and has become more circular in shape, relative to the patterns of velocity defect shown at $x'/C = 0.25$ and 1. Moreover, the scale of the azimuthal vorticity concentration has increased as well. It is again evident that the generation of enhanced azimuthal vorticity coincides with lower values of swirl ratio and the largest magnitude concentrations of azimuthal vorticity occur where the swirl ratio is below the critical value $q = \sqrt{2}$ .

The trajectory of the vortex at larger values of $x'/C = 3$ and $x'/C = 5$ has distinct features, relative to its initial form at $x'/C = 0.25$ where it is solely in the vertical direction, as induced by the continuously heaving perturbation of the wing. At these larger values of $x'/C$, the amplitude of the vortex motion in the vertical direction increases with streamwise distance, but the vortex also develops motion in the spanwise direction. This is evident by comparing the position of the vortex center at each phase angle. At $x'/C = 5$, from $\Phi = 0$ to $\Phi = 3\pi/4$, the vortex center moves towards the right. However, from $\Phi = \pi$ to $\Phi = 7\pi/4$, the vortex center moves in the opposite direction. In essence,

the trajectory of the vortex transitions from a purely vertical motion to an orbital motion with increasing streamwise distance.

*3.3.2 Fluctuations of Axial Vorticity and Axial Velocity Deficit*

Further insight into the undulation of the vortex and the generation of enhanced azimuthal vorticity $\omega_\theta C/U_\infty$ is shown in Figure 3.5. It indicates the structure of instantaneous fluctuations of axial vorticity $\omega_x'C/U_\infty$ and axial velocity deficit $1 - u'/U_\infty$ from the time-averaged values as a function of phase angle $\Phi$ at the streamwise location $x'/C = 5$. These fluctuations are calculated respectively according to $\omega_x'(\Phi) = \omega_x(\Phi) - \omega_{x,mean}$ and $u'(\Phi) = u(\Phi) - u_{,mean}$, where $\omega_{x,avg}$ and $u_{,avg}$ are the time-averaged (mean) values. Prior to performing the foregoing calculations, the centers of the instantaneous and time-averaged vortex patterns were aligned such that they were coincident. The consequences of the variations of patterns of $\omega_x'C/U_\infty$ and $1 - u'/U_\infty$ on images of total azimuthal vorticity $\omega_\theta C/U_\infty$ are given in the third row of Figure 3.5. All of the foregoing variations are a strong function of the swirl ratio $q$, which is plotted as a function of phase angle $\Phi$ at the bottom of Figure 3.5.

In Figure 3.5, an identifiable, small concentration of positive fluctuation of axial vorticity occurs at $\Phi = 0$. This dominant (red-yellow) structure, designated as m = 1 at $\Phi = \pi/4$, is amplified in both magnitude and scale for successive values of phase angle $\Phi = \pi/4$, $\pi/2$ and $3\pi/4$, which indicates the winding of the vortex in the positive sense, that is, in the same direction as the concentration of total vorticity shown in Figure 3.4d. At these values of $\Phi$, the magnitude of the swirl ratio is at or below the critical value of $q = \sqrt{2}$.

This evolution of the instantaneous vorticity fluctuation $\omega_x'C/U_\infty$ represents amplification of the m = 1 mode. The large-scale, positive (red-yellow) pattern of $\omega_x'C/U_\infty$ becomes distorted at $\Phi = 3\pi/4$, and at $\Phi = \pi$, it is severely disrupted, that is, partitioned into two (red-yellow) concentrations of vorticity fluctuations, with low-level vorticity fluctuations of opposite sign evident between them. The disruption of the coherent pattern of $\omega_x'C/U_\infty$ coincides with generation of enhanced azimuthal vorticity indicated in the third row of images. The amplification, distortion and eventual disruption of the m = 1 mode occurs when $q < \sqrt{2}$ in accord with the theoretical criterion of Leibovich and Stewartson (1983). At $\Phi = 3\pi/4$, the largest magnitude of the fluctuation of axial velocity deficit occurs. Remnants of the disrupted m = 1 mode are evident in the separated (red-yellow) clusters of $\omega_x'C/U_\infty$ at $\Phi = 5\pi/4$, but the major observation is that a negative (blue) circular concentration of $\omega_x'C/U_\infty$ abruptly occurs and this negative concentration of $\omega_x'C/U_\infty$ persists at $\Phi = 3\pi/2$; which occurs in conjunction with an increase of the swirl ratio. This negative (blue) concentration indicates winding of the vortex in the negative sense, which is in the opposite direction of the concentration of total vorticity shown in Figure 3.4d. At $\Phi = 7\pi/4$, it has abruptly degenerated, leaving only a low-level, negative (blue) arc-like pattern of $\omega_x'C/U_\infty$ which persists until $\Phi = \pi/4$.

In summary, the foregoing observations are related to changes of the swirl ratio $q$ depicted at the bottom of Figure 3.5. From $\Phi = 0$ to $\Phi = 3\pi/4$, the value of $q$ decreases and the scale of the (red) concentration of $\omega_x'C/U_\infty$ increases. When the swirl ratio reaches its minimum value, at $\Phi = 3\pi/4$, distortion of the coherent pattern of $\omega_x'C/U_\infty$ occurs and further disruption is evident at $\Phi = \pi$. At $\Phi = 5\pi/4$, the value of $q$ has started

to increase, and the abrupt onset of a concentrated (blue) core of $\omega_x'C/U_\infty$ is evident, as described in the foregoing. This concentrated core persists as the value of $q$ continues to increase, then rapidly degenerates when a sufficiently large value of $q$ is attained at $7\pi/4$. In essence, when the swirl ratio decreases with respect to $\Phi$, rapid amplification of the vorticity fluctuations $\omega_x'C/U_\infty$ is evident. Disruption of the pattern occurs when the swirl ratio reaches the minimum value, corresponding to attainment of the maximum positive value of instantaneous velocity deficit $1 - u'/U_\infty$, and in association with large concentrations of azimuthal vorticity $\omega_\theta C/U_\infty$. Conversely, when the swirl ratio increases with respect to increase of $\Phi$, patterns of vorticity fluctuations $\omega_x'C/U_\infty$ with a well-defined core occur, and eventually its rapid degeneration are evident at attainment of the maximum negative value of instantaneous velocity deficit $1 - u'/U_\infty$.

Conceptual insight into the patterns of $\omega_x'C/U_\infty$ over the range of phase angle $\Phi$ from 0 to $\pi$ given in Figure 3.5 is provided by Viola et al. (2016). They considered computations and theoretical interpretations of the nonlinear response of a nonparallel Batchelor vortex subjected to harmonic excitation in the form of streamwise perturbations of velocity for a range of amplitude and frequency, with the recognition that convective instability of the imposed perturbation can be amplified for a range of azimuthal wave numbers when the swirl number is less than $q = 1.5$, thereby leading to massive destabilization. Computations showed that the most robust mode corresponded to m = 1 when the amplitude of excitation is 10% of the freestream velocity. In the computations of Viola et al. (2016), the m = 1 mode takes the form of a dominant single concentration of vorticity having an axisymmetric (circular) shape, as a result of

nonlinear distortion; it is similar to that shown in Figure 3.5, and is prevalent at their dimensionless frequency of excitation $\omega_f$ = 0.5. In the present experiments, the dimensionless frequency of excitation is $2\pi fr_o/\Delta u$ = 0.49, and the amplitude is 15% of the free stream velocity for the images of Figure 3.5 where the m = 1 mode is dominant.

*3.3.3 Fluctuations of Circulation and Axial Velocity Deficit*

The foregoing variations of the vortex structure indicated in Figure 3.4 are further characterized in Figure 3.6, which shows plots of vortex circulation $\Gamma/U_\infty C$ and peak values of axial velocity deficit $\Delta u/U_\infty = 1 - u_{min}/U_\infty$ as functions of phase angle $\Phi$ for axial distances $x'/C$ = 0.25 and $x'/C$ = 5. Circulation is calculated by employing a contour integral of velocity over a rectangular boundary encompassing the vortex, such that all of its axial vorticity is contained within the boundary. Overall, it is evident that the circulation and axial velocity deficit of the vortex undergo substantial, time-dependent fluctuations, even though the controlled perturbation of the wing has a very small-amplitude. These fluctuations, while not entirely sinusoidal, exhibit a phase relationship between their peak values that persists throughout the flow field, in which the peak amplitude of the axial velocity deficit leads the peak of circulation. The foregoing relationship also holds for intermediate streamwise distances.

In Figure 3.6, instantaneous deviations from time-averaged values of circulation $\bar{\Gamma}/U_\infty C$ and peak axial velocity deficit $\overline{\Delta u}/U_\infty$ were determined. At $x'/C$ = 0.25, the peak deviation of circulation is $\Gamma'/\bar{\Gamma}$ = 43% from the time-averaged circulation $\bar{\Gamma}/U_\infty C$ = 0.14 of the perturbed vortex. The peak deviation of axial velocity deficit $\Delta u'/\bar{u}$ similarly

fluctuates in magnitude by 47% from the time-averaged value $\overline{\Delta u}/U_\infty$= 0.25. At $x'/C$ = 5, the peak fluctuation of circulation $\Gamma'/\bar{\Gamma}$ deviates from the time-averaged value of $\bar{\Gamma}/U_\infty C$ = 0.13 by 38%. On the other hand, the peak deviation of axial velocity deficit $\Delta u'/\bar{u}$ is 106% from the time-averaged value $\overline{\Delta u}/U_\infty$ = 0.15. As previously indicated, the displacement amplitude $A_o/C$ and velocity amplitude $w_o/U_\infty$ of the wing are 0.03 and 0.04, respectively. Despite the relatively small perturbation amplitudes associated with the wing motion, the vortex undergoes larger fluctuations in circulation and axial velocity deficit by one to two orders of magnitude.

### *3.3.4 Azimuthal Vorticity on Volume Representations of Axial Vorticity and Axial Velocity Deficit*

Figure 3.7 shows volumetric representations of the vortex constructed from sectional (planar) cuts of the three-dimensional velocity field. Surfaces of constant axial vorticity $\omega_x C/U_\infty$, and axial velocity deficit $1 - u/U_\infty$ are depicted for the indicated phase angles $\Phi$. Along the volumes are cross-sectional cuts of azimuthal vorticity $\omega_\theta C/U_\infty$. The images are oriented in a trimetric view and have been expanded in the vertical direction by a factor of 1.5 in order to resolve details. The field of view extends from $x'/C$ = 0.25 to $x'/C$ = 5. The small amplitude, long-wavelength perturbation of the wing has produced a vortex structure that consists of discrete regions of pronounced axial velocity deficit and azimuthal vorticity that travel through the vortex with a phase speed on the order of the freestream velocity.

Figure 3.7 also shows that large fluctuations of axial vorticity occur in the region immediately downstream of the trailing edge, which is consistent with the fluctuations indicated on the cross-sectional cuts of Figure 3.4. In the volumetric representations of Figure 3.7, fluctuations are represented by the change in color of the vorticity levels, as well as their vertical and streamwise extent at successive values of phase angle $\Phi$. During the downstroke of the wing, from $\Phi = 0$ to $\Phi = \pi$, large magnitude axial vorticity develops along the vortex centerline, but is attenuated at larger values of streamwise distance. As previously indicated in Figure 3.4, the increase in magnitude of axial vorticity with phase angle approximately coincides with the generation of significant levels of axial velocity deficit along the centerline of the vortex in the region immediately downstream of the trailing edge. This process also induces significant levels of azimuthal vorticity about the periphery of the vortex. In the middle of the upstroke, at $\Phi = 3\pi/2$, remnants of the previously formed azimuthal vorticity persist in the region immediately downstream of the trailing edge while both the concentrations of azimuthal vorticity and the region of axial velocity deficit are attenuated as they convect downstream. This point is consistent with the sectional images of Figure 3.4.

Furthermore, the concentrations of pronounced axial velocity deficit occupy distinct regions in space and propagate downstream through the center of the vortex. As previously indicated in Figure 3.6, fluctuations of circulation and axial velocity deficit in these regions can be one to two orders of magnitude larger than the imposed perturbation of the wing. It is important to note that the axial velocity deficit does not reach a magnitude corresponding to $\Delta u/U_\infty = 1 - u_{min}/U_\infty = 1$, i.e., there is no vortex breakdown,

which requires a stagnation point along the vortex axis as indicated in Leibovich (1978). In effect, the wing perturbation produces, for a given phase angle, an internal structure of the vortex that consists of alternating regions of large axial velocity deficit and circulation, and regions of small to no axial velocity deficit and small circulation. The regions are accompanied by enhanced levels of azimuthal vorticity which form around the perimeter of the vortex.

### *3.3.5 Occurrence of Azimuthal Vorticity on Volume Representations of Axial Velocity Deficit: Relation to Swirl Ratio*

The relationship between azimuthal vorticity $\omega_\theta C/U_\infty$, axial velocity deficit $1 - u/U_\infty$, and swirl ratio $q$ is evident in Figure 3.8, where the swirl ratio is plotted as a function of streamwise distance $x'/C$ for selected values of $\Phi$. A dashed black line is used to indicate the critical value $q = \sqrt{2}$. Superposed on these plots are isosurfaces of axial velocity deficit with corresponding sectional cuts of azimuthal vorticity.

At each phase $\Phi$, it is evident that in regions where $q < \sqrt{2}$, there are pronounced concentrations of axial velocity deficit and enhanced azimuthal vorticity. Moreover, the presence of azimuthal vorticity coincides with a decrease in swirl ratio, which is consistent with the cross-sectional patterns indicated in Figure 3.4. As previously indicated, high level azimuthal vorticity fluctuates in an organized manner about the center of the vortex in these regions. When the swirl ratio of the vortex is larger than $\sqrt{2}$, no significant axial velocity deficit or azimuthal vorticity is present. Moreover, the value of swirl ratio can be as large as 14. In effect, this indicates that the axial velocity deficit

along the vortex centerline can approach zero at certain phase angles, resulting in a local region of the vortex with no significant azimuthal vorticity. The combination of the foregoing observations indicates that the vortex structure is comprised of discrete regions of elevated values of azimuthal vorticity, circulation and axial velocity deficit, partitioned from regions in which the foregoing features are not present. These regions containing elevated values of azimuthal vorticity, circulation and axial velocity deficit propagate downstream along the vortex.

## 3.4 TIME-AVERAGED VORTEX STRUCTURE

### *3.4.1 Sectional Patterns of Axial Vorticity and Axial Velocity Deficit*

Figures 3.9a and 3.9b show selected cross-sectional patterns of normalized axial vorticity $\omega_x C/U_\infty$ and axial velocity deficit $1 - u/U_\infty$ for: (a) the unperturbed vortex (from a stationary wing) and (b) the time-averaged structure of the perturbed trailing vortex. It is evident that the imposed perturbation induces enhanced attenuation of the time-averaged vortex structure, relative to the unperturbed vortex. At $x'/C = 1$, the patterns and levels of axial vorticity and axial velocity deficit for the unperturbed and perturbed vortices are very similar. However, it is apparent that the magnitudes of axial vorticity and axial velocity deficit attenuate more rapidly with streamwise distance for the case of the perturbed vortex.

### *3.4.2 Volumetric Representations of Axial Vorticity and Axial Velocity Deficit*

The differences in flow structure between the unperturbed and perturbed vortices is further indicated in Figures 3.10a and 3.10b which compare iso-surfaces of axial vorticity $\omega_x C/U_\infty$ and axial velocity deficit $1 - u/U_\infty$. It is evident that the larger values of axial vorticity attenuate more rapidly in the case of the perturbed vortex. However, in the region closest to the trailing edge, increased axial velocity deficit is evident in the perturbed vortex. Additionally, the maximum level of axial vorticity in the region immediately downstream of the trailing edge of the wing has decreased considerably for the perturbed vortex. Figure 3.10c shows plots of time-averaged, peak axial vorticity as a function of streamwise distance for the cases of the perturbed and unperturbed vortex. The difference in peak axial vorticity increases with streamwise distance. At $x'/C = 5$, the value of peak axial vorticity in the unperturbed vortex is 25% greater than that of the perturbed vortex.

## 3.5 CONCLUSIONS

The structure of a trailing vortex from a wing undergoing very small amplitude, low frequency heaving motion is investigated using space-time images acquired via stereo particle image velocimetry. This perturbation, which has a long wavelength relative to the diameter of the vortex, leads to large undulations of axial velocity deficit $1 - u/U_\infty$ and circulation $\Gamma/U_\infty C$ along the vortex. Despite the small amplitude of the wing

motion, instantaneous magnitudes of axial velocity deficit and circulation can reach values of the order of 50% and 100% greater than their respective time-averaged values.

At a given cross-section of the vortex, the magnitude of the time-dependent swirl ratio $q$ undergoes large variations. As the minimum value of swirl ratio is approached, onset of pronounced azimuthal vorticity occurs, and its pattern shows the largest magnitude and scale when minimum swirl is attained. The onset of the pattern of azimuthal vorticity follows an orderly process of motion about the axis of the vortex until a ring-like structure occurs. Subsequently attenuation of the magnitude and scale of this pattern is evident. This process is closely correlated not only with the swirl ratio but also with the evolution of the pattern of axial velocity deficit; its largest magnitude and scale are in phase with the pattern of azimuthal velocity. This occurrence of elevated azimuthal vorticity is followed by regions of zero azimuthal vorticity that occur in conjunction with sufficiently large values of swirl ratio.

The foregoing characterizations at a given cross-section of the vortex have been confirmed by volumetric representations of the velocity defect and axial vorticity at selected instants (phase angles) of the wing perturbation; sectional patterns of azimuthal vorticity are superposed on these volumetric representations. Spatial variations of these representations along the axis of the vortex emphasize the important consequence of streamwise variations of swirl ratio. In particular, the largest magnitude and scale of the pattern of azimuthal vorticity occurs at the minimum value of swirl ratio.

The theoretical analysis of Leibovich and Stewartson (1983) establishes that when the swirl ratio $q < \sqrt{2}$, a range of azimuthal wave numbers may be amplified, potentially leading to massive destabilization. This criterion for $q$ provides a remarkably consistent threshold for onset of pronounced azimuthal vorticity, for temporal variation of $q$ at a given cross-section of the vortex and spatial variation of $q$ along the vortex at a given instant. When the minimum value of $q$ is attained and has a value less than $\sqrt{2}$, the magnitude and scale of the pattern of azimuthal vorticity are maximized.

Consideration of the instantaneous fluctuations of axial velocity and velocity deficit indicate that the onset of maximum magnitude and scale of azimuthal vorticity corresponds to the onset of disorder of the instantaneous axial vorticity. Comparison of the present experiments in the region of decreasing swirl ratio with the computations and theoretical interpretations of Viola et al. (2016) show that the same form of the m = 1 mode occurs in their computations and the present experiments. In the region of increasing swirl ratio, the experimental pattern of instantaneous axial vorticity shows a highly concentrated and coherent core followed by its eventual attenuation.

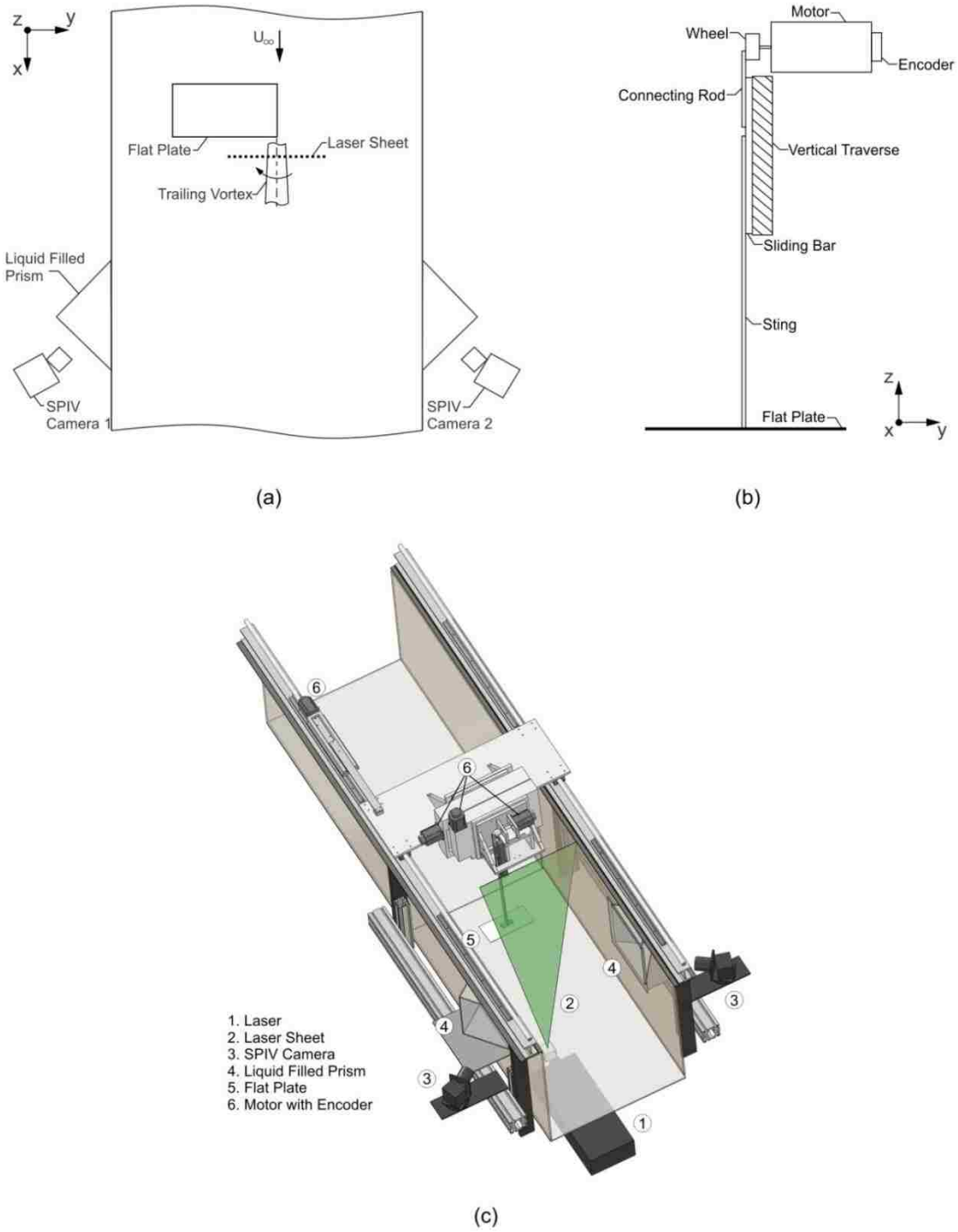


**Figure 3.1:** Overview of experimental apparatus. (a) Schematic of stereo particle image velocimetry system. (b) Schematic of wing oscillation mechanism (not to scale). (c) Model of test section and experimental system.

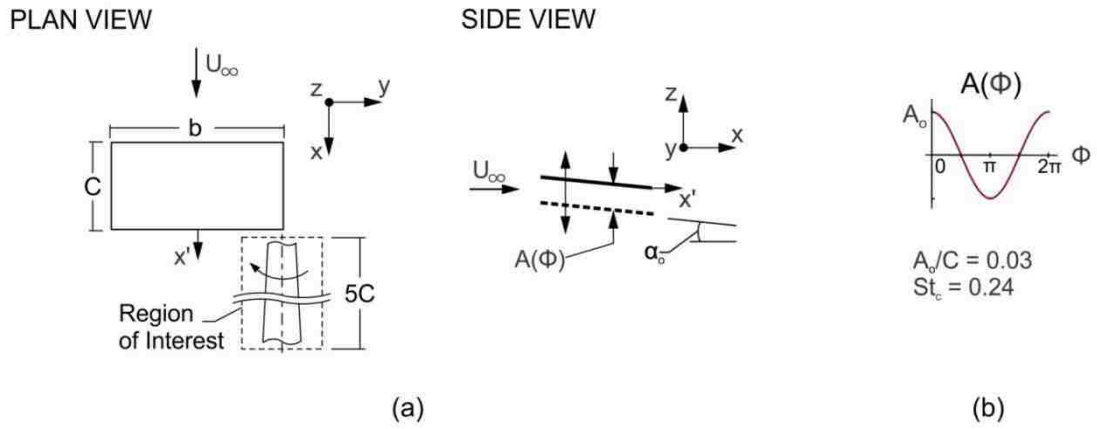


**Figure 3.2:** Overview of wing setup. (a) Plan and side view schematics of wing. (b) Motion profile of wing.

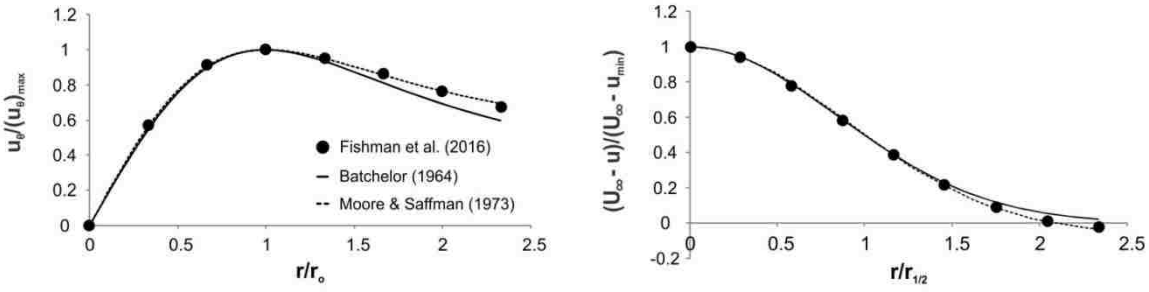


**Figure 3.3:** Comparison of normalized azimuthal velocity $u_\theta/(u_\theta)_{max}$ profiles as a function of vortex radius $r_o$ (left) and normalized axial velocity deficit $(U_\infty - u)/(U_\infty - u_{min})$ as a function of the radial half-width of the vortex $r_{1/2}$ (right).

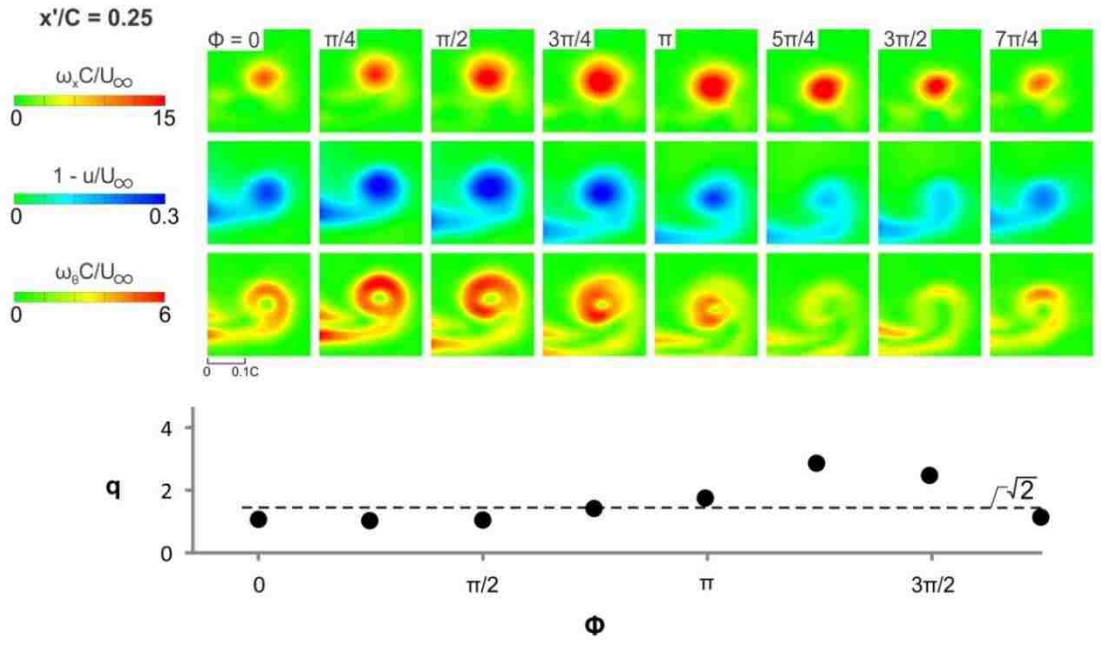


(a)

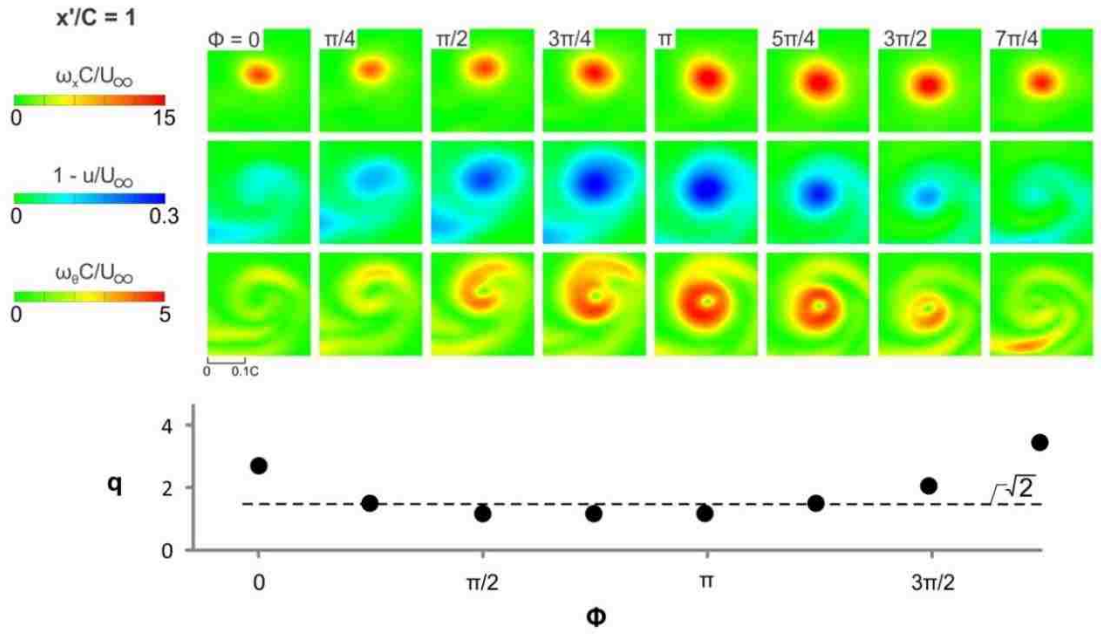


(b)

**Figure 3.4:** Comparison of sectional cuts of axial vorticity $\omega_x C/U_\infty$, axial velocity deficit $1 - u/U_\infty$ and azimuthal vorticity $\omega_\theta C/U_\infty$ as functions of phase angle $\Phi$ for streamwise distance (a) $x'/C = 0.25$ and (b) $x'/C = 1$. A plot of the swirl ratio $q$ as a function of $\Phi$ is also included.

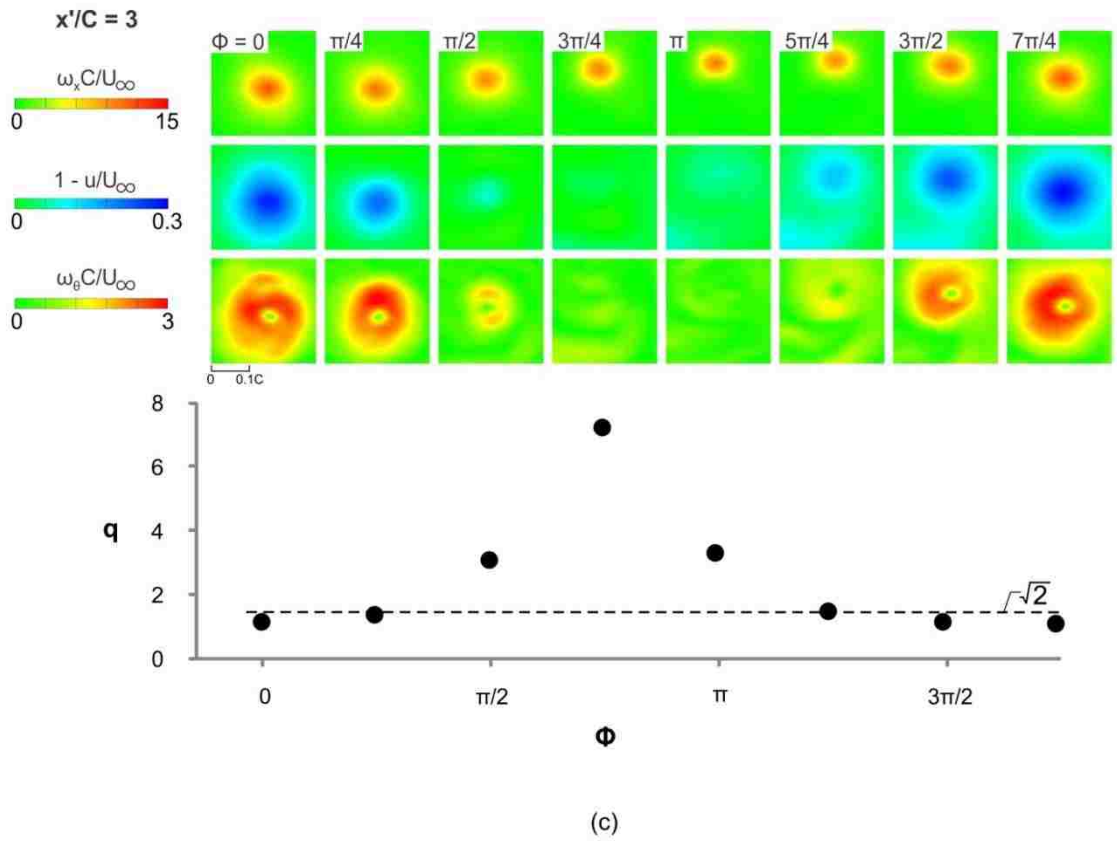


**Figure 3.4:** Comparison of sectional cuts of axial vorticity $\omega_x C/U_\infty$, axial velocity deficit $1 - u/U_\infty$ and azimuthal vorticity $\omega_\theta C/U_\infty$ as functions of phase angle $\Phi$ for streamwise distance (c) $x'/C = 3$. A plot of the swirl ratio $q$ as a function of $\Phi$ is also included.

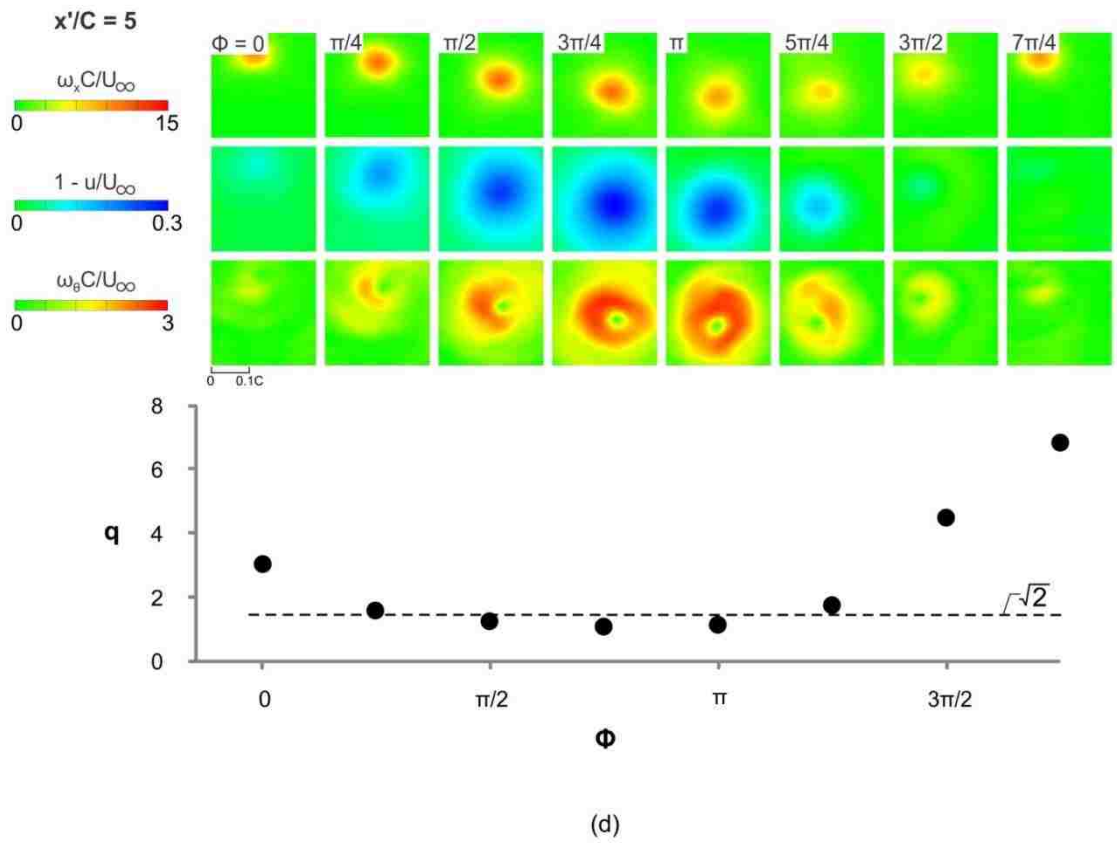


**Figure 3.4:** Comparison of sectional cuts of axial vorticity $\omega_x C/U_\infty$, axial velocity deficit $1 - u/U_\infty$ and azimuthal vorticity $\omega_\theta C/U_\infty$ as functions of phase angle $\Phi$ for streamwise distances (d) $x'/C = 5$. A plot of the swirl ratio $q$ as a function of $\Phi$ is also included.

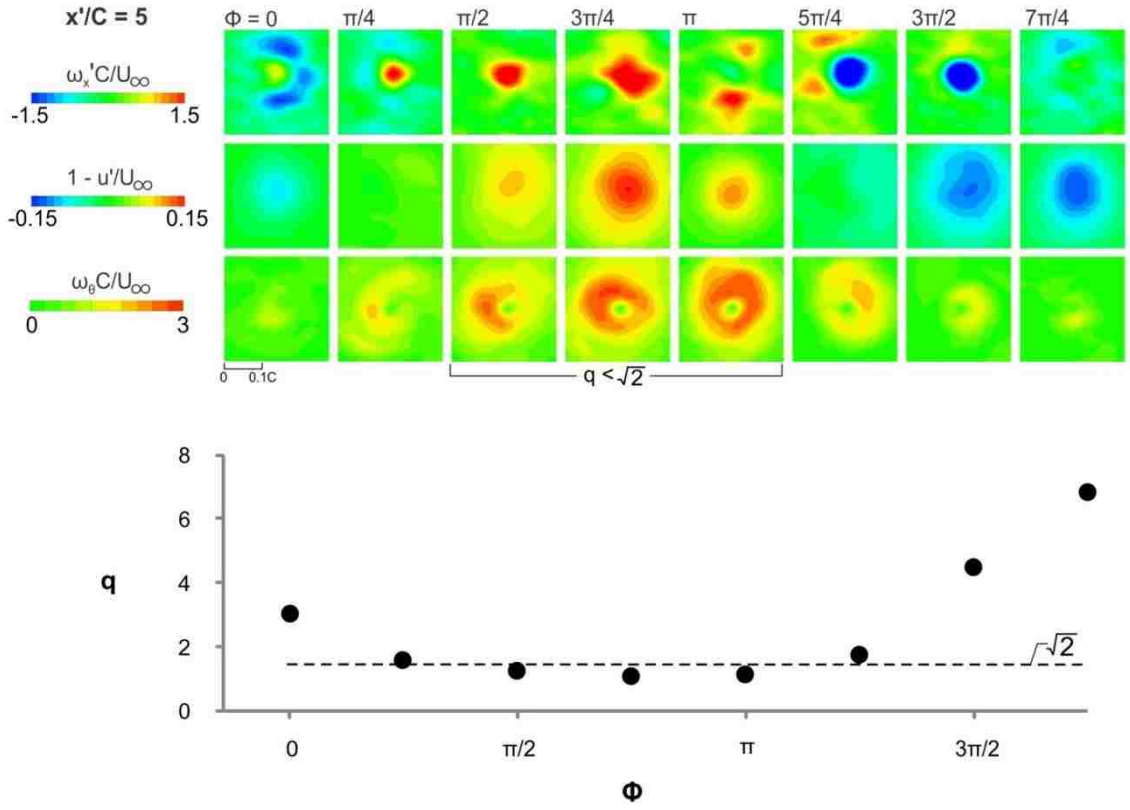


**Figure 3.5:** Sectional contours of axial vorticity fluctuations $\omega_x'C/U_\infty$, axial velocity deficit $1 - u'/U_\infty$ fluctuations and azimuthal vorticity $\omega_\theta C/U_\infty$ as functions of $\Phi$ at the streamwise distance $x'/C = 5$. A plot of the swirl ratio $q$ as a function of $\Phi$ is also included.

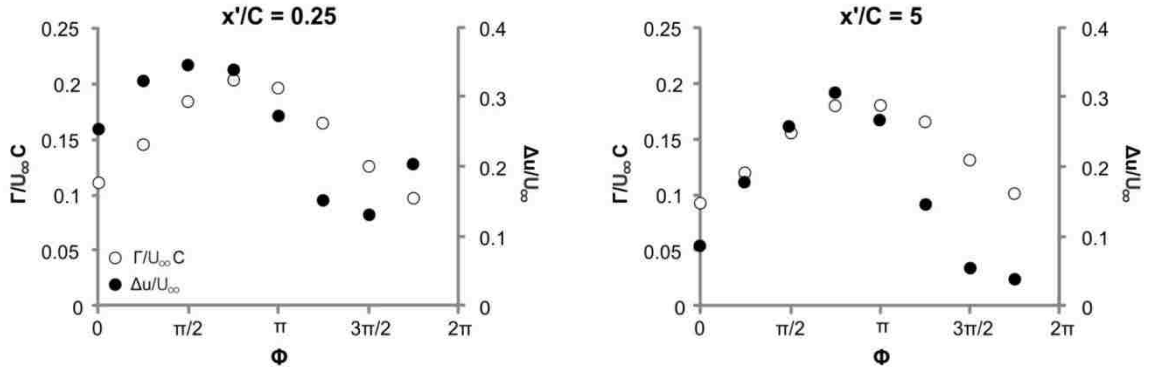


**Figure 3.6:** Comparison of plots of circulation $\Gamma/U_\infty C$ and peak axial velocity deficit $\Delta u/U_\infty$ at $x'/C = 0.25$ and $x'/C = 5$.

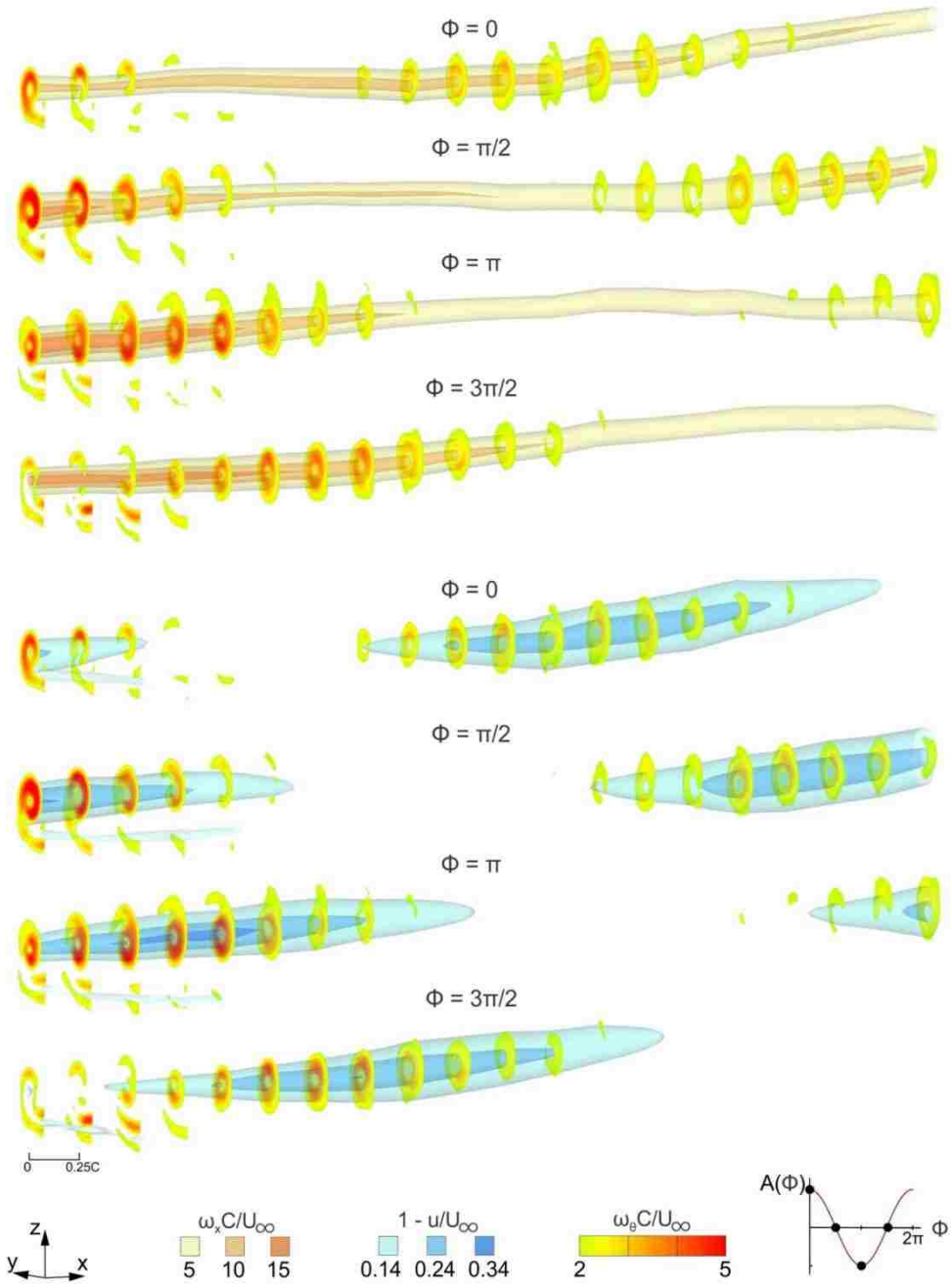


**Figure 3.7:** Comparison of iso-surfaces of axial vorticity $\omega_x C/U_\infty$ and axial velocity deficit $1 - u/U_\infty$ with sectional slices of azimuthal vorticity $\omega_\theta C/U_\infty$ as functions of phase angle $\Phi$.

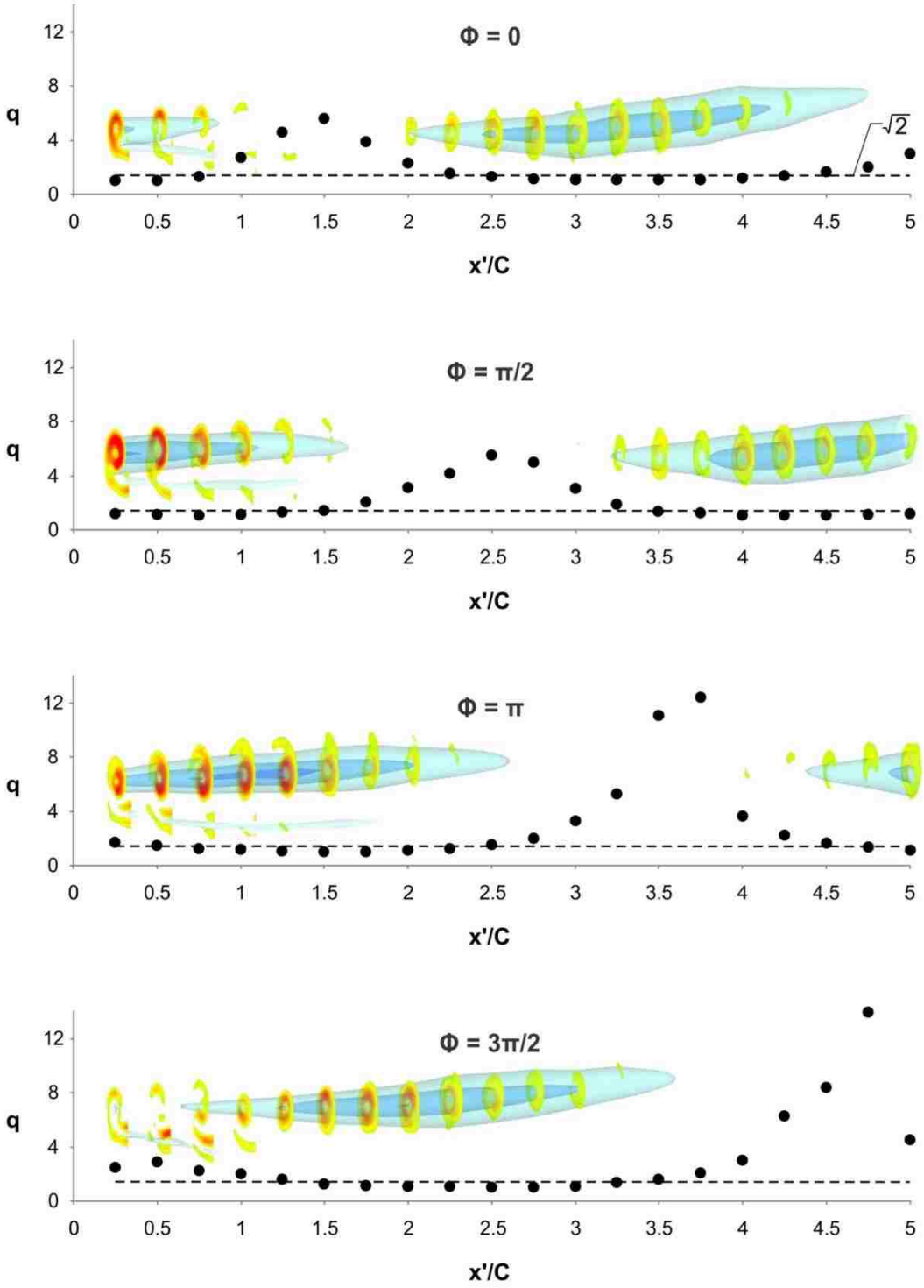


**Figure 3.8:** Plots of swirl ratio $q$ as a function of streamwise distance $x'/C$ with overlaying iso-surfaces of axial velocity deficit $1 - u/U_\infty$ and sectional cuts azimuthal vorticity $\omega_\theta C/U_\infty$ for selected phase angles $\Phi$.

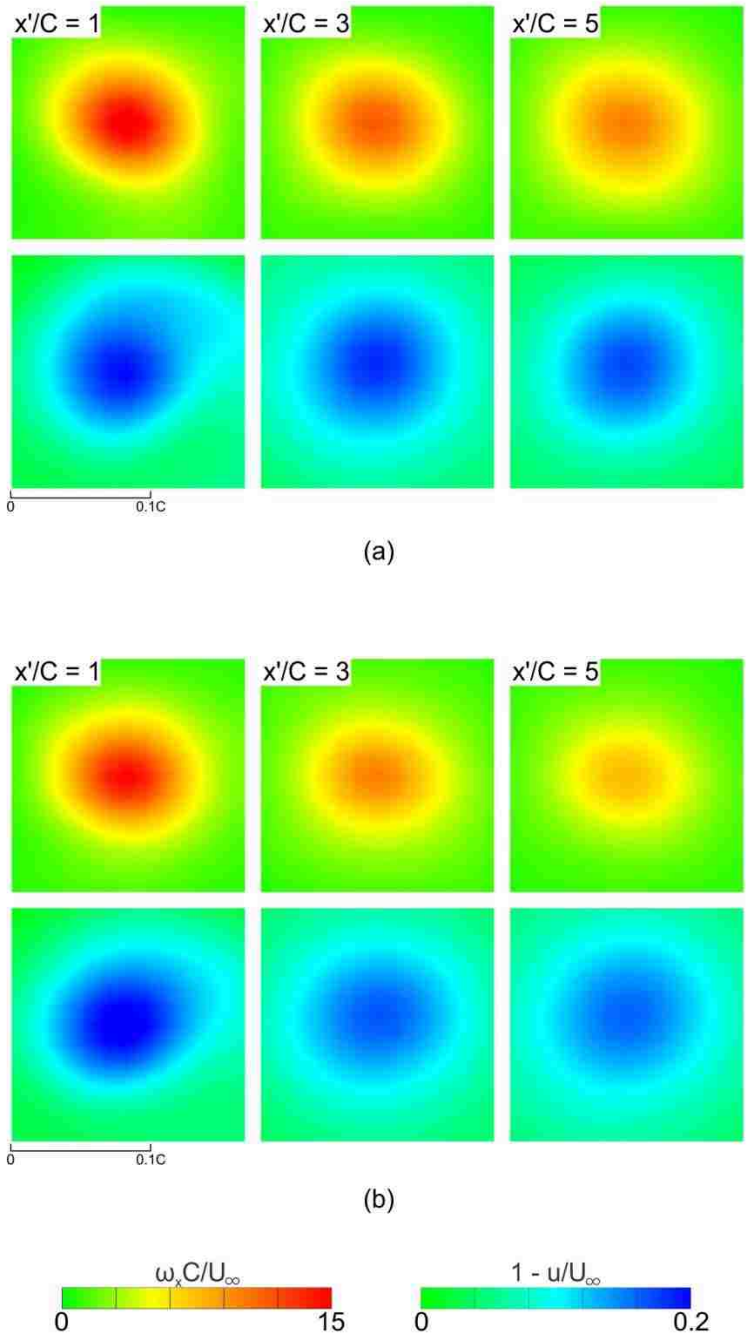


**Figure 3.9:** Comparison of sectional cuts of axial vorticity $\omega_x C/U_\infty$ and axial velocity deficit $1 - u/U_\infty$ as functions of streamwise distance $x'/C$ for the (a) unperturbed and (b) perturbed vortex.

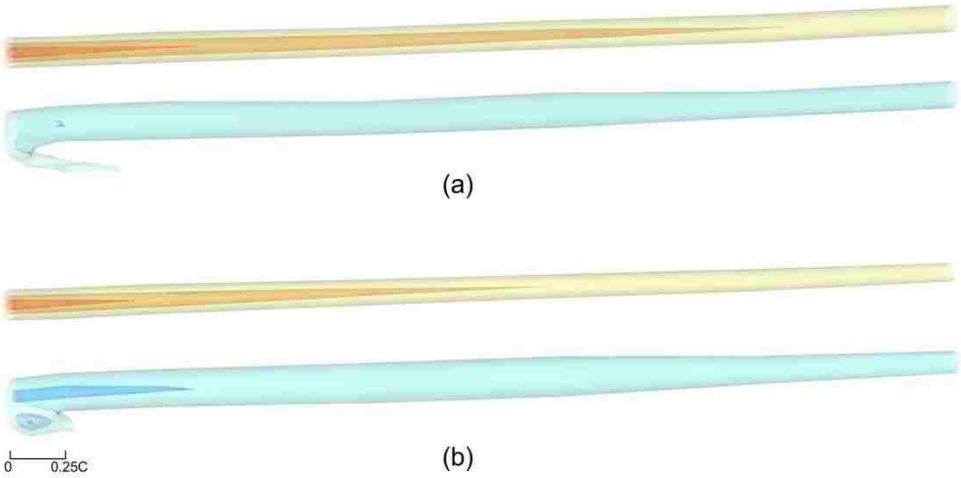


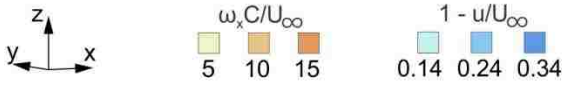


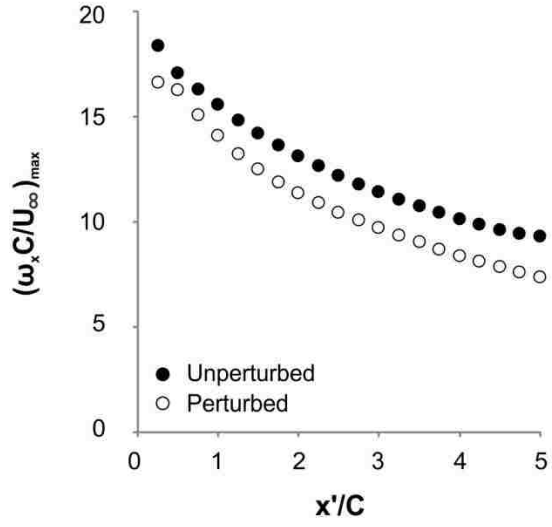


(c)

**Figure 3.10:** Iso-surfaces of axial vorticity $\omega_x C/U_\infty$ and axial velocity deficit $1 - u/U_\infty$ for the (a) unperturbed and (b) perturbed vortex. (c) Plot of peak axial vorticity for the unperturbed and perturbed vortices.

# CHAPTER 4

# ONSET OF ORBITAL MOTION IN A TRAILING VORTEX FROM AN OSCILLATING WING

## 4.1 INTRODUCTION

### *4.1.1 Objectives*

The foregoing investigations, indicated in Chapter 1, have provided valuable insight into the structure of a perturbed trailing vortex. However, a number of issues remain unresolved and lead to experimental characterization via global imaging of the unsteady flow structure of a perturbed trailing vortex from a wing subjected to small amplitude periodic motion in the heaving mode. The focus of this chapter is on the following unexplored aspects: (i) the effect of dimensionless oscillation frequency on the distributions of axial vorticity, azimuthal vorticity and axial velocity deficit; (ii) characterization of the nature of the vortex trajectory including the development of orbital motion and its evolution in the streamwise direction; (iii) the interrelationship between the onset of orbital motion and patterns of axial vorticity, azimuthal vorticity and axial velocity deficit; and (iv) the connection between the foregoing aspects and the time-dependent variation of the swirl ratio. These concepts are addressed via volumetric and

cross-sectional representations of the vortex structure acquired from stereo particle-image velocimetry (SPIV) in conjunction with three-dimensional reconstruction techniques.

### *4.1.2 Overview*

The onset and development of orbital motion of a trailing vortex from a wing undergoing small amplitude heaving motion is investigated using stereo particle image velocimetry in conjunction with three-dimensional reconstruction techniques. The effect of Strouhal number is examined via space-time representations of axial and azimuthal vorticity, axial velocity deficit and swirl ratio. At low Strouhal number, the undulation of the vortex remains unidirectional with no amplification in the streamwise direction. In contrast, at high Strouhal number, the amplitude of vortex undulation can increase up to a factor of ten in the streamwise direction. These large amplitudes occur during orbital motion of the vortex. Irrespective of the value of either the Strouhal number of excitation or the streamwise location along the undulating vortex, generic physical mechanisms occur. Changes in curvature along the vortex are closely related to changes in the axial velocity deficit, extreme values of axial vorticity and swirl ratio, and the onset and attenuation of pronounced azimuthal vorticity.

## 4.2 EXPERIMENTAL SYSTEMS AND TECHNIQUES

Experiments were performed in a large-scale, recirculating water channel in the fluids laboratory at Lehigh University. The main test section of the facility is 594 mm in

depth and 613 mm in width. Flow conditioners, which include a series of honeycomb meshes and fine screens, are arranged upstream of the test section and are utilized to achieve a turbulence intensity less than 0.3 percent. In the present experiments, the freestream velocity was maintained at $U_\infty$ = 152.4 mm $s^{-1}$ which yields a chord based Reynolds number $Re_C = U_\infty C/\nu$ = 15200, where C is the chord of the wing and ν is the kinematic viscosity of water.

A stereoscopic particle image velocimetry system was utilized to determine the flow structure of a trailing vortex from a wing undergoing continuous heaving motion subjected to different oscillation frequencies. A schematic of the system is given in Figure 4.1a. A laser sheet oriented in the spanwise, or lateral, direction, in conjunction with two charged coupled device (CCD) cameras, are used to capture the three-dimensional velocity field at successive crossflow planes. Further details on the SPIV system is indicated in Chapter 2.

A schematic of the wing oscillation mechanism is indicated in Figure 4.1b. It employs a computer-controlled motor that drives a scotch-yoke mechanism that is attached to the vertically-oriented sting of the wing. The sting is affixed to the center of the wing and also fastened to a sliding bar coupled to a vertically-oriented traverse. A connecting rod is used to link the sliding bar to a wheel that is attached to the motor. This mechanism converts the linear motion to rotational motion. An encoder attached to the motor is used to determine the position of the wing.

Figure 4.1c is a rendered model of the test section that includes the SPIV system, the wing perturbation mechanism and the wing positioning system. The laser head is positioned underneath the channel and the laser sheet is oriented in the spanwise direction. The wing positioning system consists of several motors with encoders that allow for precise positioning of the wing in all three directions. This system also provides controlled perturbation of the wing. In order to capture images at successive planes in the streamwise direction, the motion control system is translated along a rail system that extends the length of the channel.

Figure 4.2a shows plan and side view schematics of the experimental system. The model of the wing is a rectangular flat plate of aspect ratio $AR$ = 2, with a chord $C$ = 102 mm and span $b$ = 203 mm. The thickness of the wing $t$ = 1.6 mm and the corner radius $r_c$ = 0.5mm. The wing is fixed at an angle of attack $\alpha_o$ = 6° and is subjected to continuous heaving motion in the vertical direction as indicated in the side view schematic. Figure 4.2b depicts the sinusoidal displacement amplitude $A(\Phi)$ of the wing as a function of phase angle $\Phi$. The oscillation cycle consists of the downstroke of the wing which occurs between $\Phi = 0$ to $\Phi = \pi$ and the upstroke between $\Phi = \pi$ to $\Phi = 2\pi$.

Three frequencies of motion were employed in the present experiments. The non-dimensional Strouhal numbers, indicated in Figure 4.2b, are $St_c = fC/U_\infty$ = 0.08, 0.25 and 0.67. These values of Strouhal number correspond respectively to values of wavelength $\lambda/C = U_\infty/fC$ = 12, 4 and 1.5 or $\lambda/d_o$ = 120, 40 and 15 where $d_o$ is the diameter of the vortex from a stationary wing. The vortex diameter $d_o$ is defined as twice the vortex radius $r_o$, where $r_o$ is the circumferentially averaged radial location of the maximum value

of swirl velocity $(u_\theta)_{max}$. The displacement amplitude of the wing motion in all cases is $A_o/C$ = 0.03 or $A_o/d_o$ = 0.3. The extreme values of Strouhal number represent the limiting frequencies of the motor control system. Preliminary diagnostics showed that the lowest value yielded unidirectional undulation to the vortex with no change in amplitude in the streamwise direction, thereby serving as a reference case. Moreover, the moderate and highest values $St_C$ correspond to large amplification of the nonlinearly perturbed vortex, in accord with the theory and computations of Viola et al. (2016). Additionally, the opposite tip vortex was investigated at all Strouhal numbers and the vortex behavior was symmetrical to the opposite tip vortex in all cases. Namely, the differences in peak values of axial vorticity and velocity of the two vortices were within experimental error and the trajectories of orbital motion, or lack thereof, were symmetrical.

The water is seeded with 11 μm metallic coated hollow plastic spheres which have a density of 1.958 g/cm$^3$. A dual pulsed Nd:YAG laser system is utilized to generate a laser sheet of 1.5 mm thickness which illuminates the particles. Each of the CCD cameras used to capture the particle images contains an array of 1600 pixels × 1192 pixels. Insight 4G was employed to process the particle images. Interrogation windows of 32 pixels × 32 pixels are used and contain 15-20 particle images. A 50% overlap between camera frames is utilized and the particle images are processed using a frame-to-frame cross-correlation technique. The effective resolution of the SPIV system employed is 14.92 pixels mm$^{-1}$. Information on the error analysis of the SPIV system can be found in Chapter 2.

During experiments, the laser sheet was oriented in the crossflow direction, as previously indicated. Images were acquired at the following selected planes: $x'/C$ = 0, 0.5, 1, 2, 3, 4 and 5; these values correspond to the distance downstream of the trailing edge of the wing, where $x'/C$ = 0 is the trailing edge. A phase-referencing technique was employed, which grouped together images taken at a given vertical position of the wing; this process provided phase-averaged images. Instantaneous vortex centers were made coincident before performing phase-averaged calculations, to eliminate the effects of meandering. Time-average calculations were also performed. That is, averages were taken over the entire oscillation cycle. For these calculations, instantaneous images were also re-centered before taking the average. This procedure is well-established and accepted, as described in detail by del Pino et al. (2011). Volumetric reconstruction was performed utilizing in-house software in conjunction with the phase-averaged images.

## 4.3 UNSTEADY VORTEX STRUCTURE

### *4.3.1 Time-Averaged Axial and Azimuthal Profiles*

Figure 4.3 shows: time-averaged profiles of azimuthal velocity $u_\theta/(u_\theta)_{max}$ as a function of radius $r_o$; and axial velocity deficit $(U_\infty - u)/(U_\infty - u_{max})$ as a function of the radial half-width $r_{1/2}$. These profiles are shown at (a) $St_C$ = 0.08, (b) $St_C$ = 0.25 and (c) $St_C$ = 0.67. The vortex radius $r_o$ is defined as the radial location where maximum azimuthal velocity $(u_\theta)_{max}$ occurs and the radial half-width $r_{1/2}$ is defined as the location where the axial velocity deficit is half of its maximum value. Profiles are given for the streamwise

locations $x'/C$ = 0.5, 1, 2, 3, 4 and 5. For each case, the radial distributions have been circumferentially averaged. Profiles of the theoretical distributions of Moore & Saffman (n = 0.7) (1973) and the Batchelor q-vortex (1964) are plotted for comparison. Overall, the time-averaged, normalized distributions of azimuthal and axial velocity for the three cases are in general agreement with each other at $x'/C$ = 0.5 and also agree well with the profiles of the stationary vortex, shown in Fishman et al. (2017). Moreover, they compare well with the theoretical distributions of Moore & Saffman (1973), despite the unsteady fluctuations.

With increasing streamwise distance, departures from these theoretical profiles occur for all Strouhal numbers. In the azimuthal velocity profiles, they occur at the outer periphery of the vortex, from $r/r_o$ = 1.5 to $r/r_o$ = 2, where elevated values of azimuthal velocity, relative to the theoretical profiles, are evident and are most pronounced at $St_C$ = 0.67. There are similar departures, in the form of elevated values of the data, at the outer periphery of the vortex from the Moore & Saffman profile of axial velocity deficit for streamwise distances greater than $x'/C$ = 0.5. These departures are likely attributed to the large variations during the oscillation cycle of the scale and magnitude of the axial velocity deficit of the vortex, especially at larger streamwise distances, which are shown subsequently in Figure 4.6a and Figure 4.6b. Since these variations of the velocity deficit are associated with nonlinear effects, the resultant averaged, normalized profiles are distorted relative to those corresponding to an unperturbed vortex or a vortex perturbed at small amplitude. It should also be emphasized that the comparison of the theoretical distributions with the data has not been optimized through selection of different values of

constants for the theoretical distributions shown in Figure 4.3. This aspect, which is rigorously addressed by del Pino et al. (2011) for the case of an unperturbed vortex, is beyond the scope of the present investigation. Nonetheless, the present observations establish the manner in which the time-averaged vortex structure is distorted at successive streamwise locations.

*4.3.2 Initial State of Vortex at Trailing Edge*

Figure 4.4 shows cross-sectional slices of axial vorticity $\omega_x C/U_\infty$ (red) and axial velocity deficit $1 - u/U_\infty$ (blue) as functions of phase angle $\Phi$ for each value of Strouhal number $St_c$. These images were taken at the trailing edge of the wing and are viewed looking upstream along the axis of the vortex. The darkest blue, wedge-like region of axial velocity deficit near the bottom of each image corresponds to the horizontal wake at the trailing edge. For the low Strouhal number, $St_C = 0.08$, the vortex exhibits mild fluctuations of magnitude and spatial extent, or scale, of axial vorticity and axial velocity deficit during the oscillation cycle. The structure of the axial velocity deficit during the downstroke, $\Phi = 0$ to $\Phi = 3\pi/4$, is nearly symmetrical to that of the upstroke, $\Phi = \pi$ to $\Phi = 7\pi/4$. This is not the case for axial vorticity; that is, an increase in level of axial vorticity is evident from $\Phi = 0$ to $\Phi = 3\pi/4$, in comparison to that of $\Phi = \pi$ to $\Phi = 7\pi/4$. For the moderate Strouhal number $St_C = 0.25$, pronounced variations of the magnitude and scale of both the axial vorticity and axial velocity deficit are evident during the oscillation cycle. Enhanced levels of axial vorticity occur during the downstroke and attenuated levels are apparent during the upstroke. Regarding the axial velocity deficit, enhanced levels occur during the downstroke and attenuate during the upstroke. For the

highest Strouhal number, $St_C$ = 0.67, contours of both axial vorticity and axial velocity deficit are highly distorted along the wing surface from $\Phi = \pi/4$ to $\Phi = 3\pi/4$. This distortion is not present at the lower values of Strouhal number, i.e., $St_C$ = 0.08 and $St_C$ 0.25. At $\Phi = \pi$, the vortex is positioned well above the wing surface and has initiated its recovery towards circular concentrations of axial vorticity and axial velocity deficit. In contrast to the aforementioned cases at lower frequencies, the vortex exhibits lateral motion in addition to the vertical excursion which arises from the prescribed vertical heaving motion of the wing. This is evident from comparison of the location of the vortex center relative to the tip of the wing at different values of phase angle. Specifically, from $\Phi = \pi$ to $\Phi = 7\pi/4$ the vortex center location moves further outboard and then back inboard from $\Phi = 0$ to $\Phi = 3\pi/4$. The consequence of these simultaneous lateral and vertical excursions is a small amplitude orbital motion at the trailing edge of the wing, which is present only at the highest value of Strouhal number.

Figure 4.5 shows streamline patterns at the trailing edge of the wing, $x'/C = 0$, for all three values of Strouhal number $St_C$. Two phase angles, $\Phi = \pi/4$ and $\Phi = 5\pi/4$, are indicated for each case. The vortex is centered in all images. Corresponding images of axial vorticity and axial velocity deficit are previously given in Figure 4.4. In the first row of images of Figure 4.5, corresponding to $St_C$ = 0.08, the streamline patterns spiral inwards towards a central focus, which corresponds to the center of the vortex. The dark region near the center of the vortex, corresponding to densely packed streamlines, is approximately circular. This is the case at both phase angles. Similar streamline patterns are observed at $St_C$ = 0.25. As previously indicated in Figure 4.4, at $St_C$ = 0.08 and $St_C$ =

0.25, patterns of axial vorticity and axial velocity deficit are undistorted, circular concentrations. The fact that the streamlines at both frequencies spiral inward makes the focus stable and indicates that the vortex is being stretched in the axial direction, in accord with the interpretation of Perry and Chong (2000). Moreover, at both of these frequencies, the vortex trajectory during the oscillation cycle is entirely unidirectional (in the vertical direction) and the formation of the vortex is not inhibited by the motion of the wing.

At $St_C = 0.67$, the streamline patterns spiral inwards towards a central focus at $\Phi = \pi/4$. The non-circular (elongated) dark regions of densely packed streamlines near the center of the vortex coincide with the elongated patterns of axial vorticity and axial velocity deficit along the surface of the wing as indicated in Figure 4.4. However, the streamline topology at $\Phi = 5\pi/4$ has undergone a fundamental transformation relative to that at lower values of Strouhal number. It consists of streamlines spiraling inwards towards a central focus at the center of the vortex; they emanate from a limit cycle. The streamlines that spiral outwards from this limit cycle merge along a secondary limit cycle. This pattern differs from the classical streamline pattern of vortex roll-up and indicates a change in the mechanism of vortex formation in the vicinity of the wing. It arises when there is a detectable phase shift between the vortex formation and the motion of the wing. This phase shift is associated with small amplitude lateral motion of the forming vortex, which represents the onset of orbital motion.

*4.3.3 Sectional Patterns of Axial Vorticity, Axial Velocity Deficit and Azimuthal Vorticity*

Figure 4.6a and Figure 4.6b show rows of images representing cross-sectional slices of axial vorticity $\omega_x C/U_\infty$ (top), axial velocity deficit $1 - u/U_\infty$ (middle) and azimuthal vorticity $\omega_\theta C/U_\infty$ (bottom) as functions of phase angle $\Phi$. Three different Strouhal numbers $St_C$ are represented at the streamwise locations $x'/C = 0.5$ and $x'/C = 2$. At the low Strouhal number, $St_C = 0.08$, the vortex exhibits similar characteristics as it does at the trailing edge of the wing. That is, mild variations of magnitude and spatial extent, or scale, of axial vorticity and axial velocity deficit occur. Azimuthal vorticity is detectable at all values of phase angle, but is most prevalent when the axial velocity deficit has the largest magnitude and scale, as well as, a steeper gradient in the radial direction; for example, from $\Phi = 3\pi/2$ to $\Phi = \pi/4$ at $x'/C = 0.5$ and $\Phi = \pi/2$ to $\Phi = \pi$ at $x'/C = 2$.

At the moderate Strouhal number, $St_C = 0.25$, represented by the middle set of images in each figure, considerable variations of the magnitude and scale of axial vorticity and axial velocity deficit are evident over the oscillation cycle. Pronounced regions of azimuthal vorticity are evident in conjunction with regions of enhanced axial velocity deficit. At the high Strouhal number, $St_C = 0.67$, corresponding to the bottom set of images, substantial variations of axial vorticity and axial velocity deficit occur. Similar to the lower values of Strouhal number, enhanced levels of azimuthal vorticity coincide with regions of enhanced axial velocity deficit. The scale of the concentration of axial velocity deficit is much larger than that of axial vorticity at both the moderate and high

Strouhal numbers, in contrast to the patterns at low Strouhal number. The foregoing observations are consistent at all streamwise locations explored in this investigation.

In summary, clearly defined azimuthal vorticity occurs in conjunction with regions of enhanced axial velocity deficit during the oscillation cycle across all streamwise distances and for all oscillation frequencies imparted by the wing motion. This observation is consistent with that first described by Fishman et al. (2017) at a single frequency. The present findings indicate a universal occurrence extending over a range of $St_C$ = 0.08, 0.25 and 0.67, corresponding to ratios of wavelength $\lambda$ to vortex diameter $d_o$ of $\lambda/d_o$ = 120, 40 and 15. Moreover, these observations are consistent with the criterion described by Fishman et al. (2017), whereby pronounced azimuthal vorticity is generated when the swirl ratio $q < \sqrt{2}$ during the oscillation cycle. The swirl ratio is defined as $q = \Gamma/2\pi r\Delta u = 1.567V_\theta/\Delta u$, where $V_\theta$ is the maximum azimuthal velocity and $\Delta u$ is the peak axial velocity deficit of the vortex, as indicated by Jacquin & Pantano (2002). In turn, this finding is in accord with the onset of amplified azimuthal modes of the convective instability of the Batchelor vortex described by Leibovich and Stewartson (1983). Although the swirl ratio criterion described by Leibowich & Stewartson (1983) was developed from a parallel (columnar) Batchelor vortex, there is strong correspondence between it and the prominent physics of the present perturbed vortices. Figures 4.6a and 4.6b indicate, however, important distinctions of the vortex response that are frequency dependent.

*4.3.4 Volumetric Representations of Flow Structure – Axial Vorticity, Axial Velocity Deficit and Azimuthal Vorticity*

Figure 4.7a shows temporal volumes of cross-sectional slices of axial vorticity $\omega_x C/U_\infty$ and azimuthal vorticity $\omega_\theta C/U_\infty$ superposed on an iso-surface (blue) of axial velocity deficit $1 - u/U_\infty$ at the streamwise location $x'/C = 0.5$. At each value of Strouhal number $St_C$, the top and bottom images show, respectively, sectional contours of $\omega_x C/U_\infty$ and $\omega_\theta C/U_\infty$. Images are shown from an angled side view as indicated in the schematic. Linear interpolation between data planes is utilized in the construction of these temporal volumes. At the low Strouhal number $St_C = 0.08$, a small diameter region of high-level axial velocity deficit penetrates the cross-sectional contours of axial vorticity over a portion of the oscillation cycle. The existence of the iso-surface of velocity deficit coincides with occurrence of detectable azimuthal vorticity along the top portion of the vortex. At the moderate Strouhal number $St_C = 0.25$, the region of axial velocity deficit is relatively large compared to that at the low Strouhal number. Furthermore, slices of enhanced azimuthal vorticity are evident only in the region where axial velocity deficit is present. These features are also apparent at the high Strouhal number, $St_C = 0.67$. The iso-surface of axial velocity deficit is largest in this case and is again accompanied by enhanced levels of azimuthal vorticity. Larger fluctuations in axial vorticity with increasing Strouhal number are evident.

Figure 4.7b shows the equivalent temporal volumes at the streamwise location $x'/C = 2$. The format of the image layout is the same as that of Figure 4.7a. At all three frequencies, the previously established relationship is apparent. That is, the region of

axial velocity deficit coincides with enhanced levels of azimuthal vorticity. At $St_C = 0.08$, a narrowly confined region of high level axial velocity deficit occurs. On the other hand, it is clear that at $St_C = 0.25$ and $St_C = 0.67$, large-scale regions of high level axial velocity deficit arise.

An important aspect of the tip vortex from an oscillating wing is whether its response takes the form of a unidirectional undulation or an orbital motion. Figures 4.8 through 4.10 show the interrelationship between axial vorticity, axial velocity deficit and curvature of the undulating vortex. Figures 4.8 shows, at the low Strouhal number, $St_C = 0.08$, temporal volumes of cross-sectional slices of axial vorticity $\omega_x C/U_\infty$ (red) overlaying iso-surfaces of axial velocity deficit $1 - u/U_\infty$ (blue) for streamwise distances $x'/C = 0.5$, 3 and 5. The schematic indicates the perspectives for the angled side and plan views.

In Figure 4.8, at $x'/C = 0.5$, close to the trailing edge of the wing, it is evident that enhanced levels of axial velocity deficit $1 - u/U_\infty$ are present only over a portion of the cycle. This is clear in both the side and plan views. The side view shows this deficit, represented by the blue iso-surface, which occurs in the center of the vortex at the onset of the change in vortex curvature. That is, the vortex begins to slope downward at $\Phi = 0$, in conjunction with occurrence of the iso-surface of axial velocity deficit. This iso-surface is attenuated where the vortex begins to slope upward. With increasing streamwise distance, from $x'/C = 0.5$ to $x'/C = 3$, the spatial extent of the axial velocity deficit is greatly attenuated and there is a discernable phase shift in its temporal location relative to that of $x'/C = 0.5$. This shift is due to the phase velocity of the disturbed

vortex, which is of the order of the freestream velocity. At large streamwise distances, $x'/C = 5$, there is no detectable level of this high-level axial velocity deficit. As evident in the side view images, there is no discernable change in the amplitude of the vertical excursion of the concentrations of axial vorticity at increasing values of streamwise distance $x'/C$. Moreover, the plan view images show that there is no lateral excursion of the vortex for all streamwise locations.

Figure 4.9a and Figure 4.9b show, at the moderate Strouhal number $St_C = 0.25$, temporal volumes of cross-sectional slices of axial vorticity $\omega_x C/U_\infty$ superposed on iso-surfaces of axial velocity deficit $1 - u/U_\infty$. At $x'/C = 0.5$, high-level axial velocity deficit occurs in the vortex core during a majority of the cycle. The concentration of axial velocity deficit is evident at all streamwise distances; however, it extends over a smaller number of phases of the oscillation cycle with increasing values of $x'/C$. At a given value of $x'/C$, the formation of this iso-surface of axial velocity deficit coincides with a change of curvature of the vortex, and the attenuation of the iso-surface corresponds to another change of curvature. Primarily, the iso-surface forms along the downward sloping portion of the vortex and is attenuated on the upward sloping portion. This behavior is consistent with the state of the vortex at the trailing edge of the wing as shown in Figure 4.4. That is, higher magnitude axial velocity deficit, as well as axial vorticity, is present along the downward deflection of the vortex trajectory. At $x'/C = 1$, in the side view, at $\Phi = 0$ the slices of axial vorticity initially slope upward. As these slices begin to slope downward, formation of enhanced axial velocity deficit is apparent. The change in curvature, that is, where the vortex changes from sloping upwards to sloping downwards, occurs in

conjunction with the formation of enhanced axial velocity deficit. On the other hand, as the cross-sectional slices of axial vorticity slope upwards, the high-level axial velocity deficit is attenuated. These changes in curvature are also associated with variations of the magnitude and spatial extent of axial vorticity, whereby an increase of the scale of axial vorticity coincides with enhanced axial velocity deficit. In Figure 4.9b, at $x'/C = 5$, these same characteristics hold. Although the spatial extent of the region of enhanced axial velocity deficit is attenuated, it still forms along the downward sloping portion of the vortex albeit slightly after the change in curvature. It is no longer present where the axial vorticity slices begin sloping upward, as is consistent with previous observations. In the plan view, lateral excursion of the axial vorticity slices is evident. These excursions can be seen as deviations from the original unidirectional trajectory and occur at the onset and attenuation of the axial velocity deficit. Viewing these vertical and lateral excursions together indicates an elliptical pattern in the vortex trajectory.

Figure 4.10a and Figure 4.10b, at the high Strouhal number $St_C = 0.67$, indicate substantial deviations from unidirectional undulation of the vortex. The vortex structure and its evolution in the downstream direction are dramatically affected. Large excursions in the vertical and lateral directions are evident across all streamwise distances in Figure 4.10a and Figure 4.10b and their amplitudes are significantly amplified with increasing $x'/C$. Additionally, this perturbation produces a large diameter iso-surface of axial velocity deficit that encloses the slices of axial vorticity; this observation is present at all streamwise distances. That is, a large-scale region of decelerated axial flow occurs, in contrast to aforementioned cases at lower frequencies, shown in Figure 4.8 and Figure 4.9

where the iso-surface of enhanced axial velocity deficit is embedded within the central region of the volume of axial vorticity slices. Furthermore, the formation of axial velocity deficit again occurs along the downward sloping portion of the slices of axial vorticity and is attenuated along the upward sloping portion of slices of axial vorticity. Lateral excursions of the vortex trajectory, which are evident in the plan view, depict a similar relationship.

*4.3.5 Evolution of Vortex Trajectory*

Figure 4.11a and Figure 4.11b indicate the degree of departure from a unidirectional undulation of the vortex via images that show the time-sequence of cross-sectional slices of axial vorticity $\omega_x C/U_\infty$ viewed in the upstream direction, such that all instantaneous slices are superposed during the oscillation cycle.

At $x'/C = 0.5$ in Figure 4.11a, the trajectory of the vortex at Strouhal numbers $St_C = 0.08$ and $St_C = 0.25$ is unidirectional and solely in the vertical direction. However, at $St_C = 0.25$, the vortex experiences larger fluctuations in scale. At $St_C = 0.67$, orbital motion of the vortex trajectory is clearly present and accompanied by large variations in scale. At $x'/C = 1$, there is relatively little change in the nature of the vortex trajectory for all three values of Strouhal number. At $x'/C = 2$, little change of the trajectory occurs, though attenuation of the magnitude of axial vorticity is apparent at $St_C = 0.08$. The development of lateral motion of the vortex is evident at $St_C = 0.25$; simultaneously, a small increase in the vertical amplitude of motion occurs. At $St_C = 0.67$, there is a significant increase in the amplitude of the vortex trajectory at $x'/C = 2$, in both vertical

and lateral directions. This observation is accompanied by severe changes in the magnitude and spatial extent of axial vorticity.

In Figure 4.11b, the trajectory of the vortex at $St_C$ = 0.08 does not change significantly for the streamwise distances $x'/C$ = 3, 4 and 5. At $St_C$ = 0.25, the amplitudes of the vertical and lateral excursions increase incrementally from $x'/C$ = 3 to $x'/C$ = 5, such that detectable orbital motion occurs. The motion of the vortex in this case is in the opposite sense to that of the axial vorticity; that is, it is oriented in the clockwise direction. At $St_C$ = 0.67, the trajectory of the vortex does not change significantly over the streamwise locations $x'/C$ = 3 to 5. Namely, the amplitudes in both the vertical and lateral direction remain relatively unchanged. In this case, the motion of the vortex is in the same sense as that of axial vorticity; specifically, it is in the counter-clockwise direction.

In essence, the three different Strouhal numbers $St_C$ yield distinctly different classes of response, i.e., trajectories. At the Strouhal number $St_C$ = 0.08, the vortex excursion begins and remains solely in the vertical direction and its amplitude does not change with streamwise distance. At the moderate Strouhal number $St_C$ = 0.25, the vortex excursion is initially unidirectional in the vertical direction, but develops a lateral component with increasing streamwise distance, resulting in orbital motion in the clockwise direction. Additionally, the direction of winding in the spatial direction is opposite to its winding in time; that is, the vortex winds in the counter-clockwise direction in space. At the high frequency $St_C$ = 0.67, the initial motion of the vortex is in both the vertical and lateral directions; in other words, orbital motion is present and is oriented in the counter-clockwise direction. At $St_C$ = 0.67, the vortex winds in the

opposite, clockwise, direction in space. Moreover, the amplitudes of the excursion in the vertical direction increase by nearly an order of magnitude along the streamwise extent of the vortex. At $St_C$ = 0.67, as described in conjunction with Figure 4.4 and Figure 4.5, the formation of the vortex at the trailing edge is associated with lateral perturbations that are 4% of the chord of the wing (40% of the effective diameter of the vortex) and arise from a phase lag of the vortex formation relative to the wing motion, which does not exist for lower oscillation frequencies of the wing. This initial motion of the vortex is the genesis of a well-defined orbital motion that undergoes large amplitude amplification with streamwise distance.

Figure 4.11c shows plots of vertical $A_z/C$ and lateral amplitude $A_y/C$ for the three Strouhal numbers $St_C$ as functions of streamwise distance $x'/C$. At $St_C$ = 0.08 the motion is entirely vertical with no significant increase in amplitude with streamwise distance. At $St_C$ = 0.25, the motion is initially vertical and its amplitude gradually increases until saturation is reached; simultaneously a lateral component of motion becomes more prevalent. At $St_C$ = 0.67, the vertical motion increases in amplitude with streamwise distance up to the location where saturation is attained, while the lateral motion remains significantly large at all streamwise locations. Saturation of the vertical amplitude of undulation occurs between $x'/C$ = 3 and $x'/C$ = 5 for the largest value of $St_C$ and between $x'/C$ = 4 and $x'/C$ = 5 for the moderate value of $St_C$. Amplitude saturation, which is due to the onset of nonlinear effects, is an inherent feature of unstable flows that may be linearly unstable in their initial region of development. Such flows include perturbed trailing vortices, as described in the theoretical and computational investigation of Viola et al.

(2016). In a more general sense, the onset of nonlinear saturation is evident in experimental investigations of free shear flows, for example, the case of a perturbed mixing layer investigated by Freymuth (1966).

In order to clarify the role of the swirl ratio $q$ during orbital motion of the vortex, Figure 4.12 shows patterns of the vortex trajectory for the case $St_C$ = 0.67 at the streamwise location $x'/C$ = 3. It indicates the time-sequence of cross-sectional slices of axial vorticity and, in addition, the lowest level contour of axial vorticity filled with a color that corresponds to the value of swirl ratio. The values of phase angle $\Phi$ correspond to specific instants during the cycle of the wing oscillation. A clear relationship between axial vorticity, swirl ratio and changes in vortex trajectory is evident. Most notably, changes in the direction of the vortex motion are evident where the swirl ratio reaches maximum (red) and minimum (green) values. Additionally, maximum values of swirl ratio are attained in conjunction with the attenuation of axial vorticity. This indicates that the axial velocity deficit is the dominant parameter in the swirl ratio and the predominant cause of short-wave instability. Conversely, minimum values of swirl ratio are attained in conjunction with increased strength of axial vorticity.

### *4.3.6 Volumetric Representations of Flow Structure – Axial Vorticity, Axial Velocity Deficit and Swirl Ratio*

Figure 4.13a shows temporal volumes of cross-sectional slices of axial vorticity $\omega_x C/U_\infty$ colored by swirl ratio $q$ with overlaying iso-surfaces of axial velocity deficit $1 - u/U_\infty$ at a streamwise distance $x'/C$ = 0.5. Each Strouhal number $St_C$ is depicted in both

side and plan view orientations as indicated in the schematic. At $St_C$ = 0.08, the swirl ratio does not vary significantly with respect to phase angle $\Phi$ and the trajectory of the vortex is solely in the vertical direction, as previously indicated. Higher values of swirl ratio are attained in regions where there is no significant axial velocity deficit. In general, the time sequence of axial vorticity slices slopes downward with increasing swirl ratio, and slopes upward with increasing swirl ratio. At $St_C$ = 0.25, a similar relationship between vortex curvature and swirl ratio is evident, whereby changes in vortex curvature coincide with regions of minimum and maximum values of swirl ratio. Moreover, in this case, larger fluctuations in swirl ratio are apparent, relative to those at $St_C$ = 0.08. The most pronounced changes in curvature and swirl ratio are apparent at the highest dimensionless frequency $St_C$ = 0.67. The magnitude of $q$, represented by the red contours, greatly exceeds the maximum color bar value of 4, and can reach upwards of 20. In the side view, the cross-sectional slices slope downwards with decreasing values of swirl ratio and the formation of the axial velocity deficit occurs. When the cross-sectional slices slope upward, the value of swirl ratio increases in conjunction with the attenuation of the axial velocity deficit. In the plan view, the vortex deflects upwards (representing a lateral deflection in the actual flow) where high level swirl ratio occurs. A pronounced change in curvature is evident at the onset of the enhanced axial velocity deficit which corresponds to a drastic decrease in swirl ratio.

Figure 4.13b shows similar representations as Figure 4.13a, but at a streamwise distance $x'/C$ = 3. At $St_C$ = 0.08, the swirl ratio does not vary significantly with respect to phase angle and the trajectory of the vortex is solely in the vertical direction, as

previously shown at $x'/C$ = 0.5 in Figure 4.13a. Again, higher values of swirl ratio are attained in regions where there is no significant axial velocity deficit. At $St_C$ = 0.25, it is clear that changes in swirl ratio corresponding to changes in curvature. That is, in the side view, increasing swirl ratio coincides with upward sloping cross-sectional slices. Conversely, decreasing values of swirl ratio coincide with downward sloping cross-sectional slices, in conjunction with the onset of axial velocity deficit. These observations are consistent with the plan and side view temporal volumes at, $St_C$ = 0.67 where remarkably large deflections occur. For the foregoing observations, it is important to note that, for each Strouhal number, the flow structure is preserved at locations downstream of the trailing edge of the wing. That is, the changes in curvature in relation to swirl ratio are consistent at each streamwise location.

## 4.5 CONCLUSIONS

This investigation focuses on the unsteady structure of a trailing vortex from a wing undergoing small amplitude heaving motion. Space-time images acquired via stereo particle image velocimetry show the effect of Strouhal number $St_C$ (dimensionless frequency) on the response of the vortex in relation to the onset of its orbital motion. Low, moderate, and high Strouhal numbers correspond respectively to values of $St_C$ = 0.08, 0.25 and 0.67. The amplitude $A_o$ of the wing motion is approximately two orders of magnitude smaller than the chord. Over this range of Strouhal number, the vortex trajectory exhibits markedly different trajectories. Nevertheless, there are a number of

generic physical mechanisms of the perturbed vortex that can be interpreted in terms of space-time representations of axial and azimuthal vorticity, axial velocity deficit and swirl ratio.

At low Strouhal number, the amplitude of the unidirectional excursion of the vortex remains essentially constant with streamwise distance and has a magnitude of the order of the amplitude of the wing oscillation. At moderate Strouhal number, the initial region of the vortex motion is unidirectional, but at larger streamwise distance, excursions of the vortex occur orthogonal to its initial unidirectional motion, thereby giving rise to an elliptical orbital trajectory that acts in the opposite direction to that of the circulation of the vortex. Hama & Nutant (1961), Hama (1962) and Hama (1963) demonstrate that self-induction effects occur in accord with induced velocity, which is most prominent in the region with the largest curvature along a curved vortex and likely influence this development in association with the other vortex dynamics. At the high Strouhal number, the amplitude of the vortex undulation increases by nearly an order of magnitude with streamwise distance, with respect to the imposed perturbation, and pronounced orbital motion of the vortex has the same sense as the vortex circulation at all streamwise distances. The genesis of orbital motion is small amplitude lateral motion of the forming vortex at the trailing edge of the wing during its controlled vertical motion; moreover, the phase shift of the vortex development relative to the wing motion is altered with respect to that at lower values of Strouhal number. In both of the cases where orbital motion occurs, the region of axial velocity deficit is large compared to the region of axial

vorticity. In general, a combination of the foregoing mechanisms is present in the onset of orbital motion in these cases.

Irrespective of the value of the Strouhal number or the streamwise location along the vortex, several generic physical mechanisms occur along an undulating vortex. A change in vortex curvature coincides with the onset of an enhanced axial velocity deficit in the central region of the vortex; a subsequent change in curvature occurs when this elevated deficit is attenuated. These changes are evident at the trailing edge of the wing and are consistent at all streamwise distances in accord with strengthening and weakening of the vortex. Furthermore, changes in vortex curvature, or deflection, are similarly correlated with extreme values of axial vorticity and swirl ratio, as well as with the onset and attenuation of pronounced azimuthal vorticity. Onset of pronounced azimuthal vorticity coincides with regions of enhanced axial velocity deficit at the trailing edge of the wing and at all streamwise distances for all frequencies. It consistently occurs when the swirl ratio $q < \sqrt{2}$, in accord with onset of convective instability of azimuthal modes Leibovich and Stewartson (1983). The degree to which the value of swirl ratio varies during the undulation cycle of the vortex is directly related to the excitation frequency; that is, higher frequencies produce larger variations.

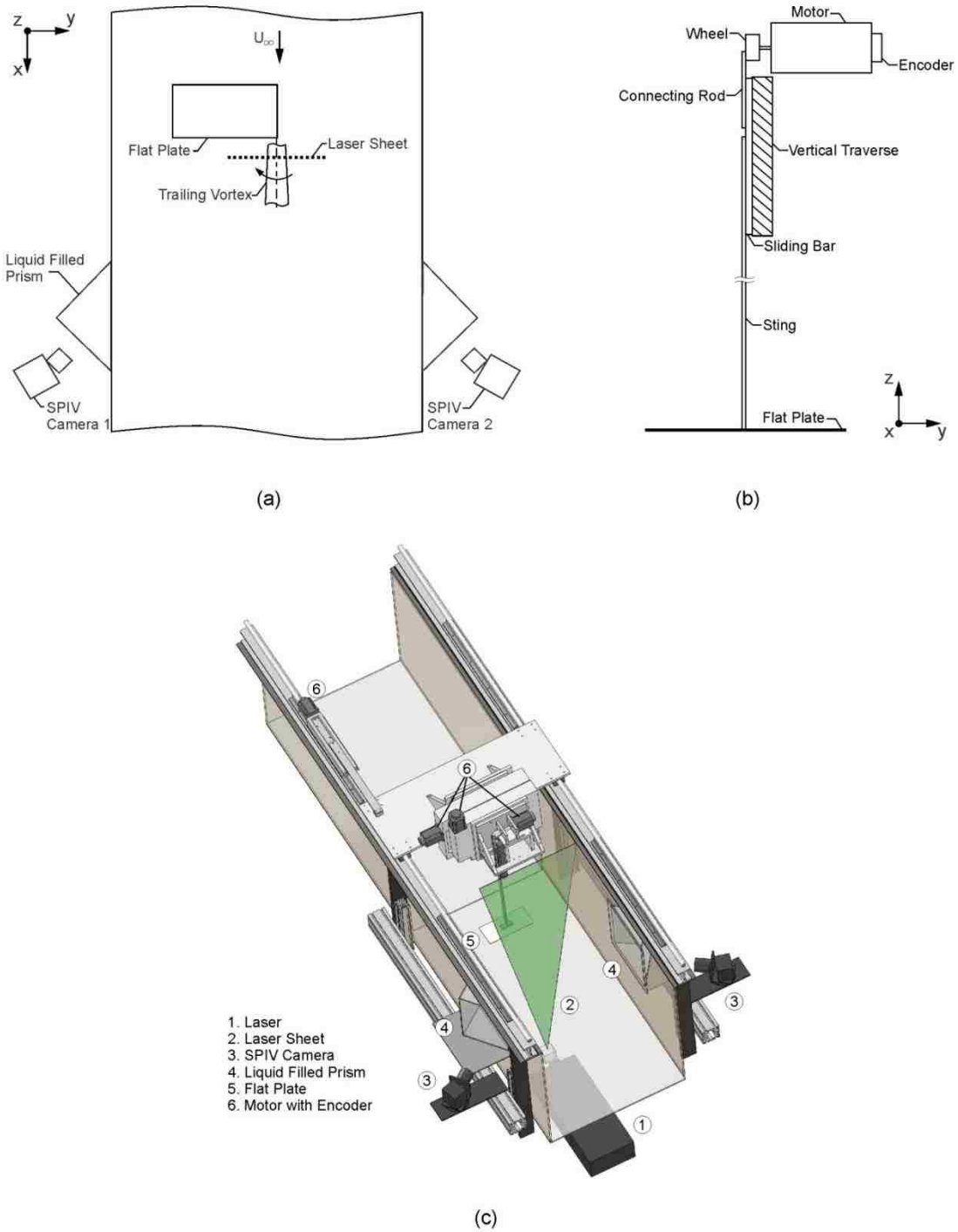


**Figure 4.1:** Overview of experimental apparatus. (a) Schematic of stereo particle image velocimetry system. (b) Schematic of wing oscillation mechanism (not to scale). (c) Model of test section and experimental system.

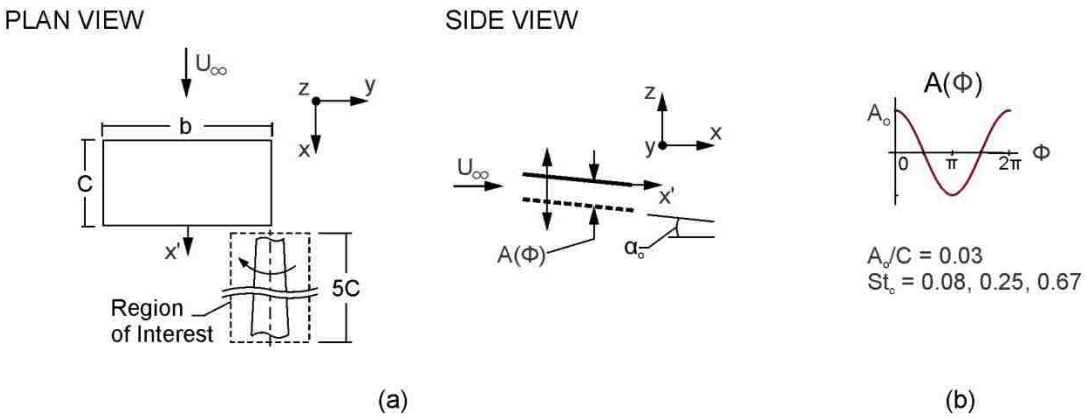


**Figure 4.2:** Overview of wing setup. (a) Plan and side view schematics of wing. (b) Motion profile of wing.

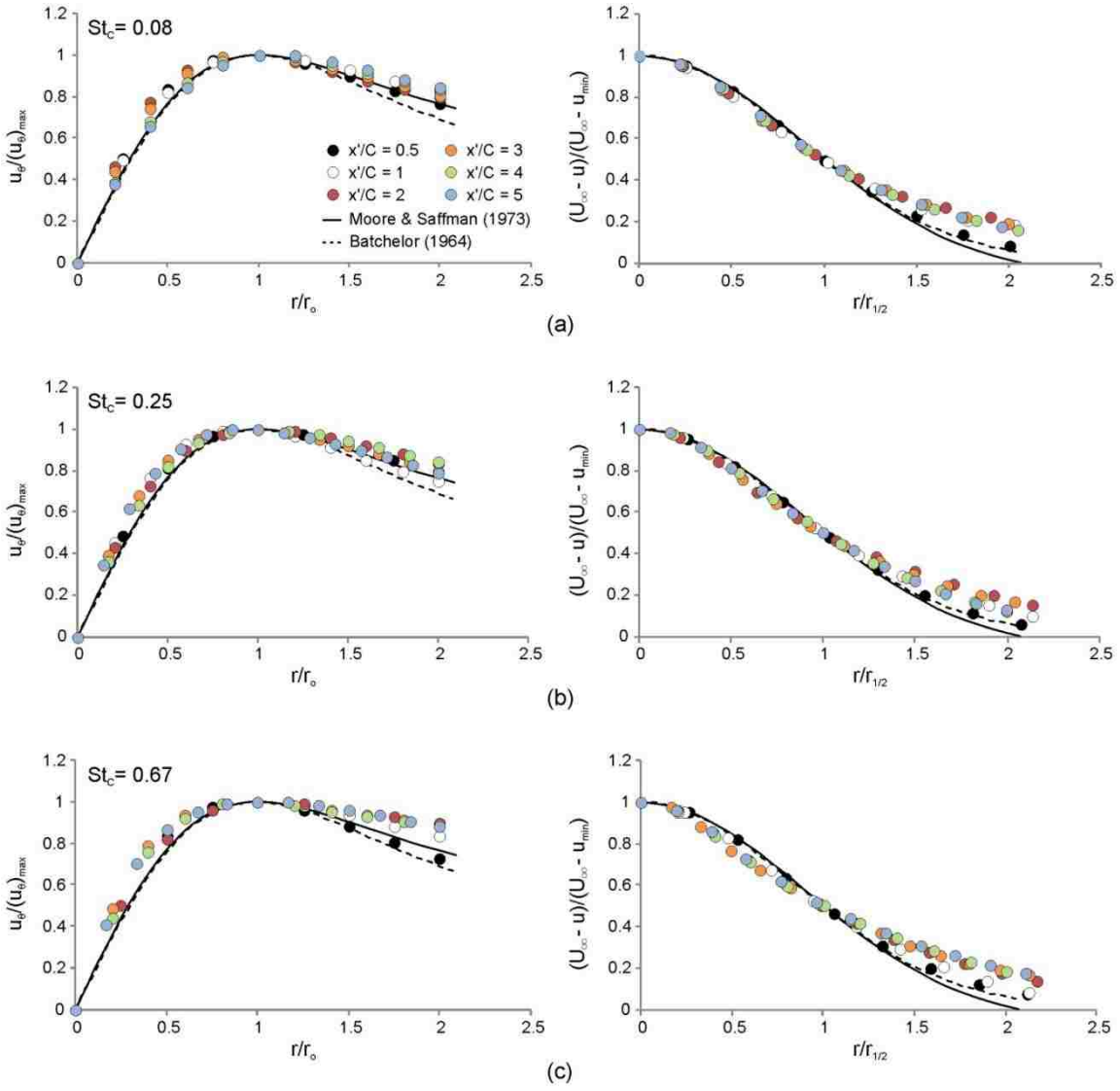


**Figure 4.3:** Comparison of time-averaged, normalized azimuthal velocity $u_\theta/(u_\theta)_{max}$ profiles as functions of vortex radius $r_o$ (left) and time-averaged, normalized axial velocity deficit $(U_\infty - u)/(U_\infty - u_{min})$ as functions of the radial half-width of the vortex $r_{1/2}$ (right) at Strouhal number (a) $St_C$ = 0.08, (b) $St_C$ = 0.25 and (c) $St_C$ = 0.67. Streamwise locations $x'/C$ are indicated. Theoretical distributions from Moore & Saffman (1973) and Batchelor (1964) are included for reference.

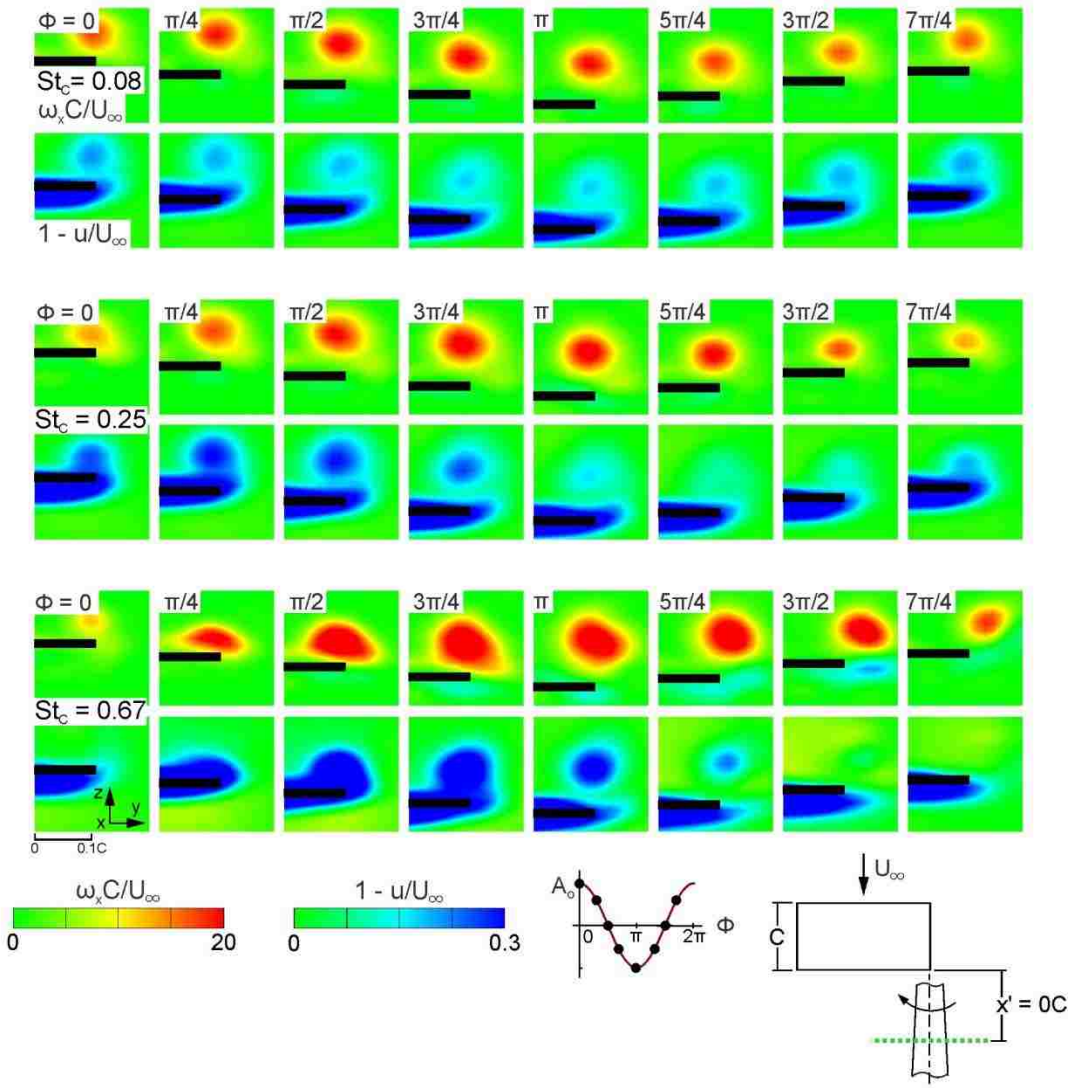


**Figure 4.4:** Cross-sectional slices of axial vorticity $\omega_x C/U_\infty$ and axial velocity deficit $1 - u/U_\infty$ as a function of phase angle $\Phi$ at each Strouhal number $St_C$ at the streamwise location $x'/C = 0$.

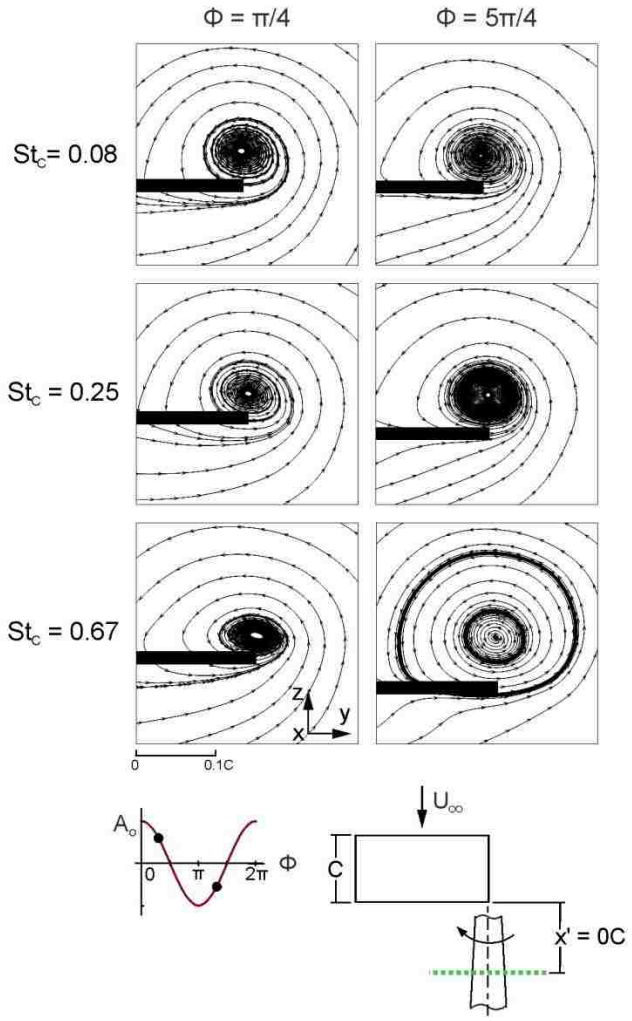


**Figure 4.5:** Streamline patterns at phase angles $\Phi = \pi/4$ and $\Phi = 5\pi/4$ at each Strouhal number $St_C$ at the streamwise location $x'/C = 0$.

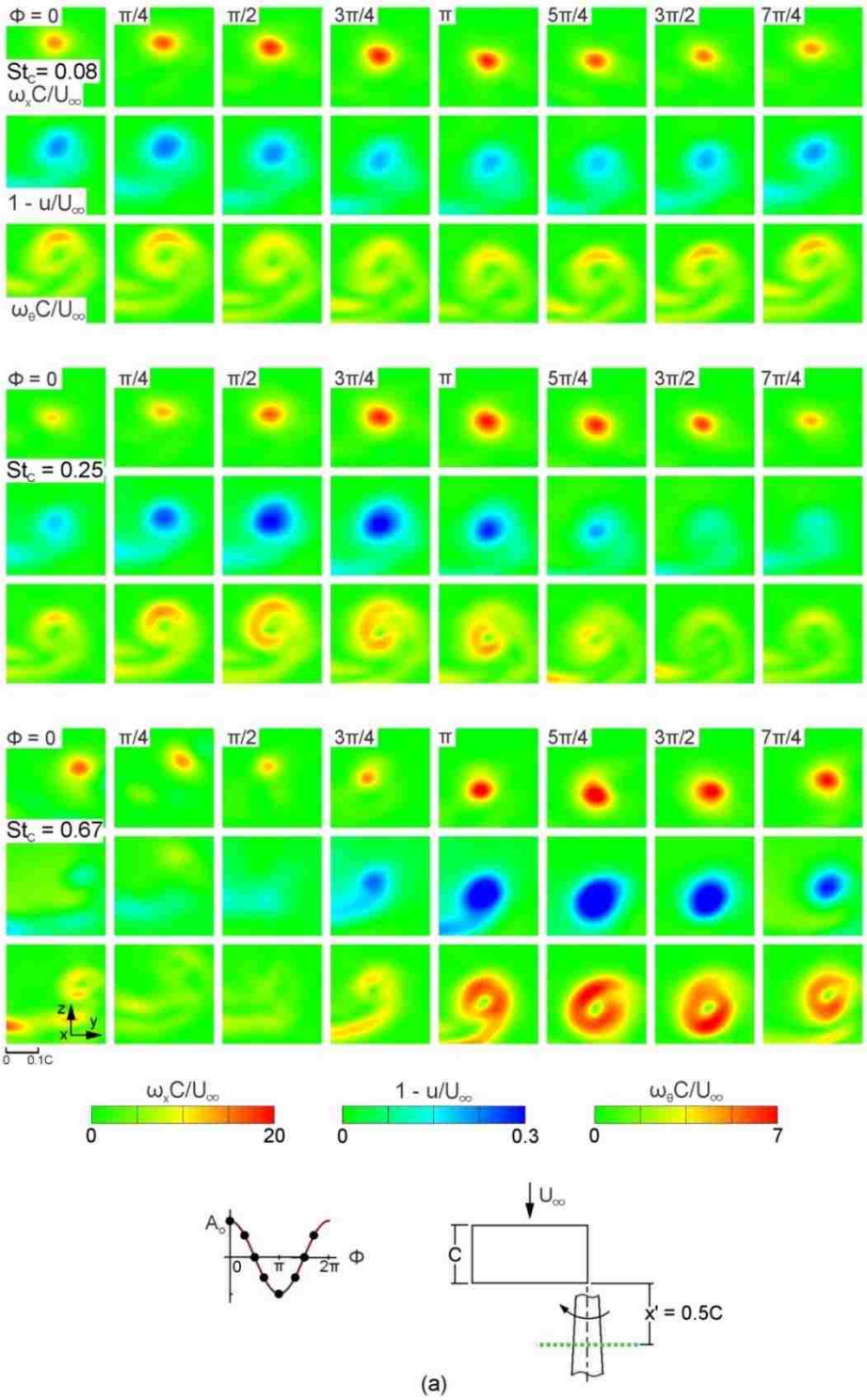


**Figure 4.6:** Cross-sectional slices of axial vorticity $\omega_x C/U_\infty$, axial velocity deficit $1 - u/U_\infty$ and azimuthal vorticity $\omega_\theta C/U_\infty$ as a function of phase angle $\Phi$ at each Strouhal number $St_C$ at the streamwise location (a) $x'/C = 0.5$.

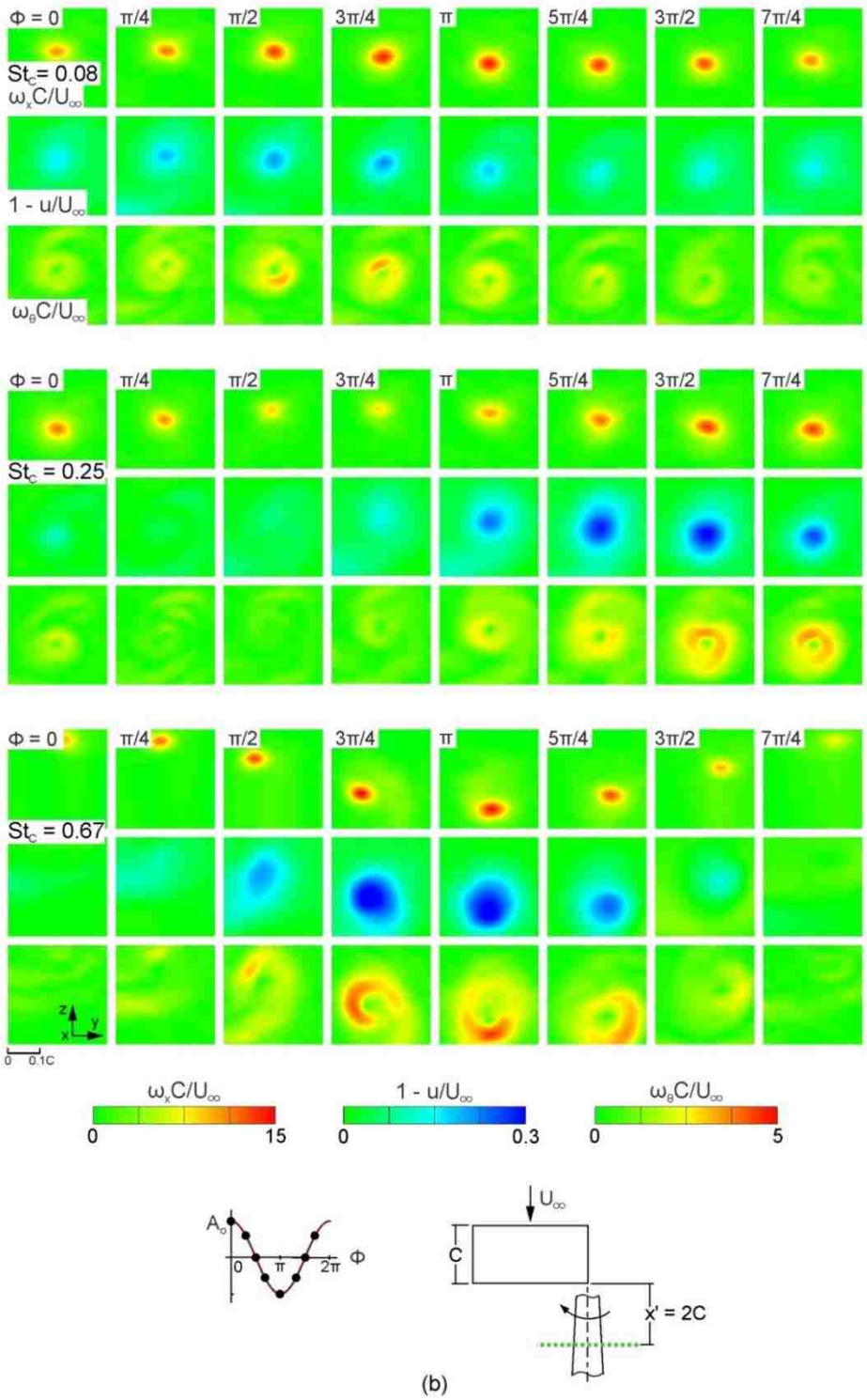


**Figure 4.6:** Cross-sectional slices of axial vorticity $\omega_x C/U_\infty$, axial velocity deficit $1 - u/U_\infty$ and azimuthal vorticity $\omega_\theta C/U_\infty$ as a function of phase angle $\Phi$ at each Strouhal number $St_C$ at the streamwise location (b) $x'/C = 2$.

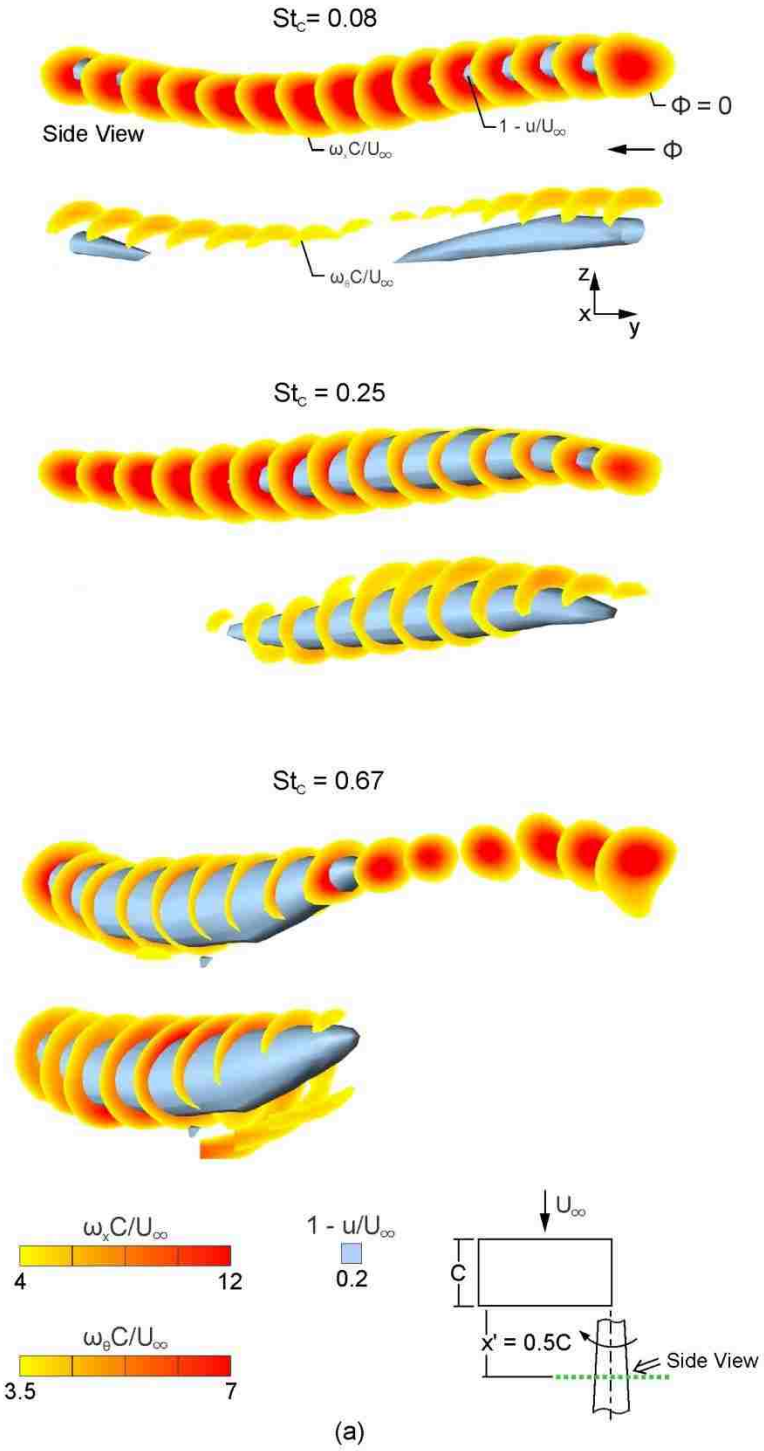


**Figure 4.7:** Temporal volumes of cross-sectional slices of axial vorticity $\omega_x C/U_\infty$ (above) and azimuthal vorticity $\omega_\theta C/U_\infty$ (below) superposed on iso-surfaces of axial velocity deficit $1 - u/U_\infty$ at each Strouhal number $St_C$ at the streamwise location (a) $x'/C$ = 0.5.

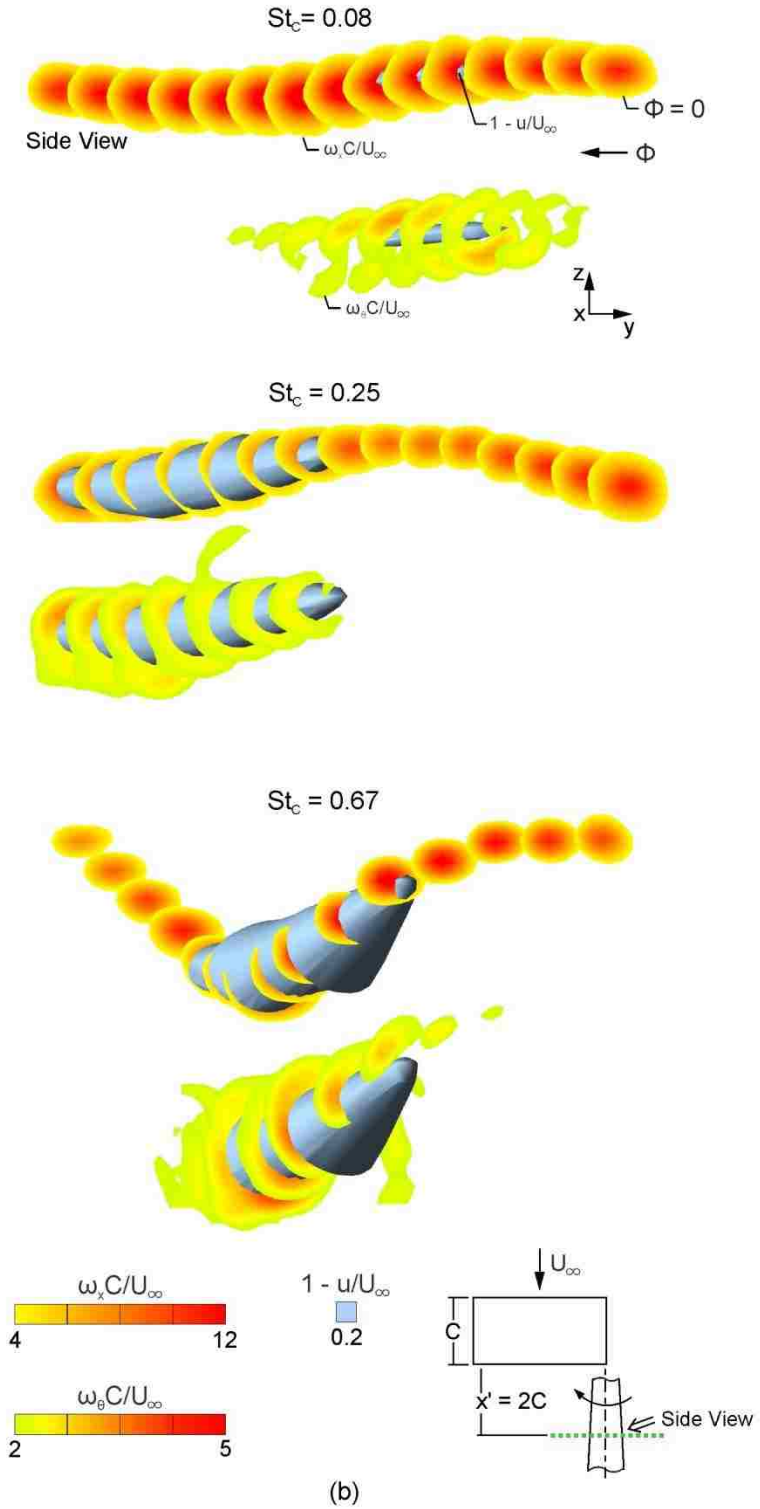


**Figure 4.7:** Temporal volumes of cross-sectional slices of axial vorticity $\omega_x C/U_\infty$ (above) and azimuthal vorticity $\omega_\theta C/U_\infty$ (below) superposed on iso-surfaces of axial velocity deficit $1 - u/U_\infty$ at each Strouhal number $St_C$ at the streamwise location (b) $x'/C = 2$.

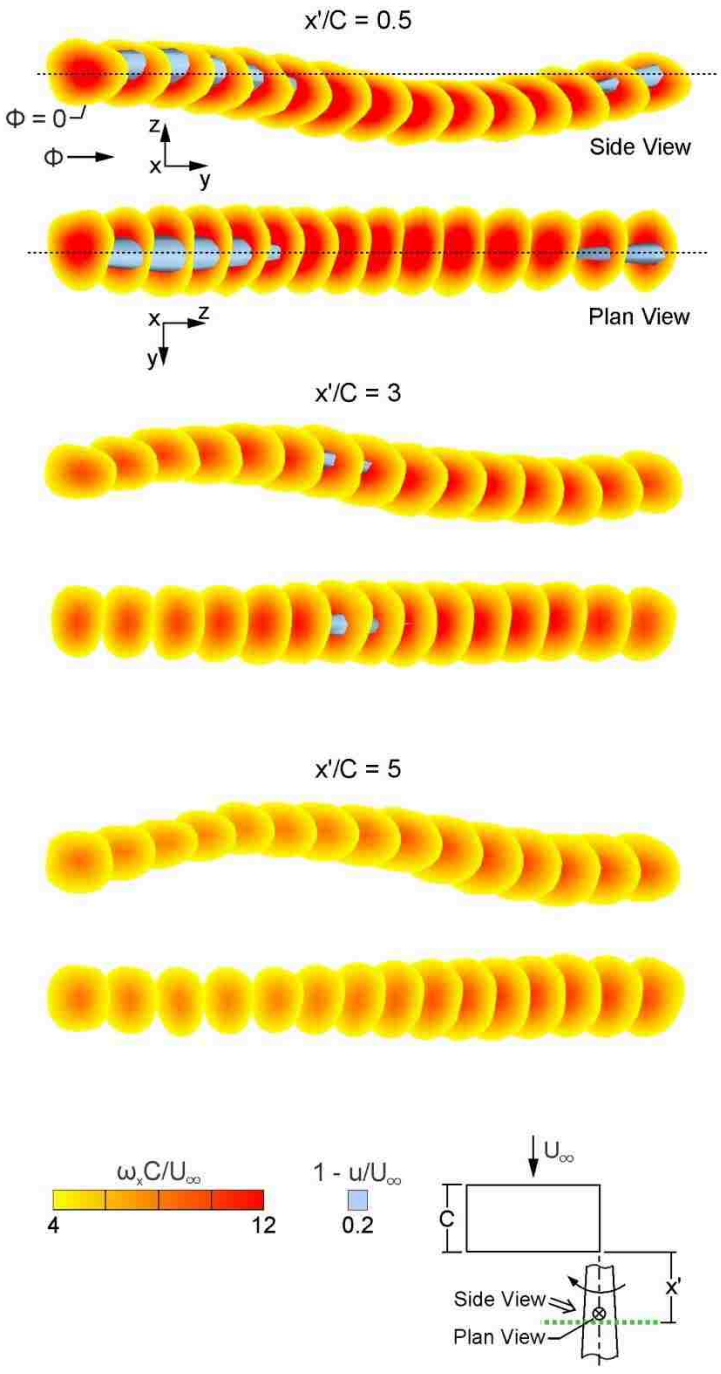


**Figure 4.8:** Temporal volumes of cross-sectional slices of axial vorticity $\omega_x C/U_\infty$ superposed on iso-surfaces of axial velocity deficit $1 - u/U_\infty$ at streamwise distances $x'/C$ = 0.5, 3 and 5. Strouhal number is $St_C$ = 0.08.

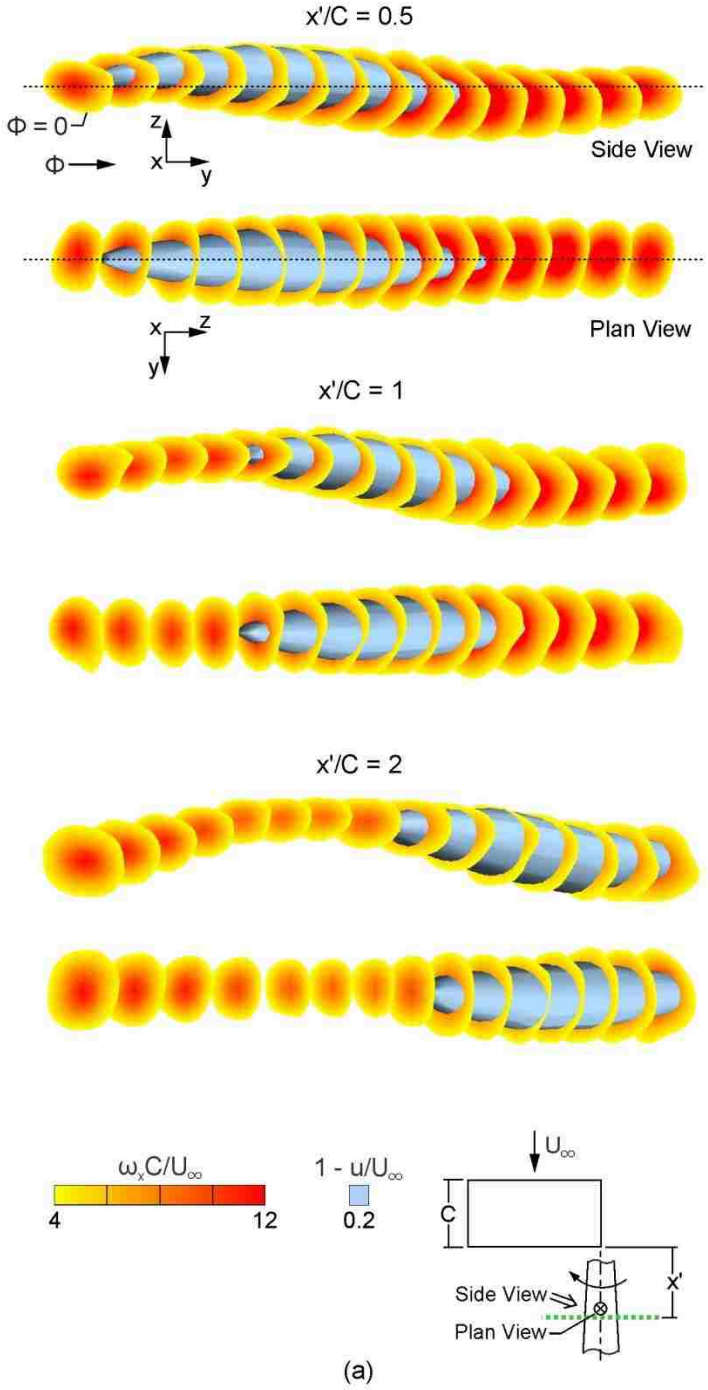


**Figure 4.9:** Temporal volumes of cross-sectional slices of axial vorticity $\omega_x C/U_\infty$ superposed on iso-surfaces of axial velocity deficit $1 - u/U_\infty$ at streamwise distances (a) $x'/C$ = 0.5, 1 and 2. Strouhal number is $St_C$ = 0.25.

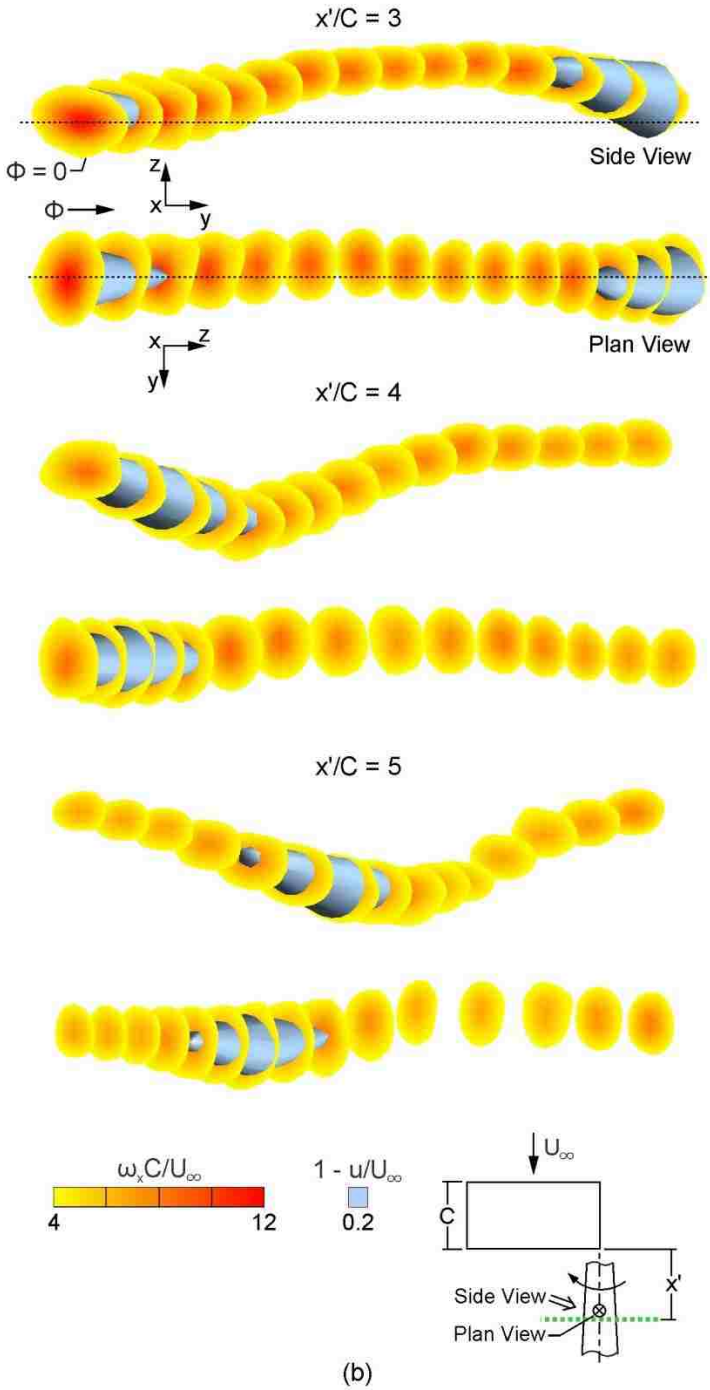


**Figure 4.9:** Temporal volumes of cross-sectional slices of axial vorticity $\omega_x C/U_\infty$ superposed on iso-surfaces of axial velocity deficit $1 - u/U_\infty$ at streamwise distances (b) $x'/C$ = 3, 4 and 5. Strouhal number is $St_C$ = 0.25.

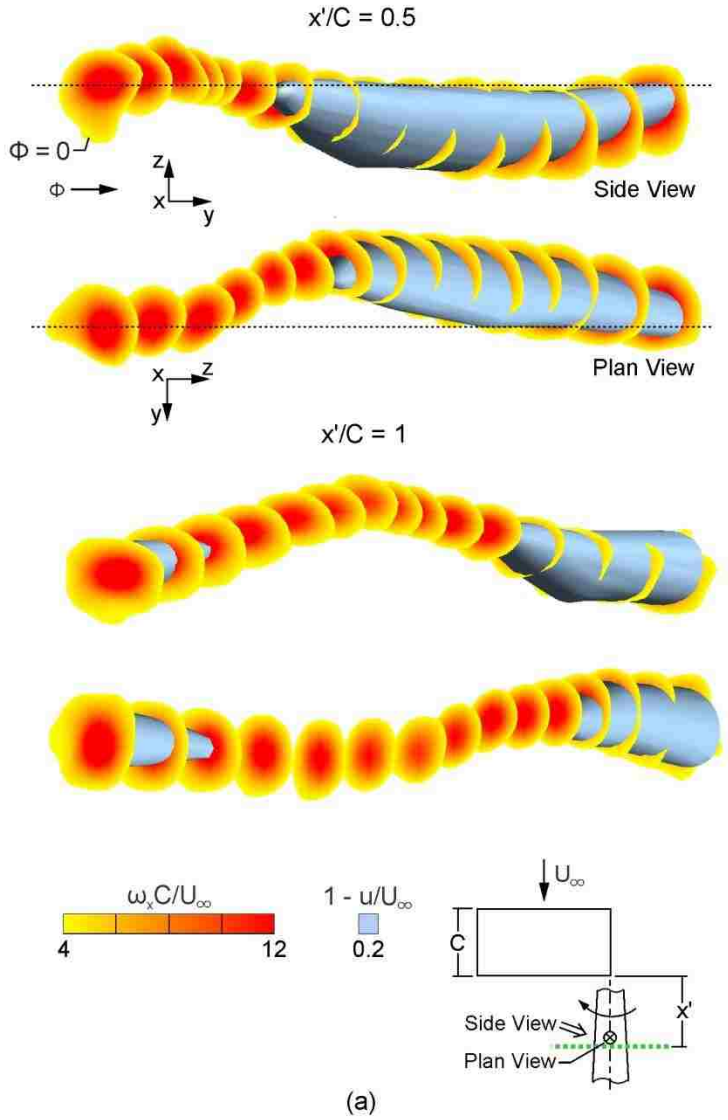


**Figure 4.10:** Temporal volumes of cross-sectional slices of axial vorticity $\omega_x C/U_\infty$ superposed on iso-surfaces of axial velocity deficit $1 - u/U_\infty$ at streamwise distances (a) $x'/C$ = 0.5 and 1. Strouhal number is $St_C$ = 0.67.

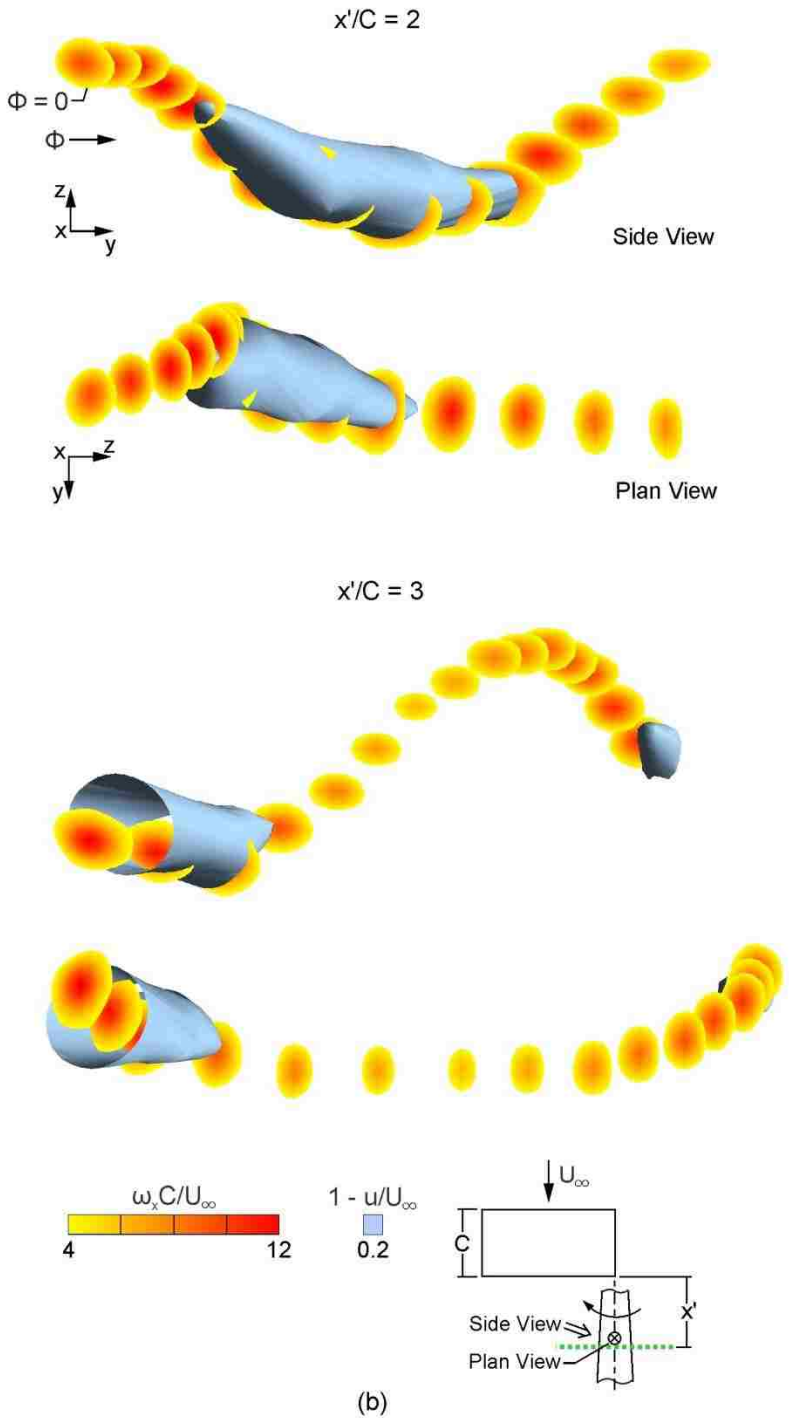


**Figure 4.10:** Temporal volumes of cross-sectional slices of axial vorticity $\omega_x C/U_\infty$ superposed on iso-surfaces of axial velocity deficit $1 - u/U_\infty$ at streamwise distances (b) $x'/C$ = 2 and 3. Strouhal number is $St_C$ = 0.67.

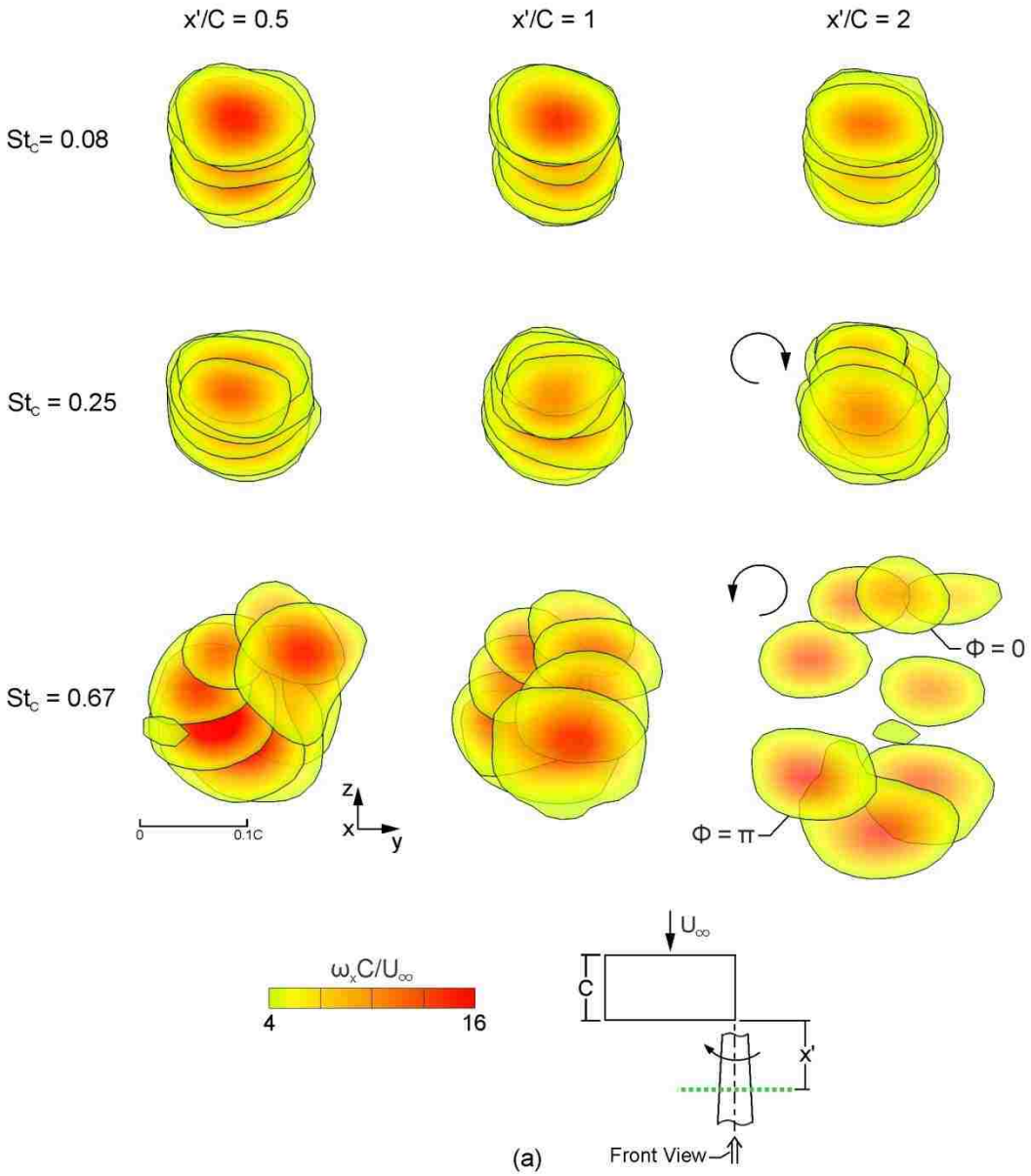


**Figure 4.11:** Time-sequence of cross-sectional slices of axial vorticity $\omega_x C/U_\infty$ viewed in the upstream direction at each Strouhal number $St_C$ at streamwise distances (a) $x'/C$ = 0.5, 1 and 2.

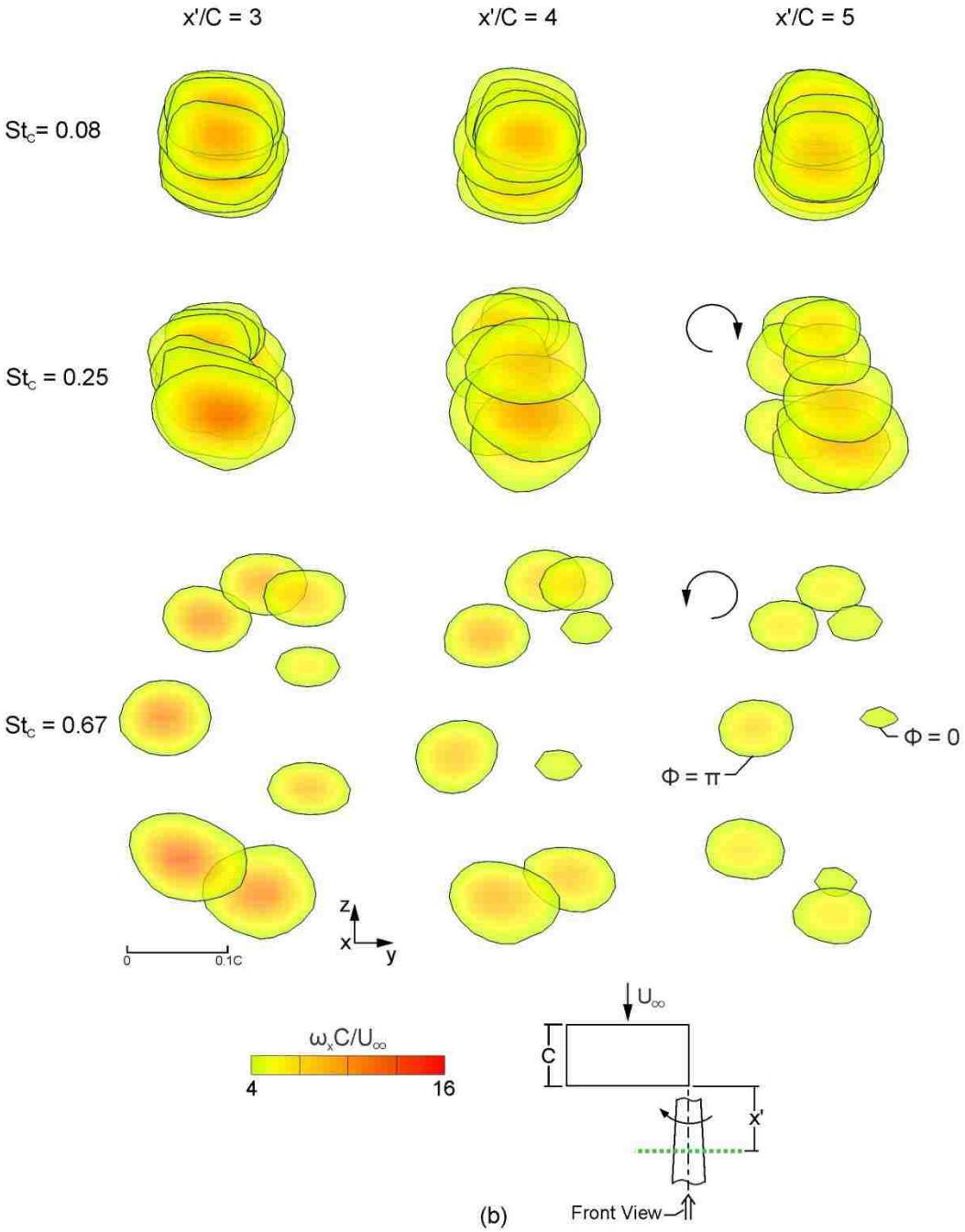


**Figure 4.11:** Time-sequence of cross-sectional slices of axial vorticity $\omega_x C/U_\infty$ viewed in the upstream direction at each Strouhal number $St_C$ at streamwise distances (b) $x'/C$ = 3, 4 and 5.

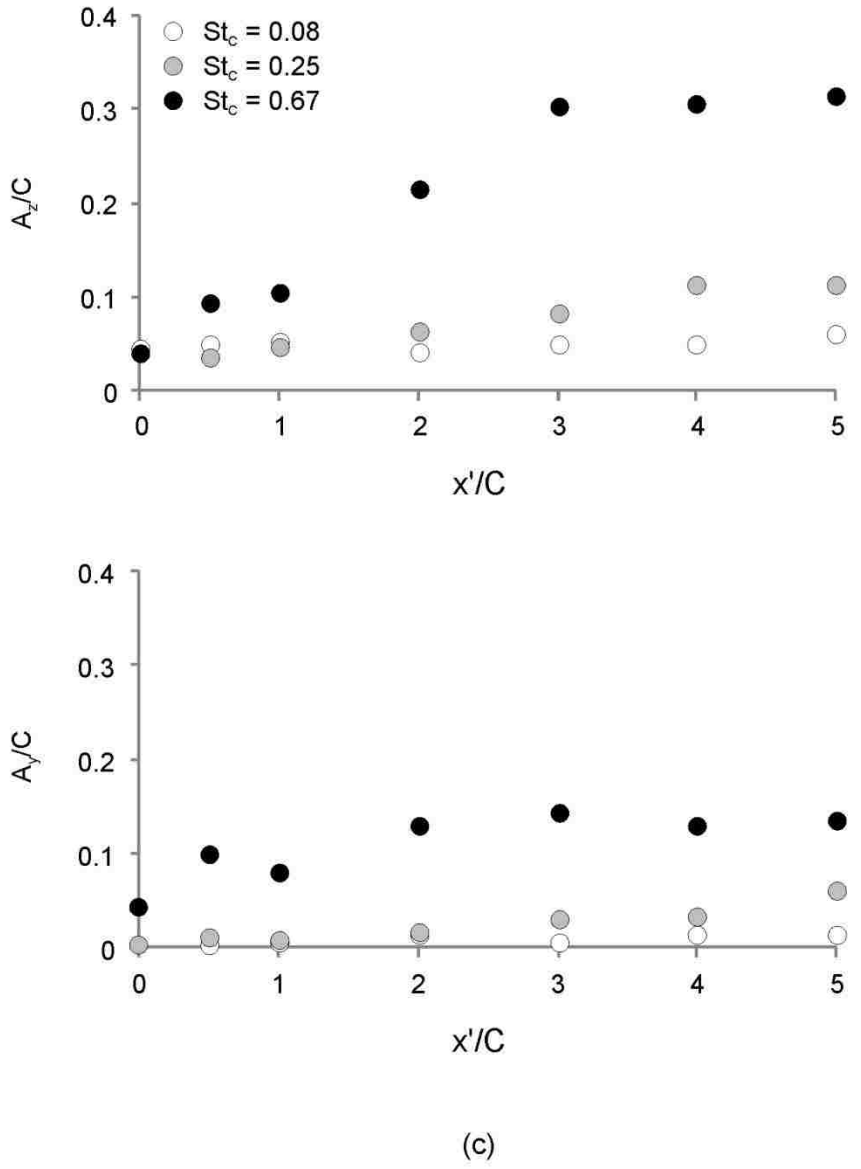


(c)

**Figure 4.11:** Vortex trajectory. (c) Plots of vertical $A_z/C$ and lateral $A_y/C$ amplitude of the vortex motion for three Strouhal numbers $St_C$ as a function of streamwise distance $x'/C$.

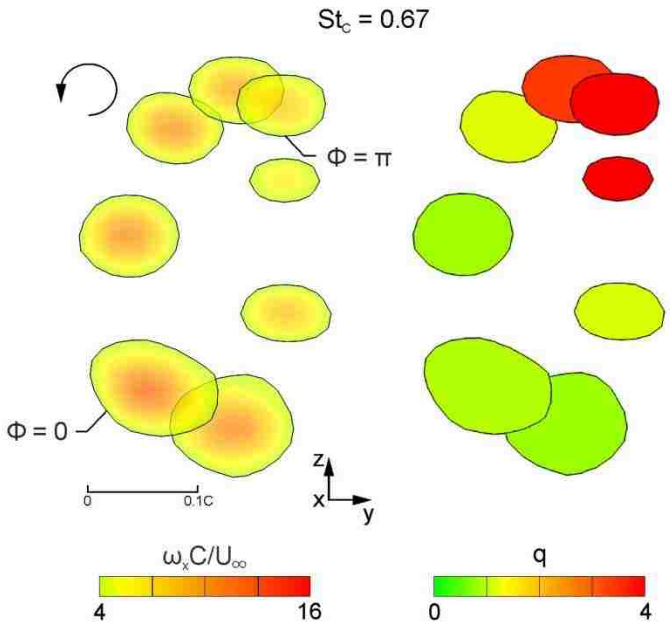


**Figure 4.12:** Time-sequence of cross-sectional slices of axial vorticity $\omega_x C/U_\infty$ (left) and swirl ratio $q$ (right) viewed in the upstream direction at Strouhal number $St_C = 0.67$ at the streamwise location $x'/C = 3$.

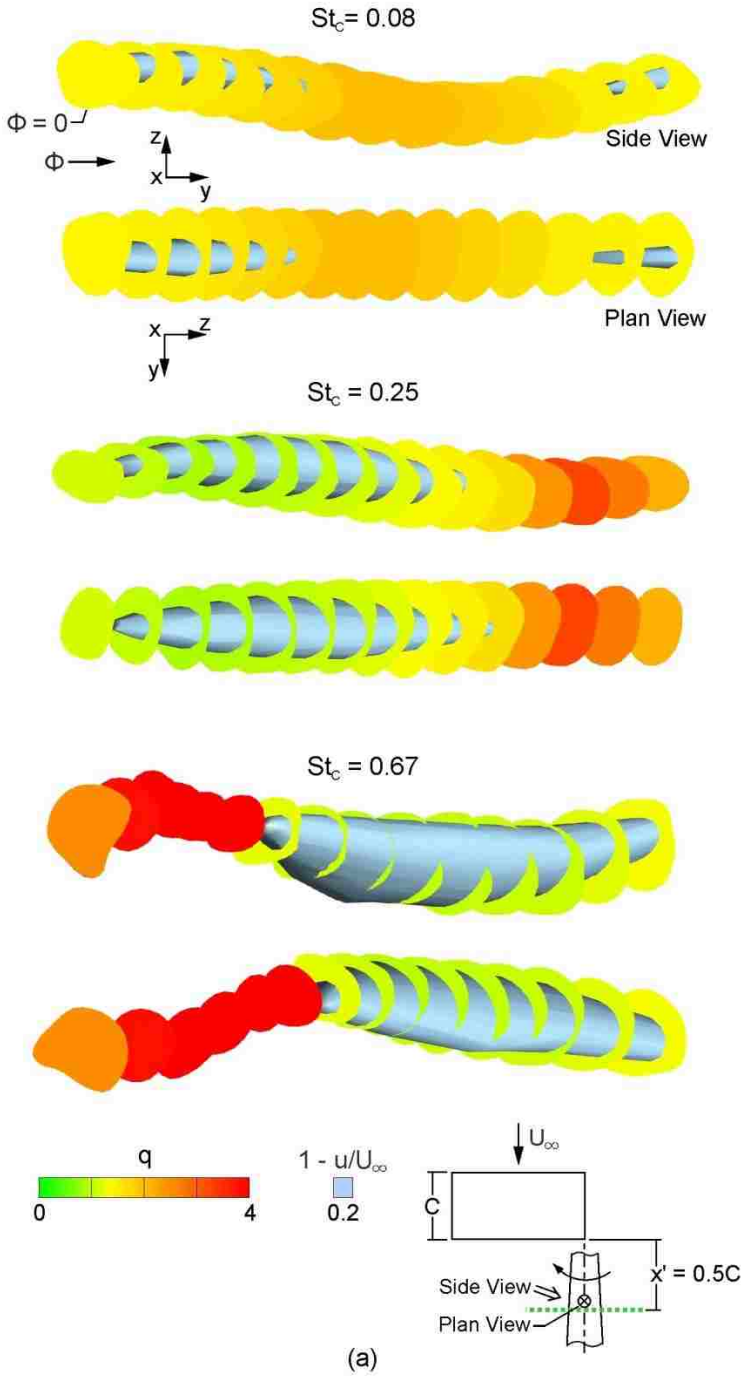


**Figure 4.13:** Cross-sectional slices of axial vorticity $\omega_x C/U_\infty$ colored according to magnitude of swirl ratio $q$ superposed on iso-surfaces of (blue) axial velocity deficit $1 - u/U_\infty$ at each Strouhal number $St_C$ at a streamwise distance (a) $x'/C = 0.5$.

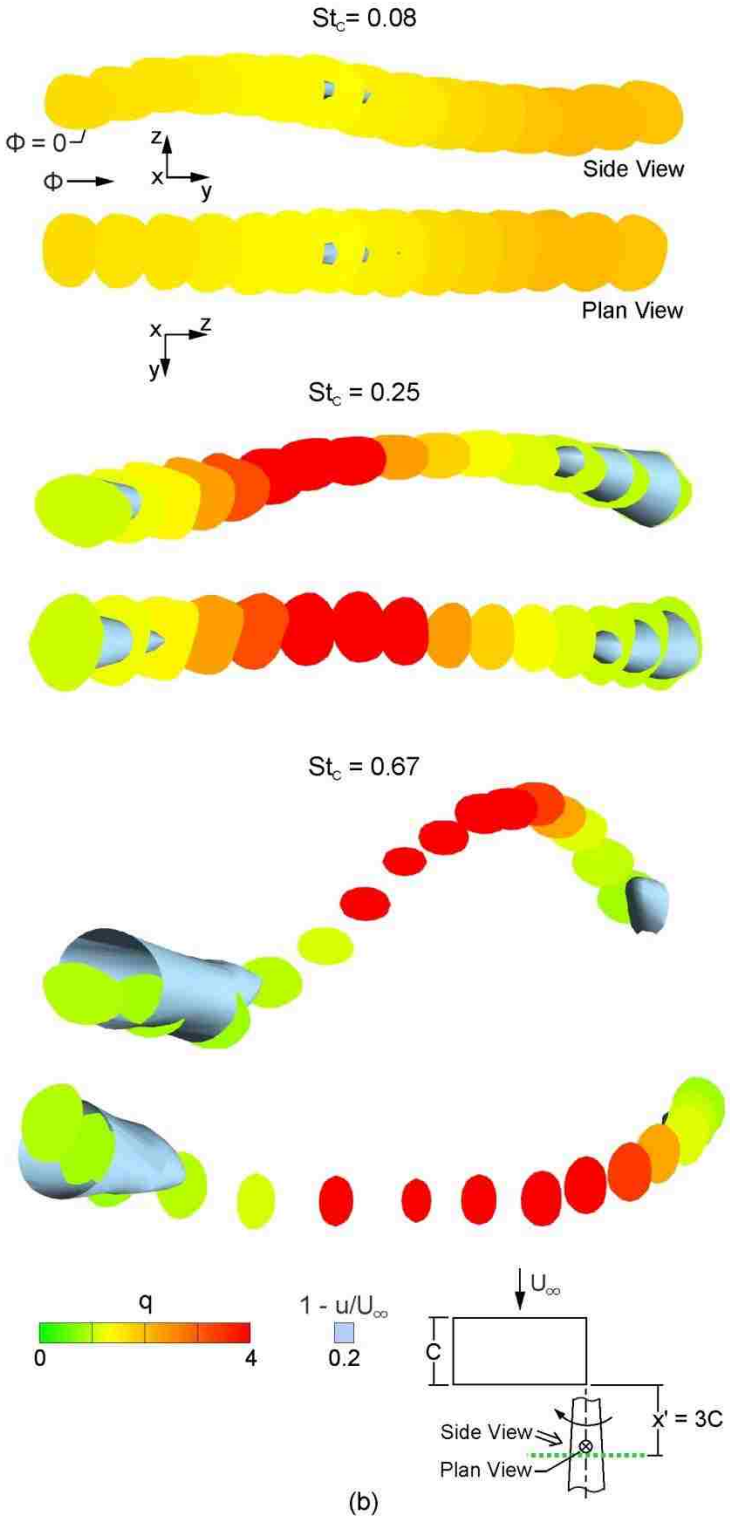


**Figure 4.13:** Cross-sectional slices of axial vorticity $\omega_x C/U_\infty$ colored according to magnitude of swirl ratio $q$ superposed on iso-surfaces of (blue) axial velocity deficit $1 - u/U_\infty$ at each Strouhal number $St_C$ at a streamwise distance (b) $x'/C = 3$.

# CHAPTER 5

# INTERACTION OF A PERTURBED TRAILING VORTEX WITH A FLAT PLATE

## 5.1 INTRODUCTION

### *5.1.1 Objectives*

In recent years, valuable insight has been gained into the structure of a trailing vortex and its interaction with a downstream (follower) plate, or wing. However, a number of issues remain unresolved, including the influence of unsteady motion of the incident vortex on the vortex-wing interaction. The focus of this chapter is to examine the unsteady flow structure along a follower wing arising from a perturbed incident vortex. The nature of the flow topology for two impingement locations will be analyzed with respect to the steady vortex-wing interaction. These concepts are addressed via volumetric and cross-sectional representations of the vortex structure acquired from particle-image velocimetry (PIV) in conjunction with three-dimensional reconstruction techniques.

### *5.1.2 Overview*

For both steady and unsteady vortex-wing interactions, the spanwise impingement location of the incident vortex determines the dominant mode of the interaction. Introducing unsteadiness of the incident vortex, in the form of vertical displacement perturbations, gives rise to orbital motion of the incident vortex, thereby yielding a time-dependent structure of the vortex-wing interaction, in contrast to the time-invariant modes of steady vortex-wing interaction. For the case of an aligned interaction, where the incident vortex having an orbital trajectory is nominally centered on the tip of the wing, the upwash of the incident vortex gives rise to separation at the tip of the wing and the induction of a tip vortex of opposite sign. This results in formation of a dipole comprising the induced and the incident vortices. In contrast to the vortex dipole arising from interaction of an incident steady vortex with the wing, the dipole structure rotates around the tip of the wing in an ordered manner. Variations of the upwash of the incident vortex alter the strength of the induced vortex. On the other hand, when the incident vortex impinges inboard of the tip of the wing, it induces a vortex having vorticity of the same sign at the wingtip due to the downwash of the incident vortex, which causes separation at the tip. At the leading edge of the wing the incident vortex bifurcates and an induced vortex at the tip of the wing is evident. Moreover, vorticity of opposite sign, relative to that of the incident vortex, is evident across the wing surface during this bifurcation and when it is positioned above the wing. This occurs as a result of the eruption of the boundary layer along the wing due to the presence of the incident vortex.

## 5.2 EXPERIMENTAL SYSTEMS AND TECHNIQUES

Experiments were performed in a large-scale, recirculating water channel in the fluids laboratory at Lehigh University. The main test section of the facility is 594 mm in depth and 613 mm in width. Further description on the flow facilities is presented in Chapter 2. In the present experiments, the freestream velocity was maintained at $U_\infty$ = 152.4 mm $s^{-1}$ which yields a chord based Reynolds number $Re_C = U_\infty C/\nu$ = 15200, where C is the chord of the wing and ν is the kinematic viscosity of water.

Monoscopic particle image velocimetry was employed to determine the flow structure of a perturbed vortex impinging along a follower wing. A schematic of this system is given in Figure 5.1a. A laser sheet oriented in the spanwise, or lateral, direction, in conjunction with charged coupled device (CCD) cameras and a mirror, are used to capture the velocity field at successive crossflow planes along the follower wing. Further details on the PIV system is indicated in Chapter 2.

A schematic of the wing oscillation mechanism is indicated in Figure 5.1b. It employs a computer-controlled motor that drives a scotch-yoke mechanism that is attached to the vertically-oriented sting of the wing. The sting is affixed to the center of the wing and also fastened to a sliding bar coupled to a vertically-oriented traverse. A connecting rod is used to link the sliding bar to a wheel that is attached to the motor. This mechanism converts the linear motion to rotational motion. An encoder attached to the motor is used to determine the position of the wing.

Figure 5.1c is a rendered model of the test section that includes the PIV system, the wing perturbation mechanism and the wing positioning system. The laser head is positioned underneath the channel and the laser sheet is oriented in the spanwise direction. The mirror is positioned downstream of the laser sheet. Analysis of the upstream influence of the mirror on the flow structure is given in Appendix A. The wing positioning system consists of several motors with encoders that allow for precise positioning of the wing in all three directions. This system also provides controlled perturbation of the wing. In order to capture images at successive planes in the streamwise direction, the motion control system is translated along a rail system that extends the length of the channel.

Figure 5.2a shows plan and side view schematics of the experimental system. The model of the leader wing is a rectangular flat plate of aspect ratio $AR$ = 2, with a chord $C$ = 102 mm and span $b$ = 203 mm. The thickness of the wing $t$ = 1.6 mm and the corner radius $r_c$ = 0.5mm. The wing is fixed at an angle of attack $\alpha_o$ = 6° and is subjected to continuous heaving motion in the vertical direction as indicated in the side view schematic. The follower wing is a rectangular flat plate of $AR = 4$ with a chord $C_{fw}$ = 51 mm and span $b$ = 203 mm. The thickness of the wing $t$ = 1.6 mm and the corner radius $r_C$ = 0.5mm. The wing is fixed at an angle of attack $\beta_o$ = 0°. Separation distances $\Delta x/C_{fw}$ and $\Delta y/C_{fw}$ are also given in the figure. The streamwise separation distance between the two wings is given as $\Delta x/C_{fw}$ = 4. Two spanwise separation distances were employed $\Delta y/C_{fw}$ = 0 (aligned) and $\Delta y/C_{fw}$ = 0.25 (inboard).

Figure 5.2b depicts the sinusoidal displacement amplitude $A(\Phi)$ of the wing as a function of phase angle $\Phi$. The oscillation cycle consists of the downstroke of the wing which occurs between $\Phi = 0$ to $\Phi = \pi$ and the upstroke between $\Phi = \pi$ to $\Phi = 2\pi$. The non-dimensional Strouhal number of the perturbation, indicated in Figure 4.2b, is $St_C = fC/U_\infty = 0.67$. This value of Strouhal number corresponds respectively to a value of wavelength $\lambda/C = U_\infty/fC = 1.5$ or $\lambda/d_o = 15$ where $d_o$ is the diameter of the vortex from a stationary wing. The vortex diameter $d_o$ is defined as twice the vortex radius $r_o$, where $r_o$ is the circumferentially averaged radial location of the maximum value of swirl velocity $(u_\theta)_{max}$. The displacement amplitude of the wing motion is $A_o/C = 0.01$ or $A_o/d_o = 0.1$.

The water is seeded with 11 μm metallic coated hollow plastic spheres which have a density of 1.958 g/cm$^3$. A dual pulsed Nd:YAG laser system is utilized to generate a laser sheet of 1.5 mm thickness which illuminates the particles. A CCD camera is used to capture the particle images contains an array of 1600 pixels × 1192 pixels. Insight 4G was employed to process the particle images. Interrogation windows of 32 pixels × 32 pixels are used and contain 15-20 particle images. A 50% overlap between camera frames is utilized and the particle images are processed using a frame-to-frame cross-correlation technique. Information on the error analysis of the PIV system can be found in Chapter 2.

Images were acquired upstream and along the follower wing at streamwise locations $x'/C_{fw} = -0.25$, 0, 0.25, 0.5, 0.75 and 1; these values correspond to the distance away from of the leading edge of the wing, where $x'/C_{fw} = 0$ is the leading edge. A phase-referencing technique was employed, which grouped together images taken at a given vertical position of the wing; this process provided phase-averaged images. Volumetric

reconstruction was performed utilizing in-house software in conjunction with the phase-averaged images.

## 5.3 AXIAL VORTICITY OF INCIDENT VORTEX UPSTREAM OF WING

Figure 5.3 shows a time sequence of sectional slices of axial vorticity $\omega_x C/U_\infty$ at a location upstream of the leading edge of the wing, $x'/C_{fw}$ = - 0.25. In the first row of images, the view is looking upstream whereby the sectional slices of axial vorticity at successive instants of time are superimposed on one another These images correspond to extreme values of offset of the incident vortex relative to the tip of the wing, i.e., aligned $\Delta y/C_{fw} = 0$ and inboard $\Delta y/C_{fw}$ = 0.25 interactions. At both values of offset, the motion of the incident vortex is similar; it has a consistent orbital form. This orbital motion is present in absence of the follower as shown in Fishman & Rockwell (2018). The second row of images of Figure 5.3 corresponds to trimetric views. This orientation of the direction of view clearly shows variations of cross-sectional area and peak axial vorticity of the incident vortex are evident during the oscillation cycle.

## 5.4 ALIGNED INTERACTION

### *5.4.1 Overview of Flow Structure Along Flat Wing*

Figure 5.4 shows an overview of the flow structure for the aligned interaction $\Delta y/C_{fw}$ = 0 in the form of volumetrically reconstructed images. Iso-surfaces (yellow and

light brown) of axial vorticity $\omega_x C/U_\infty$ are shown with overlays of cross-sectional slices of red-yellow (positive) and blue (negative) axial vorticity. The upper and lower images correspond respectively to phase angles $\Phi = \pi/4$ and $\Phi = 5\pi/4$ of the wing motion that represent the extreme vertical impingement locations of the incident vortex. At $\Phi = \pi/4$, the vortex impinges directly onto the wing tip. The upward deflection of the vortex along the wing is associated with its vertical undulation that arises from the vertical component of the orbital motion of the incident vortex. In conjunction with the upward deflection along the wing tip, an opposite signed (blue) vortex is induced. The cross-sectional slices indicate the formation of a dipole involving the incident (red-yellow) vortex and the induced (blue) vortex whose position fluctuates about the wingtip. This dipole structure is substantially attenuated along the wingtip at $\Phi = 5\pi/4$. At this phase of the oscillation cycle, at a location immediately upstream of the leading edge of the wing, the position of the incident vortex is above the wing. However, from the midchord to the wake, it is positioned below the wing. Again, this is due to the vertical component of the orbital motion of the incident vortex. In essence, for this case where the incident vortex approaching the wing is aligned with its tip, the undulation of the vertical position of the vortex induces an opposite-signed vortex along the wing tip and forms a dipole with the incident vortex. The position of the dipole varies with respect to the position of the incident vortex.

### *5.4.2 Cross-Sectional Patterns of Axial Vorticity and Streamline Topology*

Figure 5.5 shows sectional slices of axial vorticity $\omega_x C/U_\infty$ at the midchord of the wing $x'/C_{fw} = 0.5$ for the aligned interaction $\Delta y/C_{fw} = 0$. The sequence of images

corresponds to variations of phase angle $\Phi$. At $\Phi = 0$, the incident vortex (red) is positioned above and slightly outboard of the wing tip. An induced (blue) vortex of negative vorticity is also evident. As the incident vortex moves downward around the tip, from $\Phi = \pi/4$ to $\Phi = \pi$, the induced vortex position varies similarly. Clearly, the orientation of the dipole is a function of the position of the incident vortex as it is responsible for inducing a negative vorticity concentration at the wingtip. At $\Phi = 5\pi/4$, the incident vortex structure bifurcates as it moves upward over the wingtip. At $\Phi = 3\pi/2$, the incident vortex is positioned above the wing.

It is known that the positioning of a vortex incident upon a wing affects the strength of the induced vortex. For example, in the case of a steady incident vortex, its position, relative to the tip of the wing, governs the peak axial vorticity of the induced vortex as demonstrated in McKenna (2017). Based on these investigations, it is expected that peak axial vorticity would occur when the incident vortex is positioned slightly above the wing, similar to that at $\Phi = 0$. However, in the present study, the peak axial vorticity of the incident vortex varies with $\Phi$ corresponding to variation of position of the incident vortex during its orbital cycle. This is evident when comparing images at $\Phi = 0$ and $\Phi = 7\pi/4$, where the position of the incident vortex is similar, but the values of peak axial vorticity are not. In essence, this shows that both the positioning and the peak axial vorticity of the incident vortex determine the strength of the induced vortex.

Figure 5.6a shows streamline topology overlaying sectional slices of axial vorticity $\omega_x C/U_\infty$ at the midchord of the wing $x'/C_{fw} = 0.5$ for the aligned interaction $\Delta y/C_{fw} = 0$. Images are shown as function of phase angle $\Phi$. Selected critical points are

labeled on each image. At $\Phi = 0$, a larger image of this is provided in Figure 5.6b, the incident vortex is positioned above the wing and a focus F1 is evident at its center. The streamlines beneath the wing tip are oriented in the outboard direction and wrap around the tip of the wing such that above the wing tip they are oriented in the inboard direction. This pattern of streamline topology is associated with negative (blue) axial vorticity at the tip of the wing. In Figure 5.6a, at $\Phi = \pi/2$, the incident vortex, focus F1, moves in the downward direction below the tip of the wing, and a focus F3 is evident. This focus is associated with the negative vorticity concentration of the induced vortex that develops at the wing tip. A small region of positive vorticity is associated with another focus F2 which arises from distortion of the vortex at the leading edge. Compatibility between all of the foregoing features of the streamline topology is allowed by the saddle point S1. All of the critical points F1, F2, F3 and S1 are preserved at $\Phi = \pi$, despite change of the position of the incident vortex which is further beneath the wing tip. The orientation of the dipole that comprises the incident and induced vortices changes significantly from $\Phi = \pi$ to $\Phi = 3\pi/2$. At $\Phi = 3\pi/2$, the incident vortex is again positioned above the wing and focus F1 is evident. The induced vortex is attenuated and confined to the top surface of the wing; this region of vorticity has no focus associated with it. A saddle point S1 allows for compatibility between focus F1 above and the focus F2 below the wing. Again, the streamlines below the wing wrap around the tip of the wing.

Figure 5.6c shows streamline topology (top), line contours of upwash velocity $w/U_\infty$ (middle) and line contours of spanwise velocity $v/U_\infty$ (bottom) overlaying axial vorticity $\omega_x C/U_\infty$. The image is taken at $\Phi = 0$ at a streamwise location $x'/C_{fw} = 0.5$. Solid

lines correspond to positive velocity and dashed lines correspond to negative velocity. The primary mechanism of axial vorticity generation at the tip of the wing is due to the upwash of the incident vorticity causing separation to occur, indicated by the streamline pattern. Additionally, the inboard directed spanwise velocity drives the flow around the tip of the wing during this process.

Figure 5.7 provides streamline patterns superposed on sectional slices of axial vorticity $\omega_x C/U_\infty$ for the aligned interaction $\Delta y/C_{fw} = 0$. Images are shown as a function of streamwise distance $x'/C_{fw}$ for phase angles $\Phi = \pi/2$ and $\Phi = 3\pi/2$. These phase angles correspond respectively to movement of the incident vortex in the upward and downward directions around the wing tip. At $\Phi = \pi/2$ (left column) and $x'/C_{fw} = 0.25$, the incident vortex is positioned below the wing and a focus F1 is evident. As previously indicated, the flow below the wing wraps around the tip and separation occurs. Reattachment is evident further inboard of the tip. This process is associated with generation of negative vorticity at the wing tip. At $x'/C_{fw} = 0.5$, as the incident vortex and focus F1 move upwards, the formation of the induced vortex and a focus F3 is apparent. A small region of positive vorticity is associated with another focus F2, which is a remnant of the incident vortex inboard of the wingtip at $x'/C_{fw} = 0.25$. Compatibility between these features is allowed by the saddle point S1. The flow topology at the streamwise location $x'/C_{fw} = 0.5$ is preserved at the streamwise locations $x'/C_{fw} = 0.75$ and $x'/C_{fw} = 1$ for this value of phase $\Phi = \pi/2$. At the phase angle $\Phi = 3\pi/2$ (right column), a focus F1 is evident at the center of the incident vortex at $x'/C_{fw} = 0.25$. As the incident vortex moves below the tip of wing, at $x'/C_{fw} = 0.5$ and $x'/C_{fw} = 0.75$, a secondary focus F2 is evident with a

saddle point S1 between them. This topology is associated with the bifurcation of the incident vortex. Finally, at $x'/C_{fw} = 1$, the incident vortex is entirely below the wing such that only focus F1 is present. In general, there is distinct asymmetry in the flow topology with increasing streamwise distance when the incident vortex moves upward around the wing tip at $\Phi = \pi/2$ in comparison with its movement downward around the wing tip at $\Phi = 3\pi/2$.

Figure 5.8 shows volumetrically reconstructed images of sectional slices of axial vorticity $\omega_x C/U_\infty$ for the aligned interaction $\Delta y/C_{fw} = 0$. A trimetric orientation is provided in conjunction with an inlay of a plan view orientation. The wing is semi-transparent such that structures on both sides are visible. At $\Phi = 0$, the incident vortex is positioned slightly above and outboard of the wingtip at the leading edge. It forms a dipole with the induced vortex along wing tip. For all streamwise distances, the orientation of the dipole is directly related to the position of the incident vortex. This results in a dipole whose position and orientation vary in a periodic manner around the tip of the wing. From $\Phi = 0$ to $\Phi = 3\pi/4$ the dipole rotates counter-clockwise around the tip and conversely, from $\Phi = \pi$ to $\Phi = 7\pi/4$, it rotates clockwise around the tip. Moreover, the peak axial vorticity levels of the incident vortex are directly related to the peak vorticity levels of the induced vortex. That is, attenuated levels of axial vorticity in the incident vortex induce a weaker vortex at the tip of the wing and vice versa. Viewing the images of Figure 5.8 as a whole, it is possible to summarize the following observations: (i) formation of a dipole involving an incident and an induced vortex does not occur along the leading portion of the tip of the wing, that is for a distance of approximately an

eighth chord from the leading edge of the wing; (ii) contrary to the anticipated physics, the largest magnitude axial vorticity of the induced vortex does not occur during upward motion of the incident vortex about the tip of the wing, rather it occurs during downward motion about the tip, as a result of the fluctuating peak axial vorticity of the incident vortex; (iii) comparison of patterns of the incident and induced vortices at values of phase angle Φ having a difference of π does not show mirror images of the overall vortex system along the tip of the wing; (iv) during part of the oscillation cycle only very small scale, low-level induced vortices are generated due to breaking of the continuous vortex structure along the tip of the wing, that is, the incident vortex is initially above the wing in the leading region, is abruptly bifurcated at mid-chord then exists below the wing in the trailing region of the tip, as seen at $\Phi = 3\pi/2$ and $\Phi = 3\pi/2$. During this process, the magnitude of the streamwise vorticity of the incident vortex is substantially attenuated.

## 5.5 INBOARD INTERACTION

### *5.5.1 Overview of Flow Structure Along Wing*

Figure 5.9 shows an overview of the flow structure for the inboard interaction $\Delta y/C_{fw} = 0.25$. Sectional (red-yellow) slices of axial vorticity are superposed on (yellow-brown) iso-surfaces of axial vorticity $\omega_x C/U_\infty$. Phase angles $\Phi = \pi/4$ and $\Phi = 5\pi/4$ are shown. At $\Phi = \pi/4$, and at a location immediately upstream of the leading-edge of the wing, the vortex is positioned such that it impinges directly onto the leading edge. At the trailing edge, the incident vortex is positioned above the wing and negative vorticity is

evident along the top surface of the wing. At $\Phi = 5\pi/4$, near the leading edge, the incident vortex is positioned above the wing. With increasing distance along the wing, the incident vortex eventually moves below the wing, due to the vertical component of its orbital motion, and positive axial vorticity is formed along the wing tip. Additionally, a region of negative axial vorticity is formed along the bottom surface of the wing near the trailing edge.

*5.5.2 Cross-Sectional Patterns of Axial Vorticity and Streamline Topology*

Figure 5.10 provides sectional slices of axial vorticity $\omega_x C/U_\infty$ at the midchord of the wing $x'/C_{fw} = 0.5$ for the inboard interaction $\Delta y/C_{fw} = 0.25$. Images are shown as function of phase angle $\Phi$. At $\Phi = 0$, the incident vortex is positioned above the wing and a small layer of negative vorticity is induced along the top surface of the wing. As the incident vortex moves downward, at $\Phi = \pi/2$ it is evident that, its structure bifurcates with portions existing above and below the wing. This bifurcated pattern of vorticity is initiated when the incident vortex impinges upon the leading edge of the wing. At larger values of phase angle $\Phi = 3\pi/4$ and $\Phi = \pi$, the concentration of vorticity below the wing becomes dominant and, furthermore, the region of negative blue vorticity along the bottom surface of the wing becomes more prevalent. At $\Phi = 5\pi/4$ to $\Phi = 7\pi/4$ the aforementioned processes are reversed, that is, the magnitude and scale of the vorticity concentration above the wing increase, while the concentration below the wing is attenuated. This fluctuation in the axial vorticity of the incident vortex arises during its formation along the tip of the oscillating leader wing. In addition to these developments of the incident vortex, formation of a positive (red-yellow) axial vorticity concentration

occurs at the tip of the wing, attaining its largest magnitude and scale of axial vorticity at values of phase angle $\Phi = \pi/2$ to $\Phi = \pi$. Since the tip of the wing is located well outboard inboard of the incident, it is exposed to a region of vortex downwash extending outboard of the wingtip. In fact, for both of the vorticity concentrations on the upper and lower sides of the wing, the sign of the induced downwash is the same, and therefore the induced effects of both concentrations reinforce one another. Due to the angle of attack of the leader wing, only significant downwash is induced during part of the oscillation cycle.

Figure 5.11a provides sectional streamline patterns superposed on patterns of axial vorticity $\omega_x C/U_\infty$ for the inboard interaction $\Delta y/C_{fw} = 0.25$. All images are at the midchord of the wing $x'/C_{fw} = 0.5$ for four values of phase angle $\Phi$. At $\Phi = 0$, a larger image of this is provided in Figure 5.11b, a focus F1 is evident at the center of the incident vortex above the wing and a F2 is evident below the wing. This focus F2 is associated with a concentration of axial vorticity as the incident vortex moves below the wing at subsequent phases. Half saddle point S1 occurs at the indicated locations just inboard of the tip of the wing. At $\Phi = \pi/2$, the incident vortex impinges directly onto the leading edge of the wing and portions are evident along both sides. Foci F1 and F2 corresponding to the bifurcated concentrations of axial vorticity are evident above and below the wing. A half saddle point S1 occurs at the indicated locations just inboard of the tip of the wing along the top surface. A third focus F3 is present inboard of focus F1 with a saddle point S3 allowing compatibility between the two regions of axial vorticity. Focus F3 arises from the distortion of the incident vortex at the leading edge. Separation

and reattachment streamlines are evident at the tip of the wing at $\Phi = \pi/2$, in association with the region of positive (red-yellow) vorticity. This vorticity concentration is associated with focus F4 at the wingtip. Saddle point S2 allows for compatibility between focus F2 and focus F4. At $\Phi = \pi$ and $\Phi = 3\pi/2$, flow separation at the wingtip occurs without reattachment. At $\Phi = \pi$, the flow topology is identical to that of $\Phi = \pi/2$ minus the occurrence of flow reattachment and the corresponding focus F4. Viewing the streamline topology of Figure 5.11a as a whole, the orientation of the streamlines immediately outboard of the tip of the wing is in the downward direction, corresponding to the aforementioned downwash of the incident vortex. This region of the streamline pattern is compatible with the direction of the streamlines induced by the major concentrations of axial vorticity above and below the wing. In this regard, half saddle points occur at the indicated locations just inboard of the tip of the wing such as those indicated at $\Phi = 3\pi/2$.

Figure 5.11c shows streamline topology (top), line contours of upwash velocity $w/U_\infty$ (middle) and line contours of spanwise velocity $v/U_\infty$ (bottom) overlaying axial vorticity $\omega_x C/U_\infty$. The image is taken at $\Phi = 0$ at a streamwise location $x'/C_{fw} = 0.5$. Solid lines correspond to positive velocity and dashed lines correspond to negative velocity. The primary mechanism of negative axial vorticity generation along the wing is due to the gradient of the spanwise velocity compnent of the incident vorticity. Essentially, shear flow is occurring across the wing due to the spanwise velocity of the incident vortex which results in an eruption of the boundary layer along the wing. This gradient

corresponds to the change in spanwise velocity extending over the vertical distance from the surface of the wing to the center of the incident vortex.

Figure 5.12 shows streamline patterns overlaying sectional slices of axial vorticity $\omega_x C/U_\infty$ for the inboard interaction $\Delta y/C_{fw}$ = 0.25. Images are shown as functions of streamwise distance $x'/C_{fw}$ at phase angles $\Phi = \pi/2$ and $\Phi = 3\pi/2$. This figure examines the streamwise evolution in flow topology when the incident vortex moves upward across the top of the wing tip at $\Phi = \pi/2$ and when it moves downward below the wing tip at $\Phi = 3\pi/2$. At $\Phi = \pi/2$, foci F1 and F2 are associated with regions of axial vorticity above and below the wing at $x'/C_{fw}$ = 0.25 and $x'/C_{fw}$ = 0.5. The concentration of vorticity associated with F2 is attenuated at $x'/C_{fw}$ = 0.75 and $x'/C_{fw}$ = 1, as the vortex moves above the wing.

At the tip of the wing, a region of positive vorticity is present and streamlines indicate flow separation occurs at $x'/C_{fw}$ = 0.25. Half saddle points S1 and S2 allow for compatibility between the topology of focus F1 and F2, respectively, and the flow separating at the tip. Reattachment occurs at $x'/C_{fw}$ = 0.5 and focus F4 is evident.

A saddle point S3 is present inboard of focus F1 and allows compatibility between it and the flow topology corresponding to the distorted incident vortex. At $x'/C_{fw}$ = 0.5, this distorted vorticity concentration coincides with focus F3. At $x'/C_{fw}$ = 1, vorticity at the tip is largely attenuated, as the incident vortex is positioned mostly above the wing.

At $\Phi = 3\pi/2$, the incident vortex is positioned above the wing at $x'/C_{fw}$ = 0.25 and a corresponding focus F1 is evident. At the tip of the wing, separation is evident and

reattachment occurs on the bottom surface of the wing at $x'/C_{fw}$ = 0.25. Half saddle point S1 allows for compatibility between focus F1 and the separated flow at the tip. Similarly, saddle point S2 allows for compatibility between the reattached flow and the winding flow topology associated with focus F2 below the wing. This focus is not associated with large magnitude vorticity, which has been attenuated. With increasing distance along the wing, from $x'/C_{fw}$ = 0.75 to $x'/C_{fw}$ = 1 portions of the incident vortex are evident on both sides of the wing with the larger magnitude vorticity eventually being associated with focus F2. Additionally, from $x'/C_{fw}$ = 0.5 to $x'/C_{fw}$ = 1, reattachment of the flow separated at the tip does not occur. However, the previously described flow topology remains consistent.

Figure 5.13 shows volumetrically reconstructed images of sectional slices of axial vorticity $\omega_x C/U_\infty$ for the aligned interaction $\Delta y/C_{fw}$ = 0.25. A trimetric orientation is provided in conjunction with an inlay of a plan view orientation. The wing is semi-transparent such that structures on both sides are visible, i.e. structures on the bottom surface of the wing appear less vibrant. At $\Phi$ = 0, the incident vortex is located above wing at all streamwise distances and a small region of negative vorticity forms beneath the vortex along the top surface of the wing as it approaches the trailing edge. As the incident vortex moves downward and impinges directly on the leading edge of the wing, from $\Phi = \pi/4$ to $\Phi = \pi$, a region of positive axial vorticity forms along the tip of the wing. This occurs due to the enhanced downwash of the incident vortex extending across the tip of the wing. Along the bottom surface of the wing, negative vorticity is evident as well.

The region of positive axial vorticity at the tip is attenuated from $\Phi = 5\pi/4$ to $\Phi = 7\pi/4$ where the incident vortex is positioned above the wing near the leading edge.

## 5.6 CONCLUSIONS

The spanwise impingement location of the incident vortex along the leading edge of the flat wing dictates the mode of interaction that occurs. In the case of the perturbed trailing vortex, inherent variations of the strength and position of the incident vortex during the oscillation cycle of the orbital motion result in specific space-time variations of the flow structure along the wing for the aligned and inboard modes of interaction.

If the incident vortex is aligned with the wingtip, an opposite-signed vortex is induced at the tip of the wing. At any streamwise location along the wing, formation of a dipole occurs at the tip of the wing. Patterns of streamline topology show that this dipole rotates around the wingtip. This occurs as a result of the time-dependent variation of the vertical position and circulation of the incident vortex. During part of the oscillation cycle, only very small scale, low-level vortices are induced due to breaking of the continuous structure of the incident vortex along the tip of the wing; that is, the incident vortex is initially above the wing in the leading region, is abruptly bifurcated at mid-chord then exists below the wing in the trailing region of the tip. During this process, the magnitude of the streamwise vorticity of the incident vortex is substantially attenuated.

If the incident vortex is positioned inboard of the tip, a bifurcation occurs as it impinges on the leading edge of the wing. The formation of a tip vortex of positive sign occurs in conjunction with the bifurcation, as a result of the vortex downwash that causes separation at the tip of the wing. Moreover, vorticity of opposite sign, relative to that of the incident vortex, is evident along the wing surface during this bifurcation and when it is positioned above the wing, as a result of the eruption of the boundary layer along the wing due to the presence of the incident vortex.

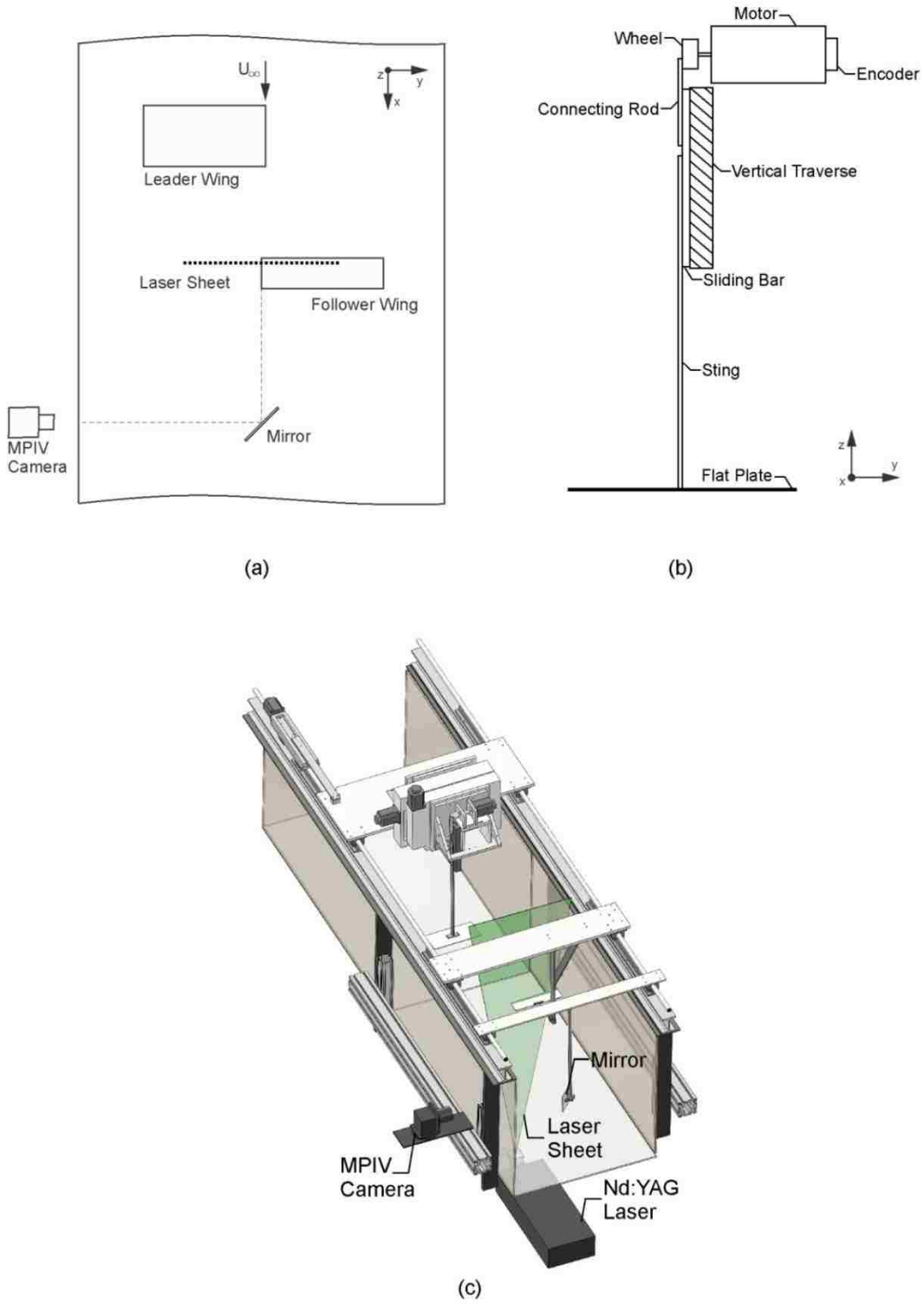


**Figure 5.1:** Overview of experimental apparatus. (a) Schematic of particle image velocimetry system. (b) Schematic of wing oscillation mechanism (not to scale). (c) Model of test section and experimental system.

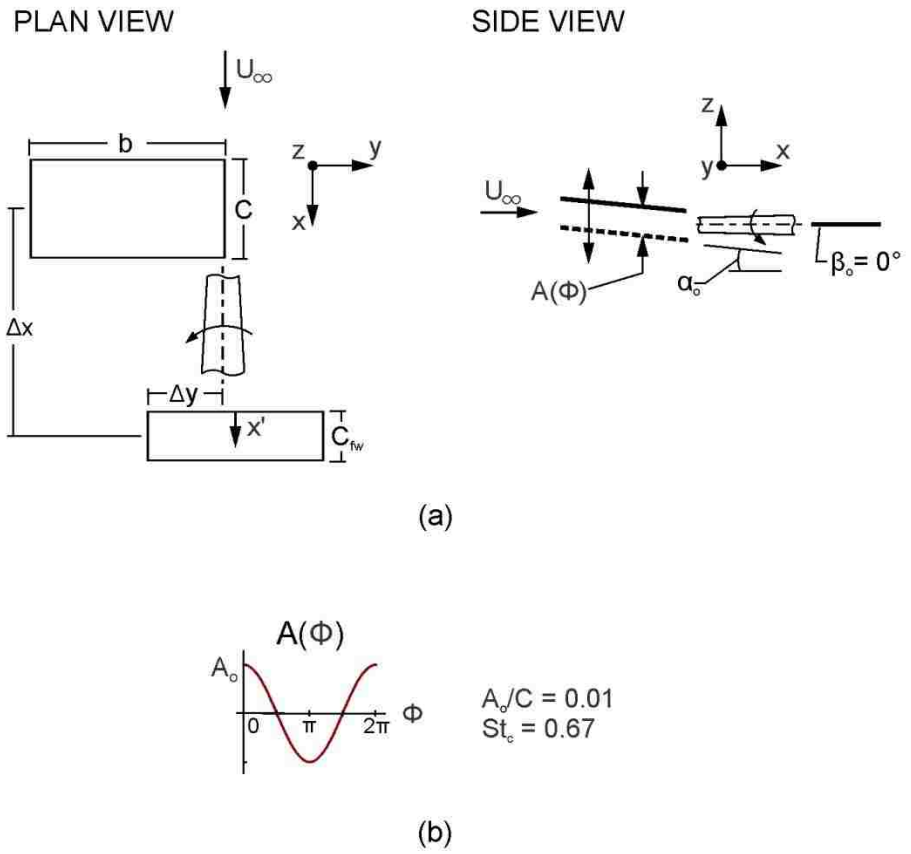


**Figure 5.2:** Overview of wing setup. (a) Plan and side view schematics of tandem wings. (b) Motion profile of leader wing.

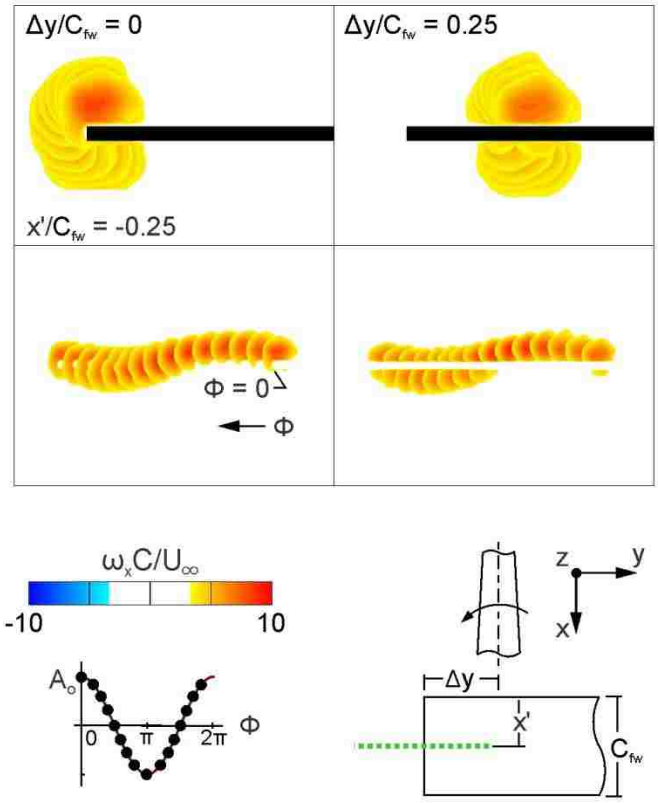


**Figure 5.3:** Time sequence of sectional slices of axial vorticity $\omega_x C/U_\infty$ upstream of the leading edge of the wing $x'/C_{fw}$ = - 0.25. The left and right columns of images correspond respectively to aligned $\Delta y/C_{fw}$ = 0 and inboard $\Delta y/C_{fw}$ = 0.25 interactions of the incident vortex with the wing. In the top row of images, the view is in the upstream direction and instantaneous slices are superposed. In the bottom row of images, the view is at an angle with respect to the axis of the vortex.

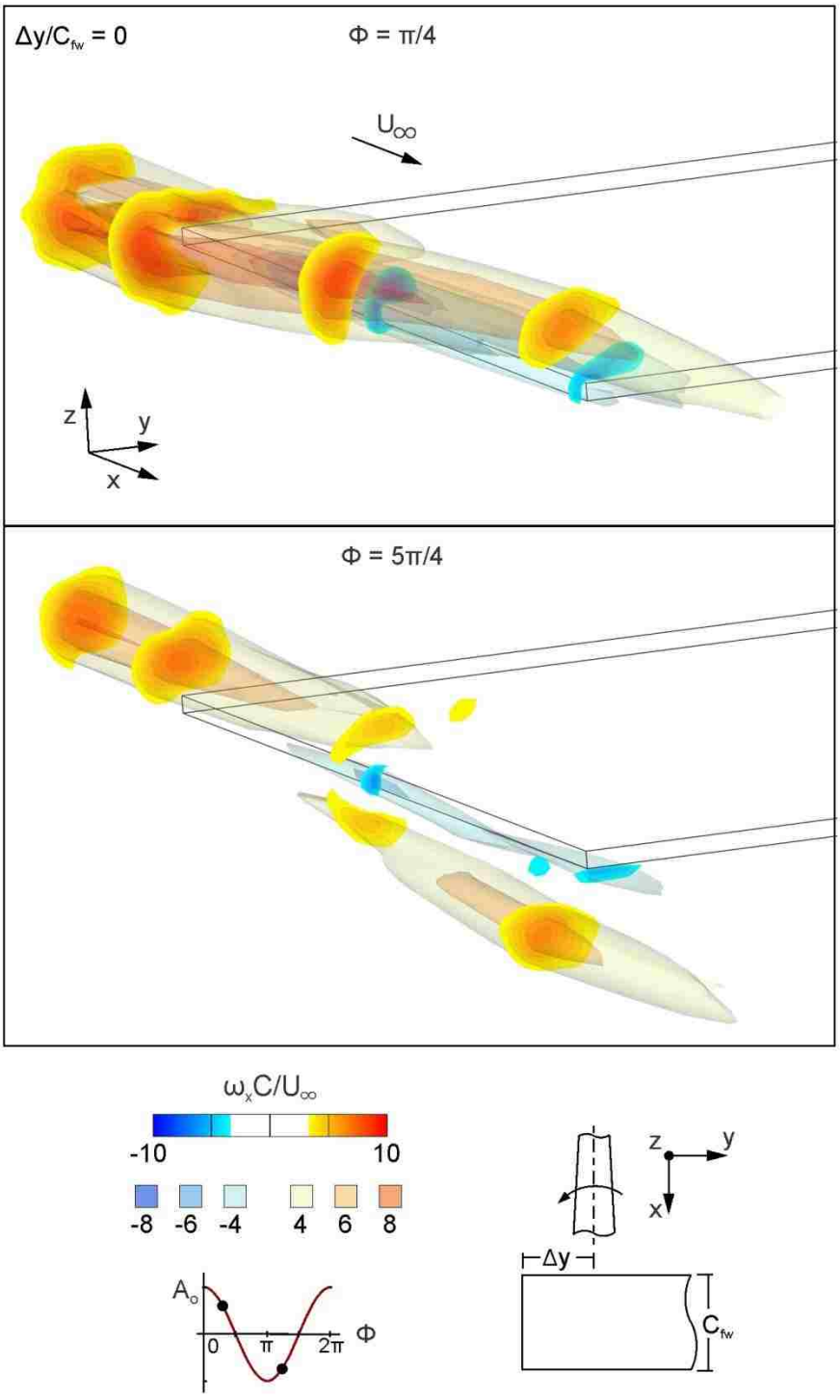


**Figure 5.4:** Overview of the flow structure for the aligned interaction $\Delta y/C_{fw} = 0$. Sectional slices of (red-yellow) axial vorticity are overlaid on (yellow-brown) iso-surfaces of axial vorticity $\omega_x C/U_\infty$. Phase angles $\Phi = \pi/4$ and $\Phi = 5\pi/4$ are shown.

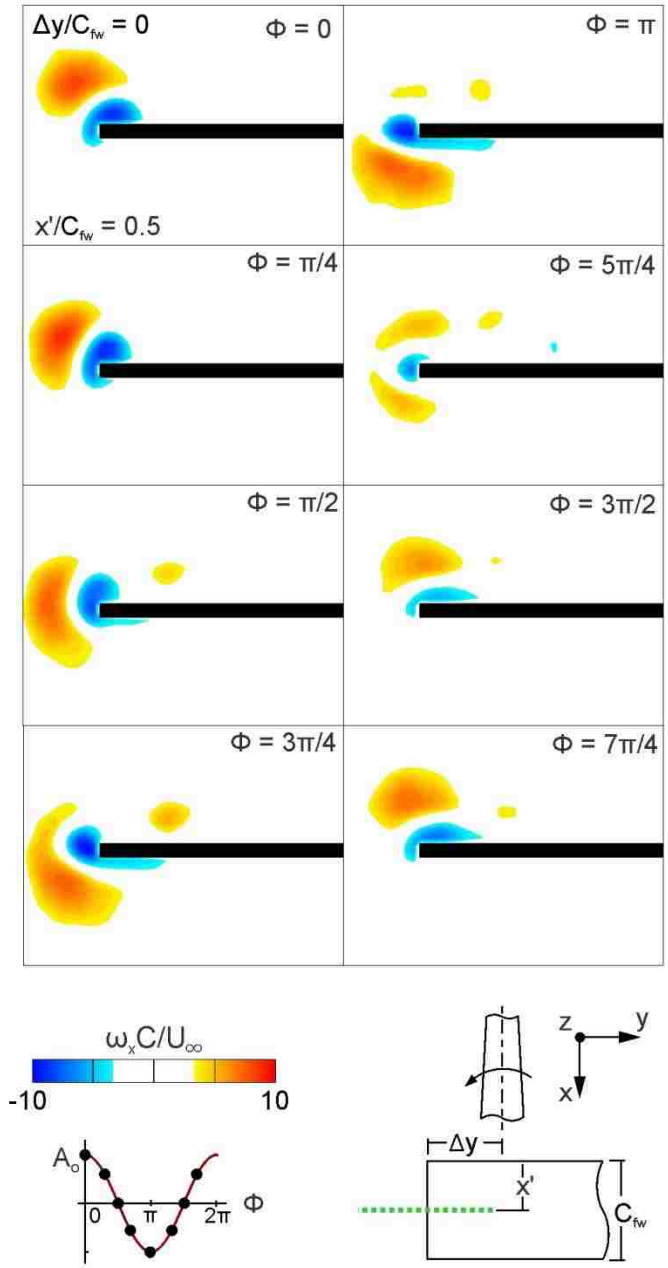


**Figure 5.5:** Sectional slices of axial vorticity $\omega_x C/U_\infty$ at the midchord of the wing $x'/C_{fw}$ = 0.5 are presented for the aligned interaction $\Delta y/C_{fw}$ = 0. Images are shown as function of phase angle $\Phi$.

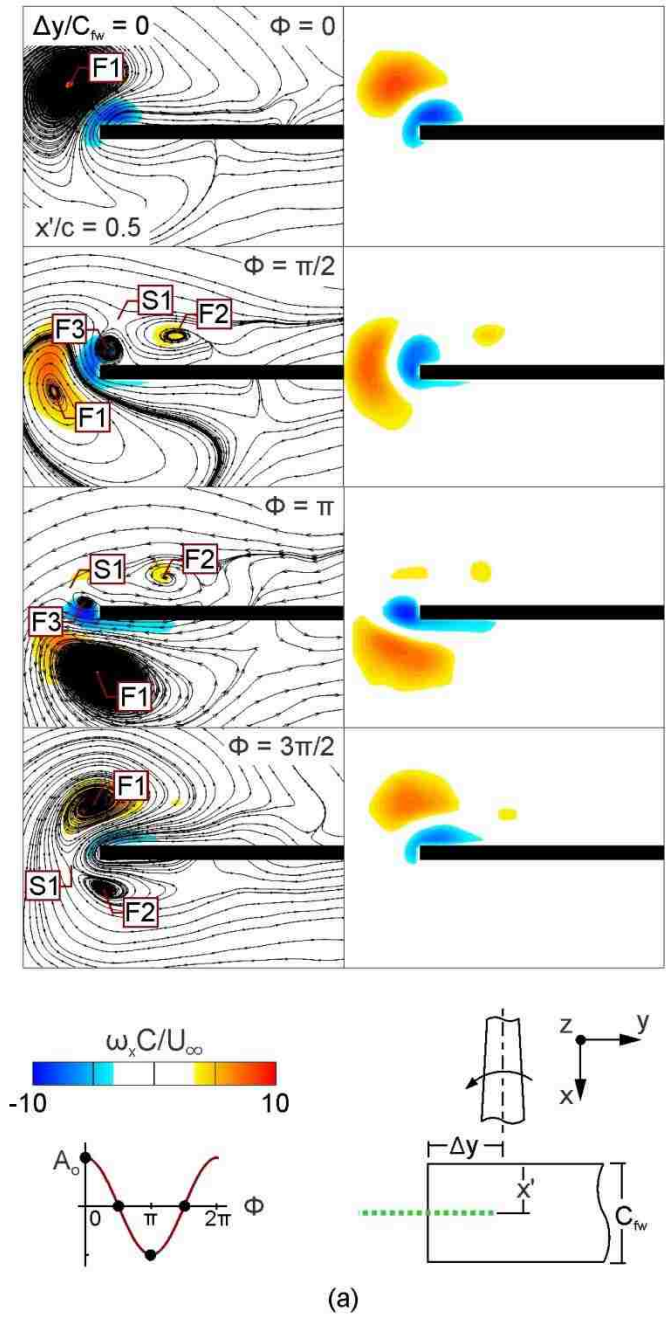


(a)

**Figure 5.6:** Streamline topology superposed on sectional slices of axial vorticity $\omega_x C/U_\infty$ at the midchord of the wing $x'/C_{fw} = 0.5$ for the aligned interaction $\Delta y/C_{fw} = 0$. (a) Images are shown as function of phase angle $\Phi$.

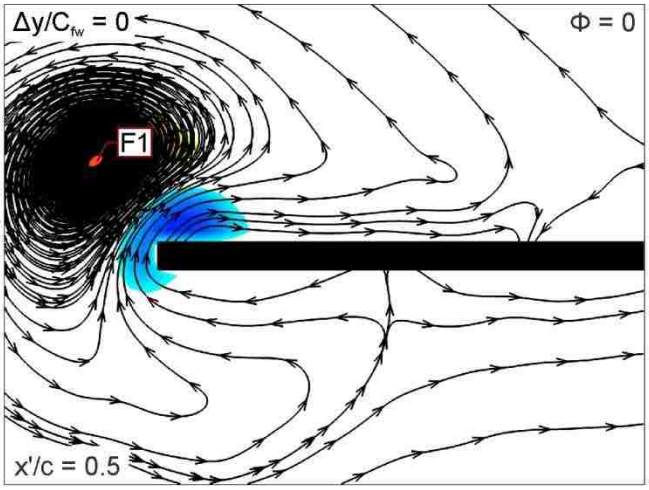


(b)

**Figure 5.6:** Streamline topology superposed on sectional slices of axial vorticity $\omega_x C/U_\infty$ at the midchord of the wing $x'/C_{fw} = 0.5$ for the aligned interaction $\Delta y/C_{fw} = 0$. (b) Images are shown at phase angle $\Phi = 0$.

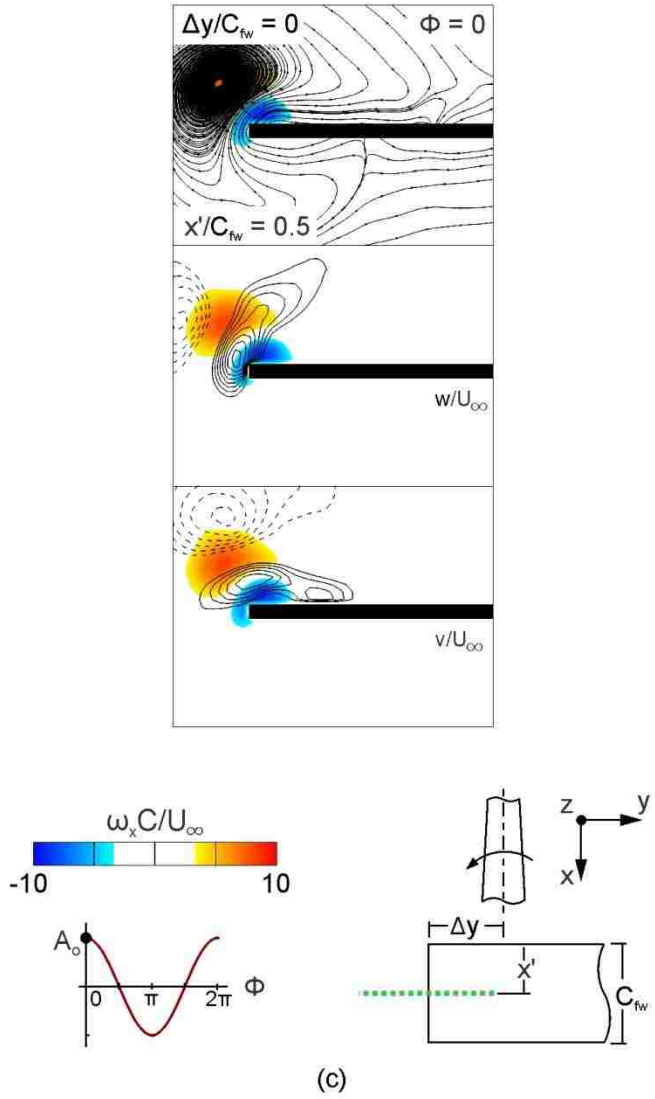


**Figure 5.6:** Overview of flow structure at $\Phi = 0$ at a streamwise location $x'/C_{fw} = 0.5$ (c) Streamline topology, line contours of upwash velocity $w/U_\infty$ and line contours of spanwise velocity $v/U_\infty$ overlaying axial vorticity $\omega_x C/U_\infty$.

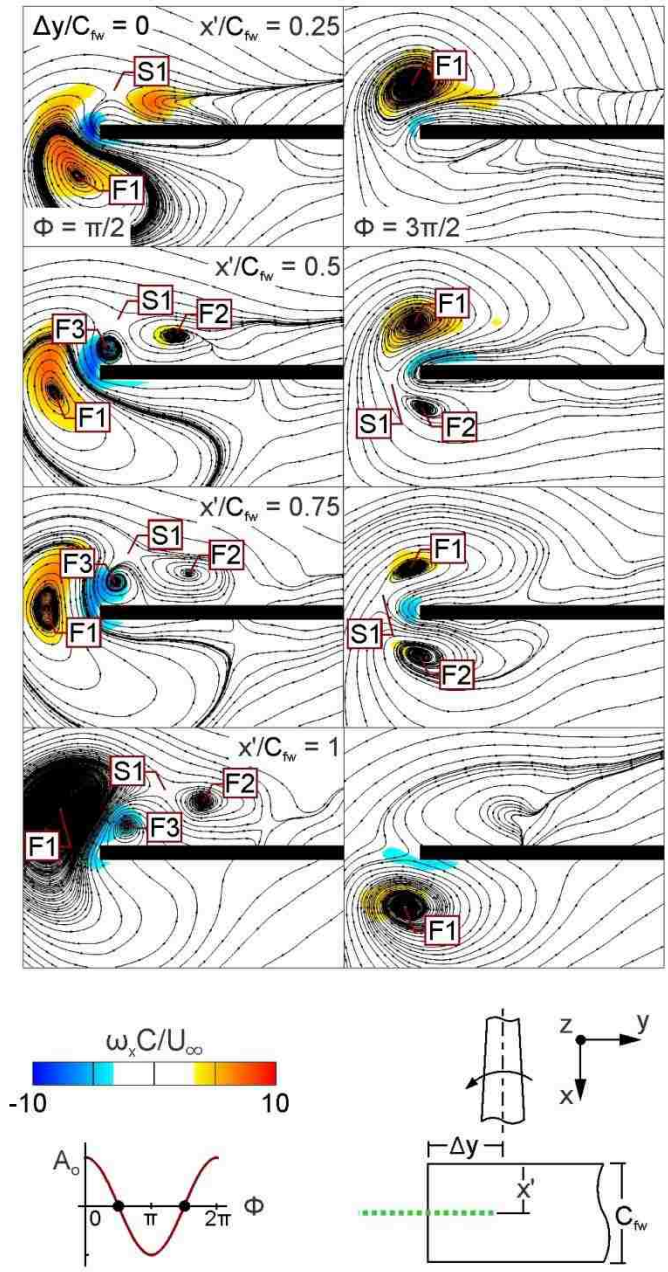


**Figure 5.7:** Streamline patterns overlaying sectional slices axial vorticity $\omega_x C/U_\infty$ are shown for the aligned interaction $\Delta y/C_{fw} = 0$. Images are shown as a function of streamwise distance $x'/C_{fw}$ at for phase angles $\Phi = \pi/2$ and $\Phi = 3\pi/2$.

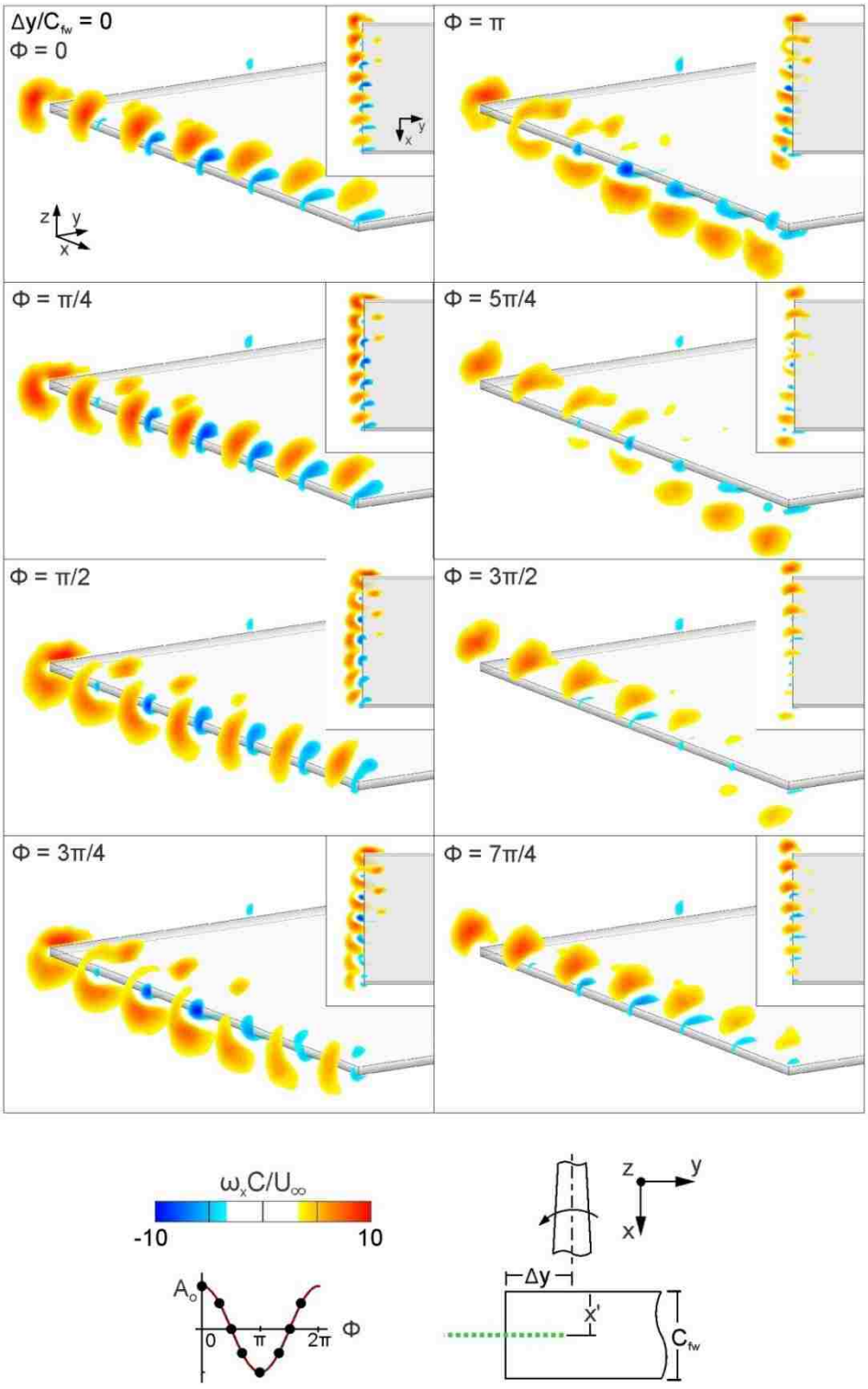


**Figure 5.8:** Volumetrically reconstructed images of sectional slices of axial vorticity $\omega_x C/U_\infty$ for the aligned interaction $\Delta y/C_{fw} = 0$. Images are shown as function of phase angle $\Phi$. A trimetric orientation is provided in conjunction with an inlay of a plan view orientation.

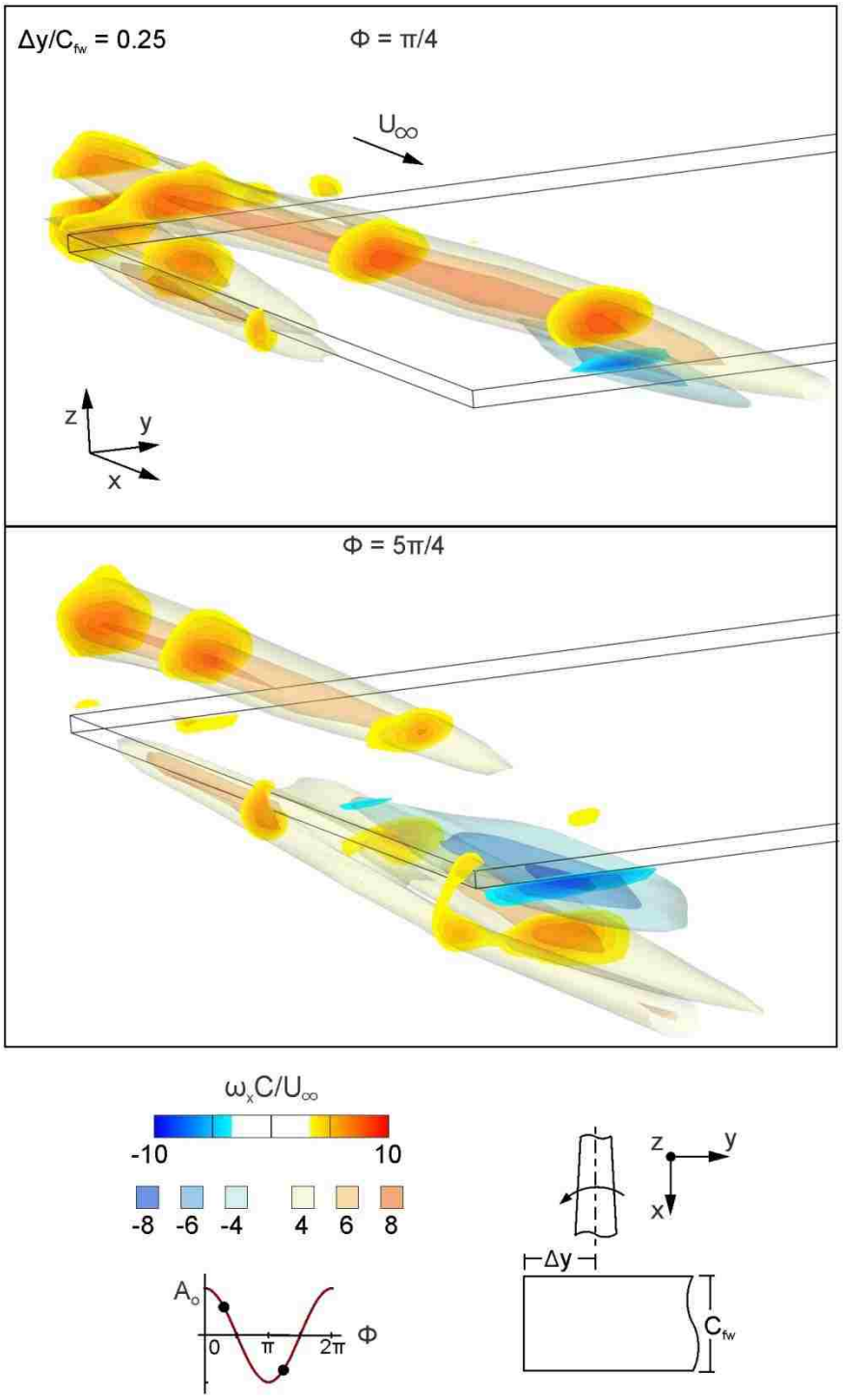


**Figure 5.9:** Overview of the flow structure for the aligned interaction $\Delta y/C_{fw}$ = 0.25. Sectional slices of (red-yellow) axial vorticity are overlaid on (yellow-brown) iso-surfaces of axial vorticity $\omega_x C/U_\infty$. Phase angles $\Phi = \pi/4$ and $\Phi = 5\pi/4$ are shown.

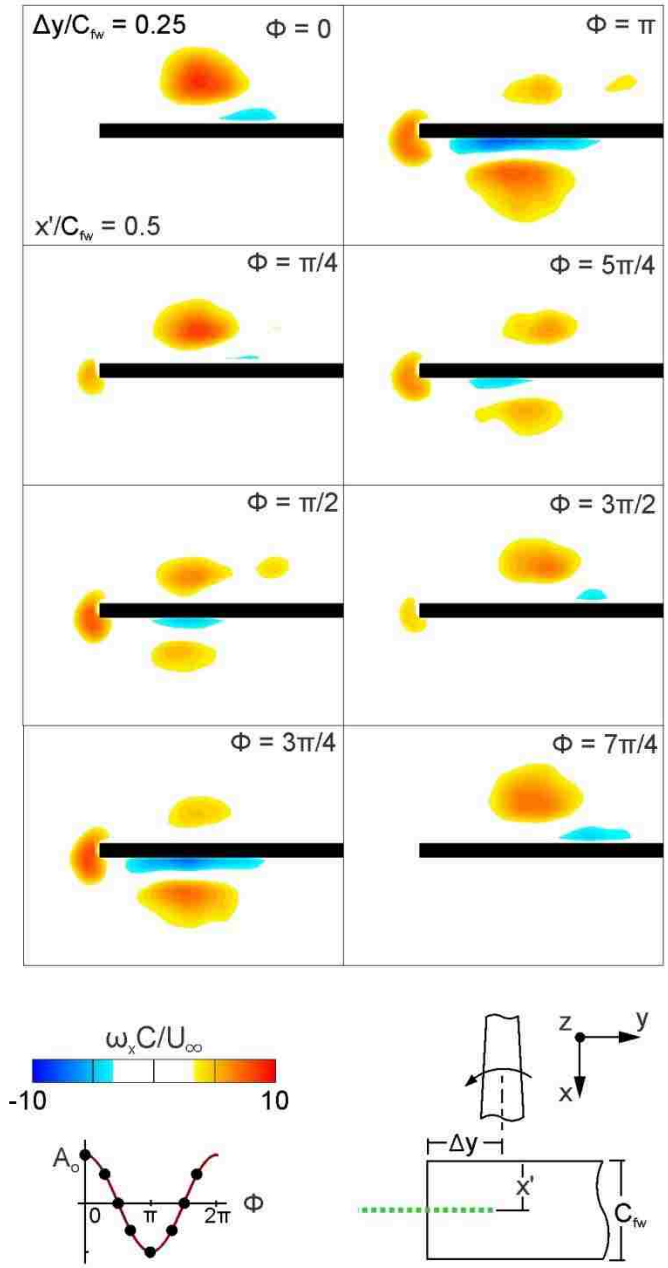


**Figure 5.10:** Sectional slices of axial vorticity $\omega_x C/U_\infty$ at the midchord of the wing $x'/C_{fw}$ = 0.5 are presented for the inboard interaction $\Delta y/C_{fw}$ = 0.25. Images are shown as function of phase angle $\Phi$.

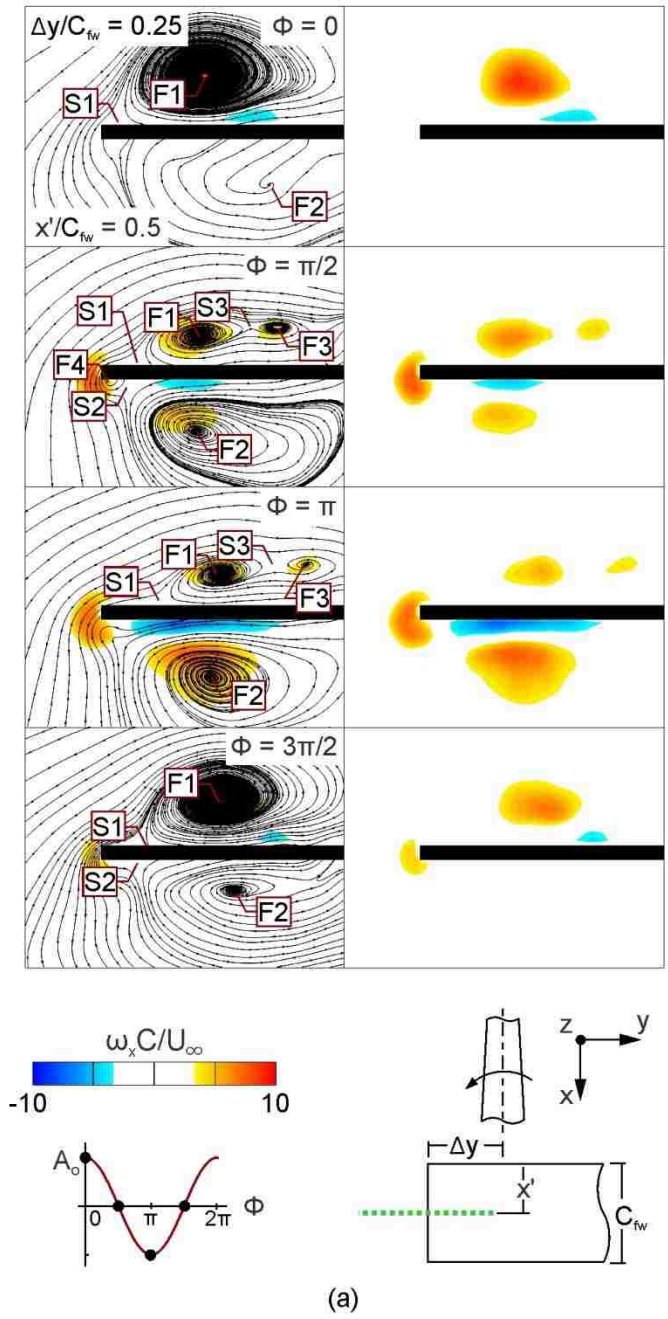


(a)

**Figure 5.11:** Streamline topology overlaying sectional slices of axial vorticity $\omega_x C/U_\infty$ at the midchord of the wing $x'/C_{fw}$ = 0.5 for the inboard interaction $\Delta y/C_{fw}$ = 0.25. (a) Images are shown as function of phase angle $\Phi$.

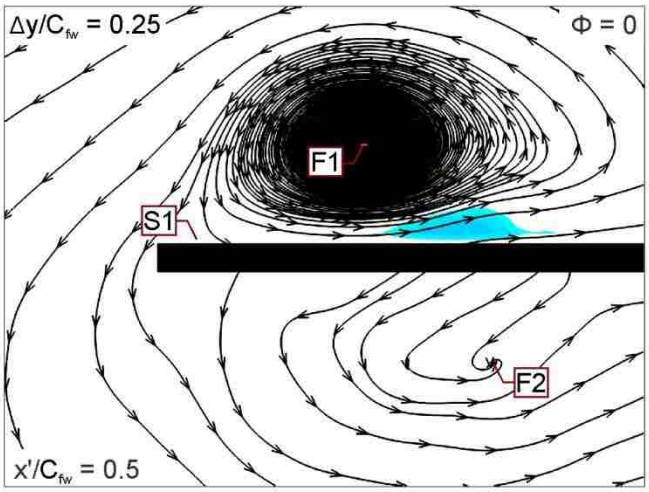


(b)

**Figure 5.11:** Streamline topology superposed on sectional slices of axial vorticity $\omega_x C/U_\infty$ at the midchord of the wing $x'/C_{fw} = 0.5$ for the inboard interaction $\Delta y/C_{fw} = 0.25$. (b) Images are shown at phase angle $\Phi = 0$.

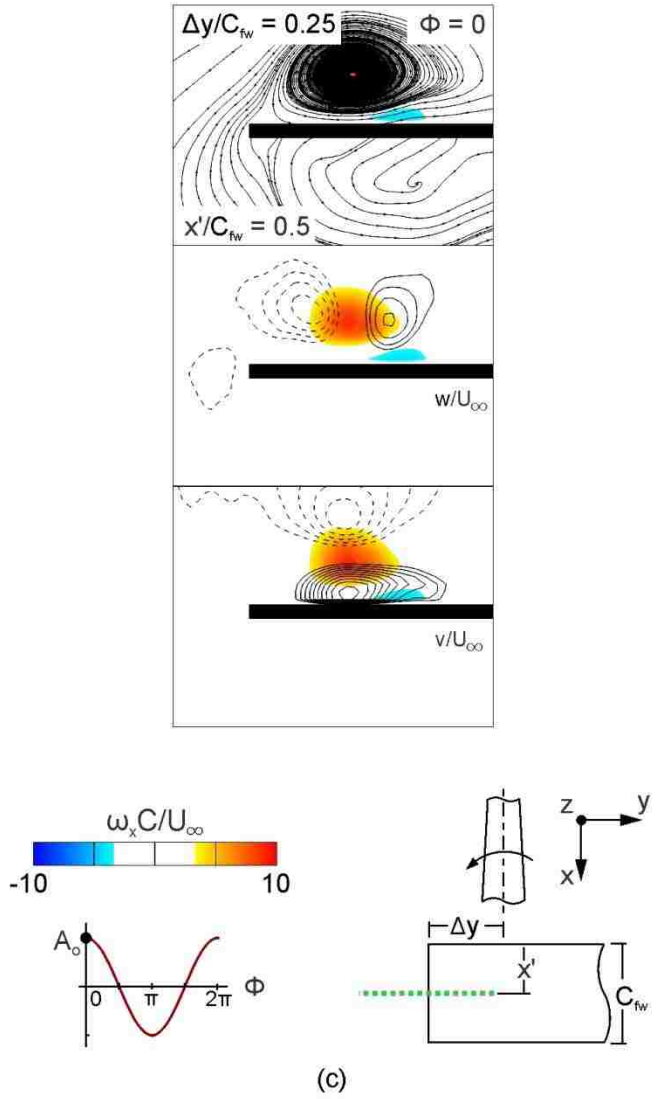


**Figure 5.11:** Overview of flow structure at $\Phi = 0$ at a streamwise location $x'/C_{fw} = 0.5$ (c) Streamline topology, line contours of upwash velocity $w/U_\infty$ and line contours of spanwise velocity $v/U_\infty$ overlaying axial vorticity $\omega_x C/U_\infty$.

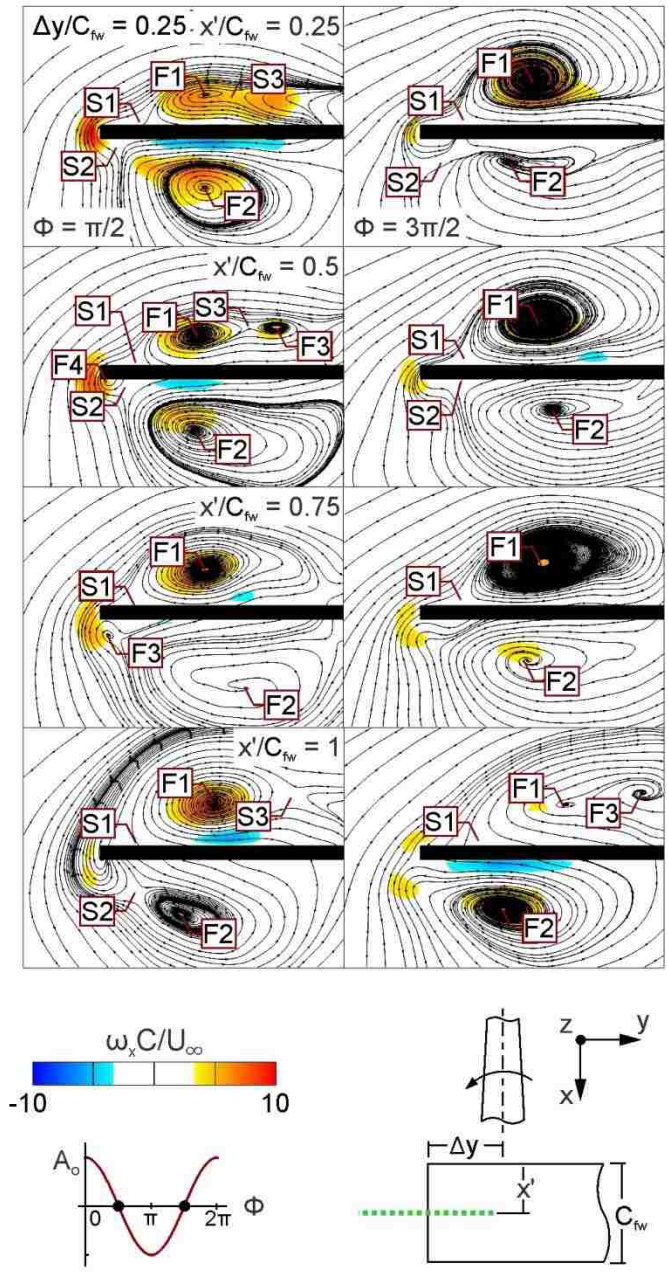


**Figure 5.12:** Streamline patterns overlaying sectional slices axial vorticity $\omega_x C/U_\infty$ are shown for the inboard interaction $\Delta y/C_{fw}$ = 0.25. Images are shown as a function of streamwise distance $x'/C_{fw}$ at for phase angles $\Phi = \pi/2$ and $\Phi = 3\pi/2$.

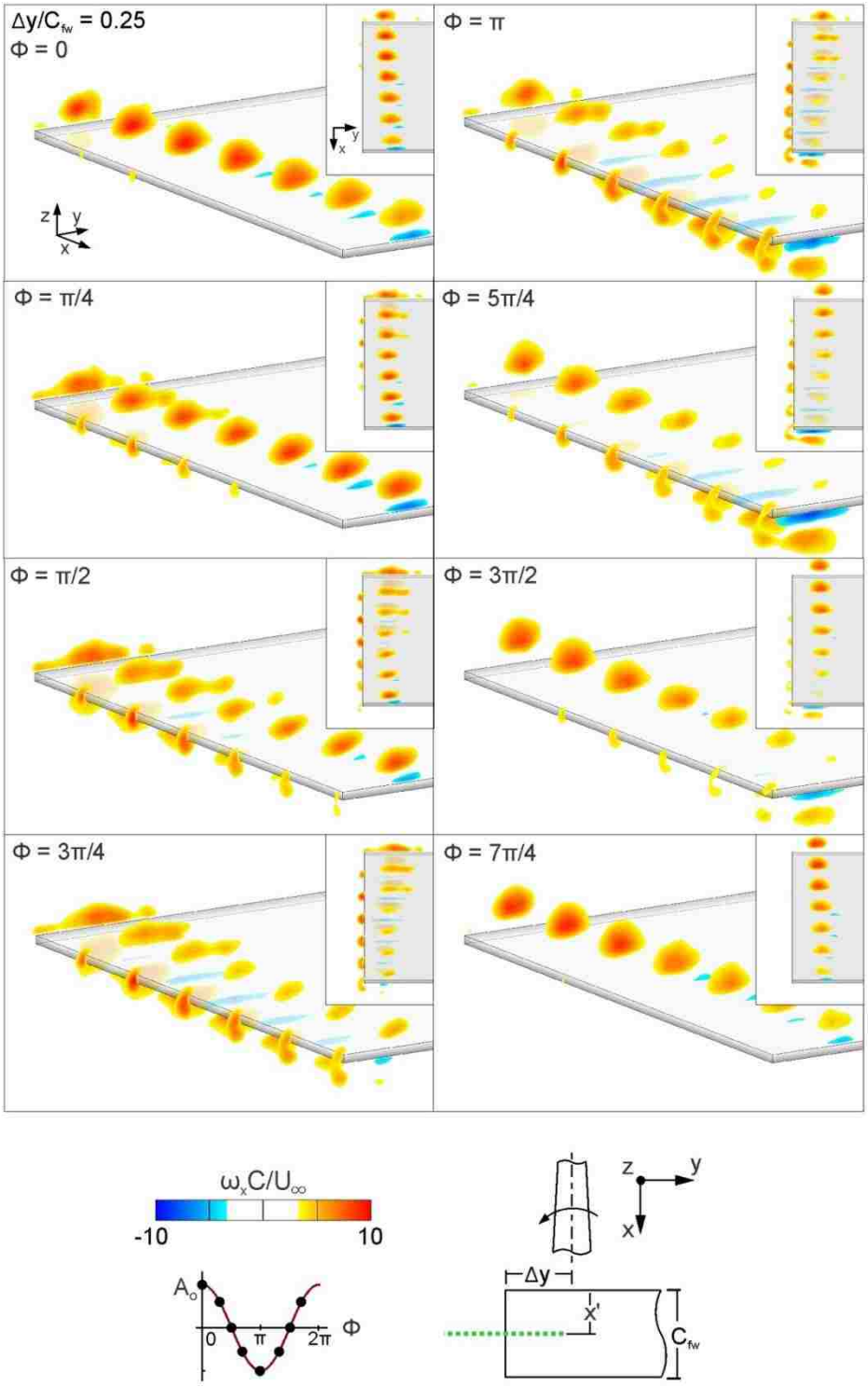


**Figure 5.13:** Volumetrically reconstructed images of sectional slices of axial vorticity $\omega_x C/U_\infty$ for the inboard interaction $\Delta y/C_{fw}$ = 0.25. Images are shown as function of phase angle $\Phi$. A trimetric orientation is provided in conjunction with an inlay of a plan view orientation.

# CHAPTER 6

# CONCLUSIONS AND RECOMMENDATIONS

## 6.1 CONCLUSIONS

This investigation focuses on the three-dimensional flow structure of a vortex from a wing subject to small-amplitude heaving oscillations, as well as the interaction of the vortex with a downstream (follower) wing. Experiments were conducted in a large-scale water channel using a novel design that allowed precise motion control and positioning of a leader wing and a follower wing. Quantitative measurements were made using monoscopic and stereoscopic particle image velocimetry to determine the flow structure of a perturbed trailing vortex and its interaction with a downstream wing. Data were processed using in-house software to analyze patterns of phase-averaged and time-averaged flow parameters.

A trailing vortex from a wing undergoing small-amplitude heaving oscillations and its interaction with a secondary wing was characterized. The displacement amplitude of the heaving oscillations was on the order of the vortex radius. The flow structure of the single perturbed trailing vortex was determined over a region extending from the trailing edge of the wing to five wing chords downstream. Volumetrically reconstructed images, as well as cross-sectional image slices, revealed features of the flow structure that were

common to the perturbed trailing vortex over several perturbation frequencies. This includes alternating regions of enhanced axial velocity deficit and azimuthal vorticity along the vortex, which occur in accord with the stability criterion of Leibowich & Stewartson (1983), as well as large variations in axial vorticity. The nature of the onset of orbital motion in these perturbed trailing vortices was characterized in relation to these flow features as a result of the perturbation. In the case of the perturbed vortex-wing interaction, the flow structure along the follower wing was characterized using cross-sectional images at two different spanwise locations of vortex impingement: aligned with the tip of the follower wing and inboard of its tip. Patterns of axial vorticity, velocity and streamlines were utilized to reveal differences of the flow topology for these locations of vortex impingement.

### *6.1.1 Structure of a Trailing Vortex from a Perturbed Wing*

The structure of a trailing vortex from a wing undergoing very small amplitude, low frequency heaving motion is investigated using space-time images acquired via stereo particle image velocimetry. The unsteady motion of the wing induces large undulations in axial velocity deficit and circulation along the vortex and thereby corresponding changes of the swirl ratio. These fluctuations are accompanied by organized patterns of azimuthal vorticity encompassing regions of axial velocity deficit.

Along the vortex, the onset of pronounced azimuthal vorticity occurs in conjunction with regions of large magnitude axial velocity deficit, which also coincide with low values of swirl ratio. As the minimum value of swirl ratio is approached, onset

of pronounced azimuthal vorticity occurs, and its pattern shows the largest magnitude and scale when minimum swirl ratio is attained. The onset of the pattern of azimuthal vorticity follows an orderly process of motion about the axis of the vortex until a ring-like structure occurs. Subsequently attenuation of the magnitude and scale of this pattern is evident. Volumetric representations of the axial velocity deficit, axial vorticity and azimuthal vorticity depict these variations of along the axis of the vortex.

The theoretical analysis of Leibowich & Stewartson (1983) establishes that when the swirl ratio $q < \sqrt{2}$, a range of azimuthal wave numbers may be amplified, potentially leading to destabilization. This criterion for $q$ provides a consistent threshold for onset of pronounced azimuthal vorticity. The onset of maximum magnitude and scale of azimuthal vorticity corresponds to the onset of disorder of the instantaneous axial vorticity fluctuations. Comparison of the present experiments in the region of decreasing swirl ratio with the computations and theoretical interpretations of Viola et al (2016) show that the same form of the m = 1 mode occurs. In the region of increasing swirl ratio, the experimental pattern of instantaneous axial vorticity fluctuation shows a highly concentrated and coherent core followed by its eventual attenuation.

### *6.1.2 Onset of Orbital Motion in a Trailing Vortex from an Oscillating Wing*

Over a range of Strouhal number, the trajectory of a trailing vortex from an oscillating wing exhibits markedly different characteristics. Despite this, there are a number of generic physical mechanisms of the perturbed vortex that are evident when

comparing space-time representations of axial and azimuthal vorticity, axial velocity deficit and swirl ratio.

At low Strouhal number, the amplitude of the unidirectional excursion of the vortex remains essentially constant with streamwise distance. At moderate Strouhal number, the initial region of the vortex motion is unidirectional, but at larger streamwise distance, excursions of the vortex occur orthogonal to its initial unidirectional motion, thereby giving rise to an elliptical orbital trajectory that acts in the opposite direction to that of the circulation of the vortex. At high Strouhal number, the amplitude of the vortex undulation increases by nearly an order of magnitude with streamwise distance, and pronounced orbital motion of the vortex has the same sense as the vortex circulation at all streamwise distances. The onset of orbital motion can be attributed to induction effects described in Hama & Nuntant (1961). Additionally, at the highest frequency, small amplitude lateral motion of the forming vortex at the trailing edge of the wing arises due to a phase shift between the vortex roll-up and the wing oscillation.

Regardless of the value of the Strouhal number of the imposed perturbation, several generic physical mechanisms occur along an undulating vortex. These mechanisms are evident at the trailing edge of the wing and are consistent at all streamwise distances. In both of the cases where orbital motion occurs, the scale of the region of enhanced axial velocity deficit is large compared to the scale of the region of axial vorticity. Changes in vortex curvature are correlated with extreme values of axial vorticity and swirl ratio, as well as with the onset and attenuation of pronounced azimuthal vorticity. The onset of pronounced azimuthal vorticity coincides with regions

of enhanced axial velocity deficit at the trailing edge of the wing and at all streamwise distances for all frequencies. It consistently occurs when the swirl ratio $q < \sqrt{2}$, in accord with onset of convective instability of azimuthal modes Leibovich & Stewartson (1983). The degree to which the value of swirl ratio varies during the undulation cycle of the vortex is directly related to the excitation frequency; that is, higher frequencies produce larger variations.

### *6.1.3 Interaction of a Perturbed Trailing Vortex with a Wing*

The spanwise impingement location of the incident vortex along the leading edge of the flat wing dictates the mode of interaction that occurs. In the case of the perturbed trailing vortex, inherent variations of the strength and position of the incident vortex during the oscillation cycle result in specific space-time variations of the flow structure along the wing for the aligned and inboard modes of interaction.

If the incident vortex is aligned with the tip of the wing, an opposite-signed vortex is induced. At any streamwise location along the chord of the wing, the streamline topology indicates a dipole formation at the tip of the wing. This dipole rotates around the tip as a result of the time-dependent variation of the vertical position and circulation of the incident vortex. During part of the oscillation cycle, only very small scale, low-level induced vortices are generated due to breaking of the continuous structure of the incident vortex along the tip of the wing, that is, the incident vortex is initially above the wing in the leading region, is abruptly bifurcated at mid-chord then exists below the wing in the trailing region of the tip. During this process, the magnitude of the streamwise vorticity of the incident vortex is substantially attenuated. If the incident vortex is positioned

inboard of the tip, a bifurcation occurs as it impinges on the leading edge of the wing. The formation of a tip vortex of positive sign occurs in conjunction with the bifurcation, as a result of the vortex downwash that causes separation at the tip of the wing. Moreover, vorticity of opposite sign, relative to that of the incident vortex, is evident across the wing surface during this bifurcation, as a result of the gradient of spanwise velocity in the vertical direction. That is, the change in spanwise velocity extending over the vertical distance from the surface of the wing to the center of the incident vortex.

## 6.2 RECOMMENDATIONS

This investigation has provided insight into the flow structure of a trailing vortex from an oscillating wing undergoing small-amplitude heaving motion, as well as the interaction of the unsteady, perturbed trailing vortex with a downstream (follower) flat plate, or wing. Based on the findings of the present investigations it is possible to recommend future studies of the following unexplored issues.

It has been demonstrated herein that the direction of orbital motion of the trailing vortex is different at high and low values of perturbation frequency. The detailed physics of the origin of this change in direction of rotation should be addressed by taking into account the variation of the phase difference between the wing motion and the forming vortex at successive values of finely-spaced frequency of the wing perturbation. The present study has shown that the onset of a phase shift is a critical aspect of onset of

orbital motion at a sufficiently high frequency, but further investigation of this aspect is called for.

From a practical aerodynamic standpoint, the technique employed in this investigation to induce perturbations of the trailing vortex involved controlled perturbations of the wing. This method of perturbation induces, of course, a time - dependent vertical displacement of the center of the vortex. In order to gain an understanding of the perturbed vortex structure in absence of vertical undulations, it would be of interest to design and implement a means of generating a vortex such that only perturbations of axial vorticity and azimuthal velocity occur. Using this approach, one could therefore isolate the effects of vertical undulations of the vortex.

For the perturbed vortex-wing interaction, it would be worthwhile to employ a follower wing at a non-zero angle of attack. The experiments performed herein serve as a canonical problem of a vortex impingement along a flat plate. Introducing an angle of attack to the follower wing would represent a more practical flow scenario. The primary objective of this type of investigation would be to determine the degree to which a perturbed incident vortex could modulate an existing tip vortex along a follower wing, relative to a steady vortex-wing interaction. More complex wing geometries could also be employed in subsequent studies.

Additionally, the effect of wing-flexibility has not been explored. The relationship between the perturbed incident vortex and a flexible follower wing on the development of the tip vortex would be of primary interest. Force measurements would indicate the

unsteady loading and modes of wing flexibility in relation to non-dimensional frequency and amplitude of the perturbed vortex. Characterizing these aspects in relation to the unsteady flow structure would be important.

Alternatively, introducing oscillations of the follower wing would serve to simulate flapping flight, commonly seen in biological fliers. Investigations have shown that oscillations of either the incident vortex or the follower wing greatly affect the flow structure along the follower wing. Further experiments could explore the effect of oscillation frequency of the system of wings, as well as the phase differences between them, on the unsteady flow structure and loading.

## REFERENCES


ADRIAN, R. J. & WESTERWEEL, J. 2011 Particle Image Velocimetry. Cambridge University Press.

BANGASH, Z. A., SANCHEZ, R.P., AHMED, A. & KHAN, M.J. 2006 Aerodynamics of Formation Flight. J. Aircraft 43 (4), 907-912.

BARNES, C. J., VISBAL, M. R. & GORDNIER, R. E. 2014a Investigation of aeroelastic effects in streamwise-oriented vortex/wing interactions. AIAA Paper 2014-1281. AIAA.

BARNES, C. J., VISBAL, M. R. & GORDNIER, R. E. 2014b Numerical simulations of streamwise-oriented vortex/ flexible wing interaction. AIAA Paper 2014-2313. AIAA.

BARNES, C. J., VISBAL, M. R. & GORDNIER, R. E. 2015 Analysis of streamwise-oriented vortex interactions for two wings in close proximity. Phys. Fluids 27, 015103.

BARNES, C. J., VISBAL, M. R. & GORDNIER, R. E. 2015b Effect of bending oscillations on a streamwise-oriented vortex interaction. AIAA Paper 2015-3303. AIAA.

BARNES, C. J., VISBAL, M.R. & HUANG, P.G. 2016 On the effects of vertical offset and core structure in streamwise-oriented vortex-wing interactions. J. Fluid Mech, 799, 128-158.

BATCHELOR, G. K. 1964 Axial flow in trailing line vortices. J. Fluid Mech. 20, 645–658.

BHAGWAT, M.J., CARADONNA, F.X. & RAMASAMY, M. 2015 Wing-vortex interaction: unraveling the flowfield of a hovering rotor. Exp. Fluids 56, 1-17.

BIRCH, D. & LEE, T. 2005 Investigation of the near-field tip vortex behind an oscillating wing.
J. Fluid Mech. 544, 201–241.

BRISTOL, R., ORTEGA, J., MARCUS, P. & SAVAŞ, Ö. 2004 On cooperative instabilities of parallel vortex pairs. J. Fluid Mech. 517, 331–358.

CALDERON, D. E., WANG, Z., GURSUL, I. & VISBAL, M. R. 2013 Volumetric measurements and simulations of the vortex structures generated by low aspect ratio plunging wings. Phys. Fluids. 25, 067102.

CHANG, J. W. & PARK, S. O. 2000 Measurement in the tip vortex roll-up region of an oscillating wing. AIAA J. 38, 1092–1095.

CLEAVER, D. J., WANG, Z., GURSUL, I. & VISBAL, M. R. 2011 Lift enhancement by means of small-amplitude airfoil oscillations at low Reynolds numbers. AIAA J. 49, 2018–2032.

CONNER, M. 1989 High alpha research vehicle program. Photo Number: EC89-0096-226, https://www.nasa.gov/centers/dryden/multimedia/imagegallery/F-18HARV/EC89-0096-226.html

CROUCH, J. D. 2005 Airplane trailing vortices and their control. C. R. Phys. 6, 487–499.

CROW, S.C., 1970 Stability Theory for a Pair of Trailing Vortices AIAA J. 8, 2172-2179.

DELBENDE, I., CHOMAZ, J. & HUERRE, P. 1998 Absolute/convective instabilities in the batchelor vortex: a numerical study of the linear impulse response. J. Fluid Mech. 355, 229–254.

DELBENDE, I. & ROSSI, M. 2005 Nonlinear evolution of a swirling jet instability. Phys. Fluids. 17, 044103.

DEL PINO, C., PARRAS, L., FELLI, M. & FERNANDEZ-FERIA, R. 2013 Structure of trailing vortices: Comparison between particle image velocimetry measurements and theoretical models. Phys. Fluids. 23, 013602.

ECKHOFF, K. S. 1984 A note on the instability of columnar vortices. J. Fluid Mech. 145, 417–421.

FREYMUTH, P. 1966 On transition in a separated laminar boundary layer. J. Fluid Mech. 25, 683-704.

GARMANN, D. J. & VISBAL, M. R. 2014 Unsteady interactions of a wandering streamwise-oriented vortex with a wing. AIAA Paper 2014-2105.

GARMANN, D. J. & VISBAL, M. R. 2015 Interactions of a streamwise-oriented vortex with a finite wing. J. Fluid Mech. 767, 782–810.

GARMANN, D. J. & VISBAL, M. R. 2016a Unsteady evolution of the tip vortex on a stationary and oscillating naca0012 wing. AIAA Paper 2016-0328.

GARMANN, D. J. & VISBAL, M. R. 2016b Further investigations of the tip vortex on an oscillating naca0012 wing. AIAA Paper 2016-4343.

GARMANN, D. J. & VISBAL, M. R. 2017 Analysis of tip vortex near-wake evolution for stationary and oscillating wings. AIAA J. 55, 2686 – 2702.

GERONTAKOS, P. & LEE, T. 2006 Active trailing-edge flap control of oscillating-wing tip vortex. AIAA J. 44, 2746–2754.

GORDNIER, R. E. & VISBAL, M. R. 1999 Numerical simulation of the impingement of a streamwise vortex on a plate. Int. J. of Computational Fluid Dynamics 12(1) 49-66.

GREEN, S. & ACOSTA, A. 1991 Unsteady flow in trailing vortices. J. Fluid Mech. 227, 107-134.

HAMA, F. & NUTANT, J. 1961 Self-induced velocity on a curved vortex. Phys. Fluids. 4, 28.

HAMA, F. 1962 Progressive deformation of a curved vortex filament by its own induction. Phys. Fluids. 5, 1156.

HAMA, F. 1963 Progressive deformation of a perturbed line vortex filament. Phys. Fluids. 6, 526.

HUMMEL, D. 1983 Aerodynamic aspects of formation flight in birds. J. Theor. Biol. 104 (3), 321–347.

HUMMEL, D. 1995 Formation flight as an energy-saving mechanism. Isr. J. Zool. 41 (3), 261–278.

JACQUIN, L. & PANTANO, C. 2002 On the persistence of trailing vortices. J. Fluid Mech. 471, 159–168.

LAWSON, N. J. & WU, J. 1997 Three-dimensional particle image velocimetry: error analysis of stereoscopic techniques. Meas. Sci. Technol. 8, 897–900.

KERSWELL, R. 2002 Elliptical instability. Annu. Rev. Fluid Mech. 34. 83–113.

KLESS, J., AFTOSMIS, M. J., NING, S. A. & NEMEC, M. 2013 Inviscid analysis of extended-formation flight. AIAA J. 51 (7), 1703–1715.

LAMBERT C. & GURSUL, I. 2004 Characteristics of fin buffeting over delta wings. J. Fluids Struct. 9, 307–319.

LEE, T. 2007 Effectiveness of dynamically deflected tab control of a tip vortex. AIAA J. 45, 2994–3002.

LEIBOWICH, S. 1978 The structure of vortex breakdown. Annu. Rev. Fluid Mech. 10. 221–246.

LEIBOWICH, S. & STEWARTSON, K. 1983 A sufficient condition for the instability of columnar vortices. J. Fluid Mech. 126, 335–356.

LISSAMAN, P. B. S. & SCHOLLENBERGER, C. A. 1970 Formation flight of birds. Science 168,1003–1005.

MAY, S. 2015 Vortex. NASA's picture dictionary. http://www.nasa.gov/audience/forstudents/k-4/dictionary/Vortex.html

MAYER, E. W. & POWELL, K. G. 1992 Viscous and inviscid instabilities of a trailing vortex. J. Fluid Mech. 245, 91–114.

McKENNA, C. K., BROSS, M., & ROCKWELL, D. 2017a Structure of a streamwise-oriented vortex incident upon a wing. J. Fluid Mech. 816, 306-330

McKENNA, C. K., FISHMAN, G. & ROCKWELL, D. 2018 Interaction of a trailing vortex with an oscillating wing. Exp. Fluids 59:18.

McKENNA, C. K, & ROCKWELL, D. 2016 Topology of vortex-wing interactions. Exp. Fluids 57:161.

MOORE, D. W. & SAFFMAN, P. G. 1973 Axial flow in laminar trailing vortices. Proc. R. Soc. Lond. A 333, 491–508.

NING, S. A., FLANZER, T. C. & KROO, I. M. 2011 Aerodynamic performance of extended formation flight. J. Aircraft 48 (3), 855-865.

OLENDRARU, C. & SELLIER, A. 2002 Viscous effects in the absolute-convective instability of the batchelor vortex. J. Fluid Mech. 459, 371–396.

PANAGAKOS, A. & LEE, T. 2006 Tip vortex control via an active trailing-edge tab. J. Aircraft 43, 1152–1158.

PERRY, A. & CHONG, M. 2000 Interpretation of flow visualisation. In Flow Visualisation: Techniques and Examples, 1-26.

PRASAD, A. K. 2000 Stereoscopic particle image velocimetry. Exp. Fluids 29, 103–116.

RAMAPRIAN, B. R. & ZHENG, Y. 1998 Near field of the tip vortex behind an oscillating rectangular wing. AIAA J. 36, 1263–1269.

ROCKWELL, D. 1998 Vortex-body interactions. Annu. Rev. Fluid Mech. 30, 199–229.

ROY, C., LEWEKE, T., THOMPSON, M., & HOURIGAN, K. 2011 Experiments on the elliptic instability in vortex pairs with axial core flow. J. Fluid Mech, 677, 383–416.

SANDSTROM, T. 2014 A breakthrough in rotorcraft prediction accuracy using detached eddy simulation. https://www.nas.nasa.gov/SC12/demos/demo1.html
SAVAS, O. 2005 Experimental investigations on wake vortices and their alleviation. C. R. Phys. 6, 415–429.

SCHLICHTING, H. 1951 Saving of power in formation flying. Navy Department Report 239, April.

SPALART, P. R. 1998 Airplane trailing vortices. Annu. Rev. Fluid Mech. 30, 107–138.

THOMAS, C. 2001 Autonomous formation flight program. Photo Number: EC01-0328-4, https://www.nasa.gov/centers/dryden/multimedia/imagegallery/AFF/EC01-0328-4.html

VIOLA, F., ARRATIA, C. & GALLAIRE, F. 2016 Mode selection in trailing vortices: harmonic response of the non-parallel batchelor vortex. J. Fluid Mech. 790, 523–552.

VISBAL, M. R. 2011 Three-dimensional flow structure on a heaving low-aspect-ratio wing. AIAA Paper 2011-219.

WASHBURN, A.E., JENKINS, L.N. & FERMAN, M.A. 1993 Experimental investigation of vortex-fin interaction. AIAA Paper 1993-0050.

WEIMERSKIRCH, H., MARTIN, J., CLERQUIN, Y., ALEXANDRE, P. & JIRASKOVA, S. Energy saving in flight formation. Nature. 413, 697-698.

WEST, G. S. & APELT, C. J. 1982 The effects of tunnel blockage and aspect ratio on the mean flow past a circular cylinder with Reynolds numbers between 104 and 105. J. Fluid Mech. 114, 361–377.

WITTMER, K. S. & DEVENPORT, W. J. 1999 Effects of perpendicular blade-vortex interaction, part1: turbulence structure and development. AIAA J. 37 (7) 805-812.

WOLFE, S., LIN, J. C. & ROCKWELL, D. 1999 Buffeting at the leading-edge of a flat plate due to a streamwise vortex: flow structure and surface pressure loading. J. Fluids Struct. 9, 359–370.

YILMAZ, T. O. & ROCKWELL, D. O. 2010 Three-dimensional flow structure on a maneuvering wing. Exp. Fluids 48, 539–544.

ZANOTTI, A., ERMACORA, M., CAMPANARDI, G. & GIBERTINI, G. 2014 Stereo particle image velocimetry measurements of perpendicular blade-vortex interaction over an oscillating airfoil. Exp. Fluids 55, 1-13.

# APPENDIX A

## SUPPLEMENT TO CHAPTER 2: MONOSCIPIC PIV IMAGING TECHNIQUE: EFFECT OF DOWNSTREAM MIRROR LOCATION ON MEASUREMENTS OF AXIAL VELOCITY DEFICIT AND AXIAL VORTICITY

Monoscopic PIV imaging was achieved by employing a downstream mirror that enabled images to be captured perpendicular to the flow direction and along the upper and lower surfaces of the follower wing when a tandem wing configuration was employed. Sections 2.2.2 and 2.4.1 describe the wing configuration and show the rendered model and schematic of the system; as well as the calibration procedure. This appendix discusses the preliminary investigations that were performed in order to investigate the effect of the downstream mirror location, relative to the position of the wing, on the upstream resultant flow structure. This preliminary investigation utilized SPIV to capture the tip vortex three chords downstream of a stationary wing while the downstream mirror was present and centered directly behind the vortex. The streamwise position of the mirror was varied relative to the laser plane location. The effect of the mirror is insignificant when it is positioned six wing chords downstream of the trailing edge.

Figure A.1 shows cross-sectional cuts of axial velocity deficit $1 - u/U_\infty$ at a streamwise location $x_{LP}/C = 3$ behind the trailing edge of the leader wing. Six different mirror locations $x_M$ are indicated. For the most extreme condition considered, $x_M/C = 1$, severe distortion of the axial velocity defiict is present. Clearly, the upstream influence of the mirror on the developing vortex is apparent. With increasing streamwise distance, however, it is evident that these effects diminish significantly and convergenece is realized at $x_M/C = 6$. At $x_M/C = 8$, the flow structure and peak value of axial velocity of the vortex are equivalent to that of the condition where no mirror is present, $x_M/C = \infty$.

Figure A.2 similarly shows cross-sectional cuts of axial vorticity $\omega_x C/U_\infty$ for the same configuration and under the same conditions as those described in Figure A.1. For all streamwise locations of the mirror, including $x_M/C = 1$, the pattern of axial vorticity remains generally consistent. Convergence of the flow structure is achieved at $x_M/C = 6$.

In general, at extremely small separation distances, such as $x_M/C = 1$, the upstream influence of the mirror is evident. However, the utilization of a downstream mirror has no effect on the upstream flow structure when the distance between the plane of measurement and the mirror is greater than $x_M/C = 6$. In the present expereiments, the distance utilized is $x_M/C = 12$, which is significantly past the point of flow convergence indicated in the foregoing.

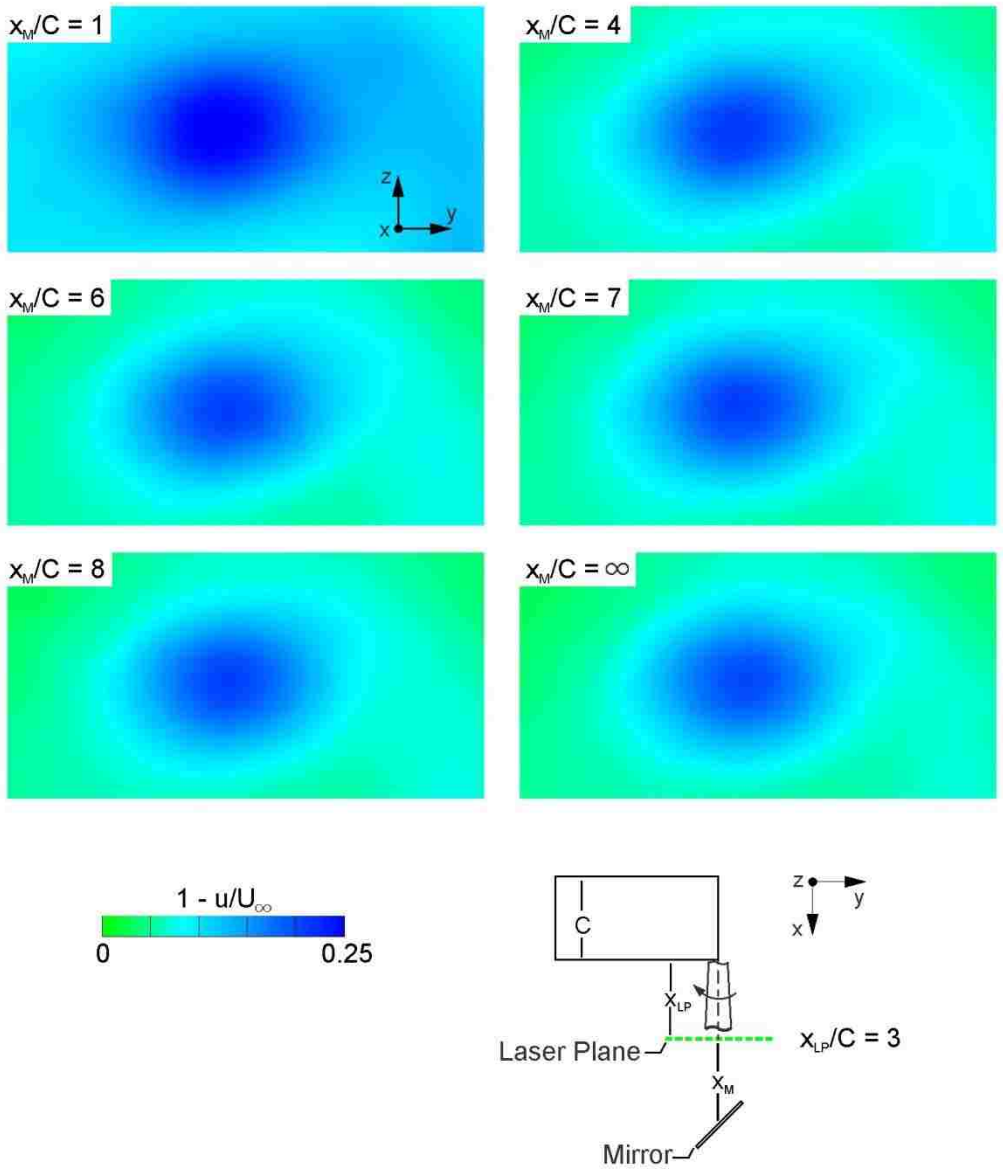


**Figure A.1:** Cross-sectional cuts of axial velocity deficit $1- u/U_\infty$ at a streamwise location $x_{LP}/C = 3$ behind the trailing edge of the leader wing. Six different mirror locations $x_M$ are indicated.

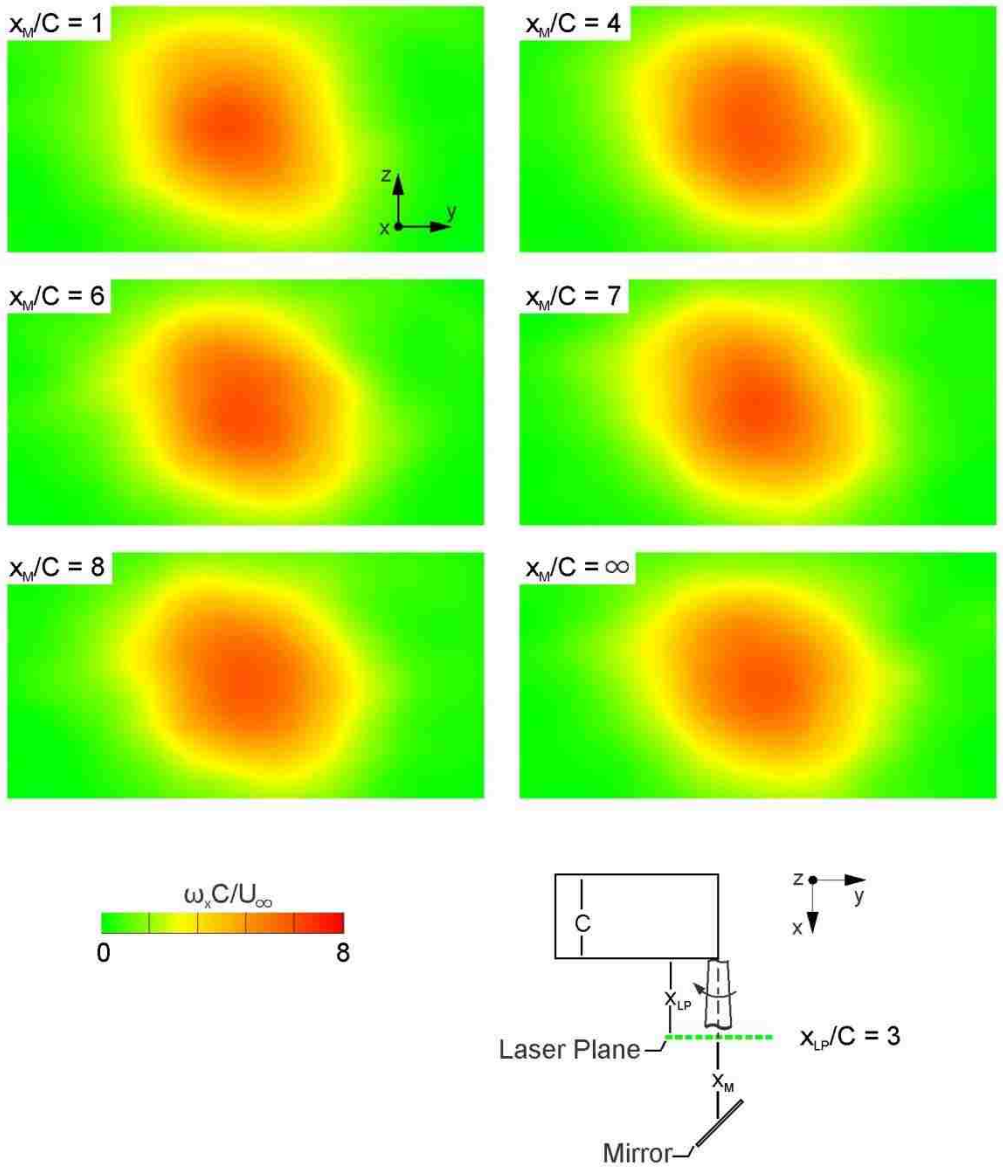


**Figure A.2:** Cross-sectional cuts of axial vorticity $\omega_x C/U_\infty$ at a streamwise location $x_{LP}/C$ = 3 behind the trailing edge of the leader wing. Six different mirror locations $x_M$ are indicated.

# APPENDIX B

## SUPPLEMENT TO CHAPTER 2: DEVELOPMENT OF TIP VORTEX: PATTERNS OF AXIAL VORTICITY OF THE VORTEX FROM THE OPPOSITE WINGTIP

As described in Section 2.2, the leader wing used in these experiments is a rectangular flat plate of aspect ratio $AR = 2$. It is expected that symmetrical undulations of both wingtip vortices will occur over the range of frequencies employed in these experiments. Previous studies have shown the symmetrical nature of the flow structure along oscillating wings at similar values of Strouhal number. Qualitative evidence of this is shown in Calderon et al. (2013), where highly symmetrical volumetric flow patterns of the Q-criterion are observed along a rectangular flat plate and in the near-wake. Additionally, Yilmaz & Rockwell (2010) showed highly symmetrical flow structure, in the form of velocity and vorticity, along a rectangular flat plate undergoing large amplitude heaving motion. The following images are from preliminary studies that confirm the symmetrical nature of the two vortices from a rectangular flat plate undergoing small-amplitude heaving oscillations at several Strouhal numbers.

Figures B.1, B.2 and B.3 show sectional slices of axial vorticity $\omega_x C/U_\infty$ as a function of phase angle $\Phi$ at a streamwise location $x'/C = 0.25$, or one-quarter chord

downstream of the trailing edge of the wing, for values of Strouhal number $St_C$ = 0.08, 0.25 and 0.67, respectively. Both tip vortices, left (blue) and right (red), are shown. Overall, in each of the cases, the trajectories of the two vortices are identical and symmetrical. At $St_C$ = 0.08 and $St_C$ = 0.25, entirely vertical undulations occur in both tip vortices. At all phase angles, the left and right vortices are at equal vertical displacements. At $St_C$ = 0.67, orbital motion is present and the trajectories of the left and right vortices mirror each other. In both cases, the direction of the orbital motion is in the same direction as that of the axial vorticity. That is, the left side vortex trajectory is in the clockwise direction and the right side vortex trajectory is in the counter-clockwise direction. Additionally, the fluctuations in the size of the left and right vortices are equivalent at all Strouhal numbers; however, there are minor discrepancies in the distortions these vortices exhibit at a few phases for Strouhal numbers $St_C$ = 0.25 and 0.67. Lastly, in all cases, the differences in peak values of axial vorticity are within experimental error.

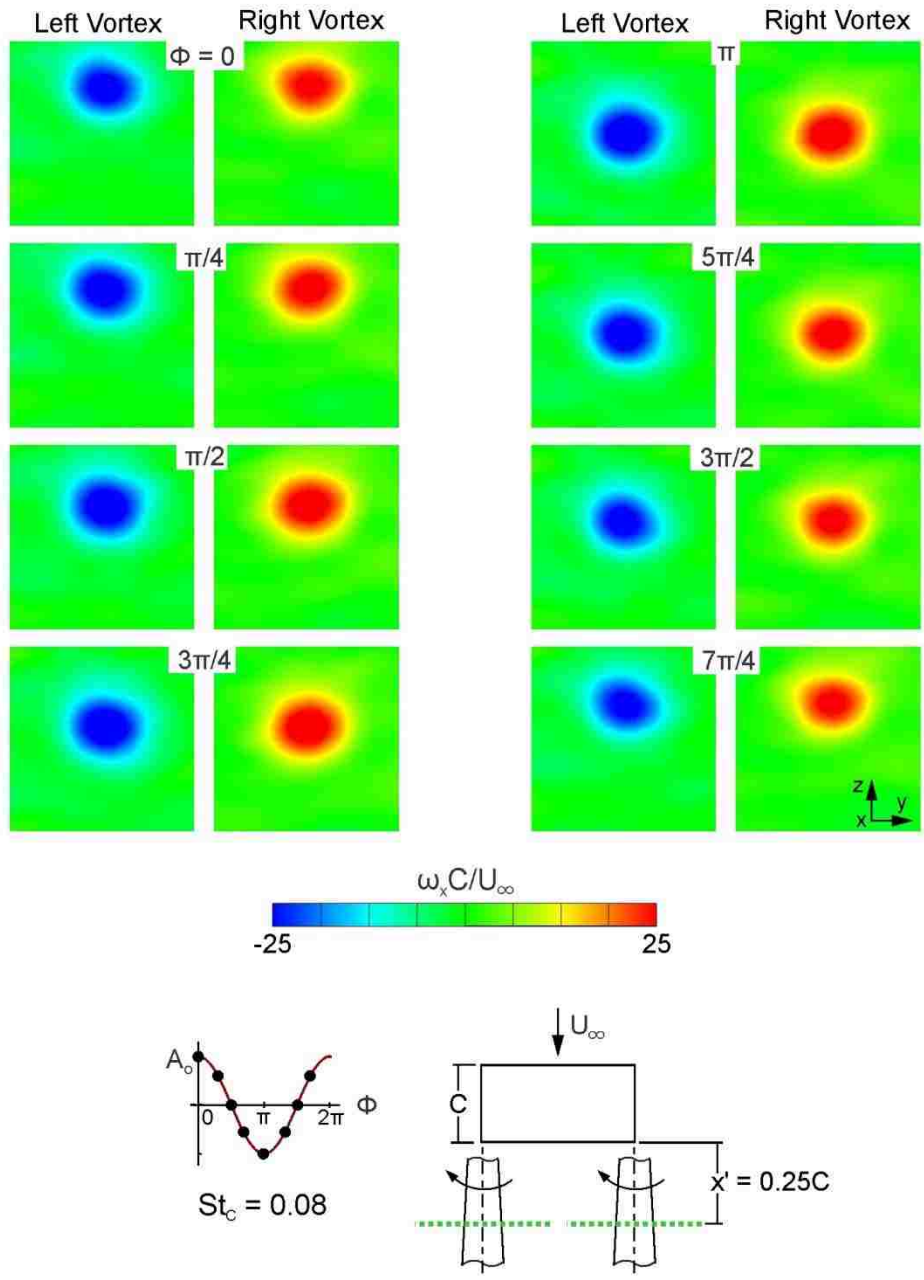


**Figure B.1:** Sectional slices of axial vorticity $\omega_x C/U_\infty$ as a function of phase angle $\Phi$ at a streamwise location $x'/C$ = 0.25, i.e.,one-quarter chord downstream of the trailing edge of the wing, at a Strouhal number $St_C$ = 0.08.

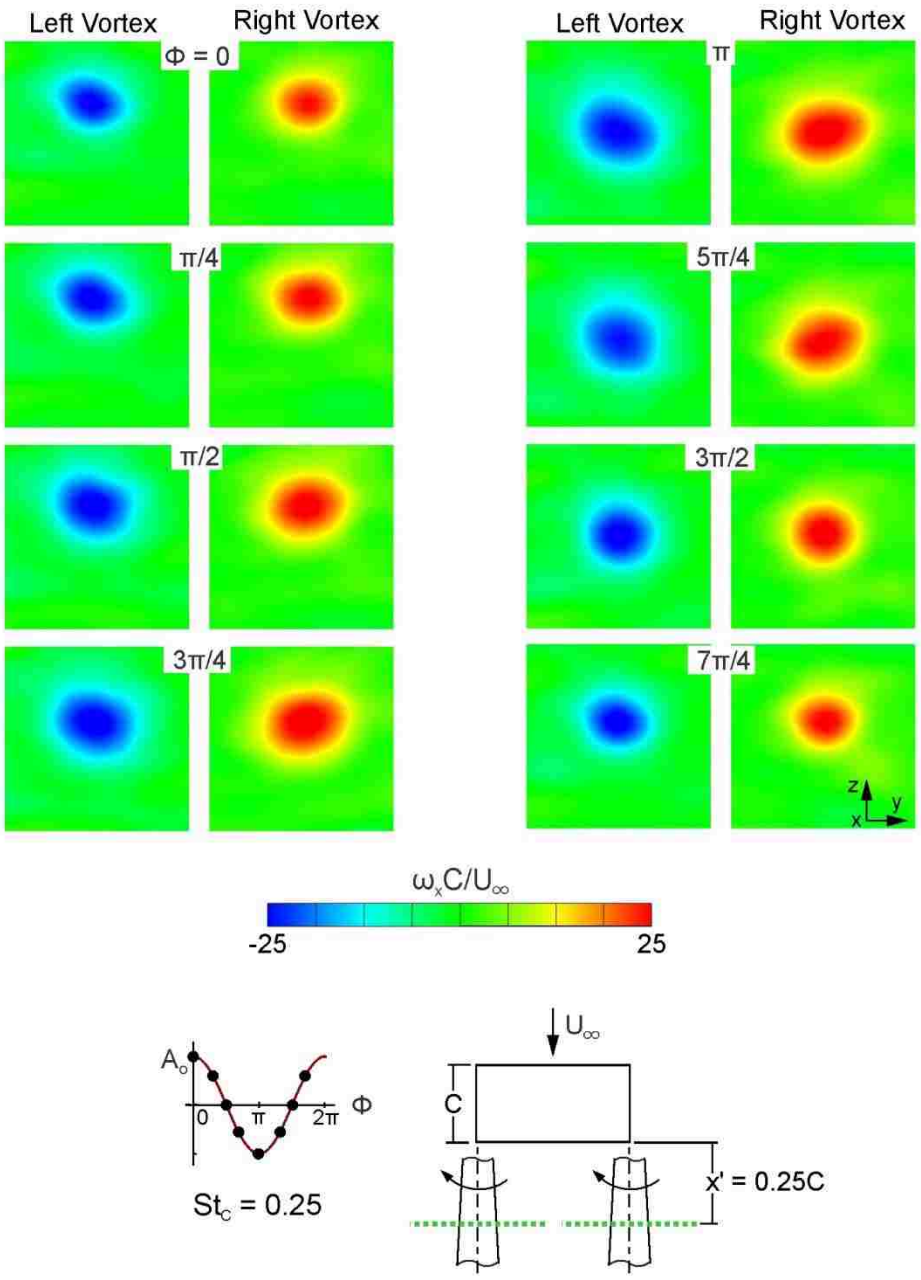


**Figure B.2:** Sectional slices of axial vorticity $\omega_x C/U_\infty$ as a function of phase angle $\Phi$ at a streamwise location $x'/C$ = 0.25, i.e., one-quarter chord downstream of the trailing edge of the wing, at a Strouhal number $St_C$ = 0.25.

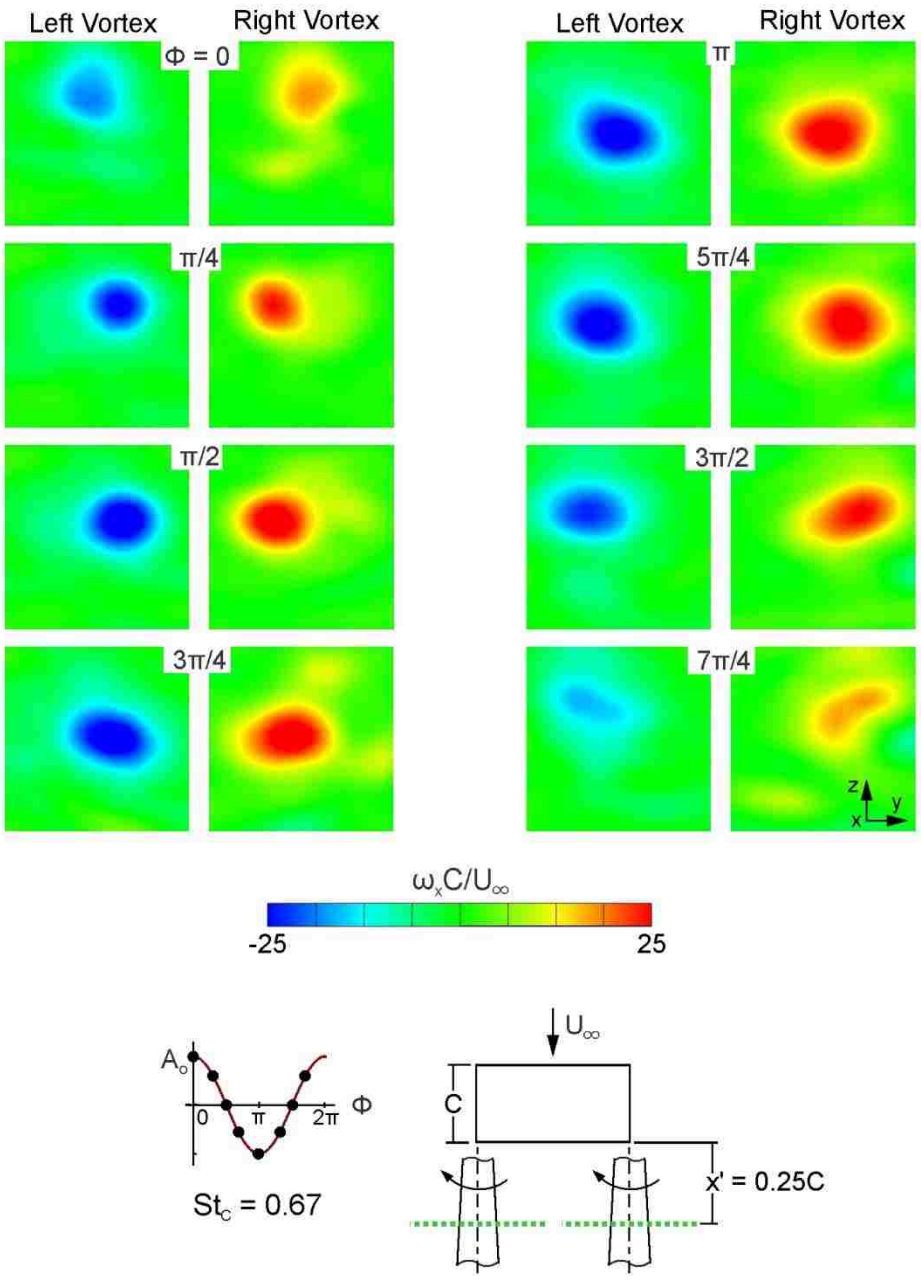


**Figure B.3:** Sectional slices of axial vorticity $\omega_x C/U_\infty$ as a function of phase angle $\Phi$ at a streamwise location $x'/C$ = 0.25, i.e., one-quarter chord downstream of the trailing edge of the wing, at a Strouhal number $St_C$ = 0.67.

# APPENDIX C

## ASSESSING THE POTENTIAL INFLUENCE OF THE CROW INSTABILITY ON THE TRAJECTORY OF THE TRAILING VORTEX

A pair of trailing vortices from an aircraft is known to undergo the long wavelength Crow instability that eventually leads to their dissipation. This instability develops when small displacement perturbations of one, or both, of the vortices gives rise to effects of mutual induction, self-induction and straining on each vortex. These effects cause the instability to grow in space and time. The influence of the Crow instability on a pair of counter-rotating vortices, such as those employed in these studies, must be accounted for when considering how the vortex trajectory evolves. The effect of this instability on the vortex trajectory can be determined from the analysis of Crow (1970) which provides the equations governing this instability.

Crow (1970) shows the amplification rate of the instability for a pair of vortices is dependent on the spacing $b$ between the pair and the circulation $\Gamma$ of each vortex. The analysis shows that the instability will grow by a factor $e$ in a time scale $a^{-1}$. The time scale is described as $a^{-1} = 1.21(2\pi b^2/\Gamma)$. For the experiments under consideration, the vortex spacing $b$ will be taken as the span of the wing, which is 8 inches. The dimensional circulation $\Gamma$ of the vortex is 3.84 $in^2/s$. Employing these values results in a

time scale $a^{-1}$ equal to 126.7 seconds. This is the time scale for which the instability will grow by a factor $e$.

The growth factor $e$ is dependent upon the time scale $a^{-1}$ and the time $t$ that the vortex pair has travelled. The growth factor of the instability is given as $e = exp(t/a^{-1})$. For the vortex pair under consideration, the growth factor is determined for a streamwise travel distance $x'$ of 5 chords, or 20 inches. This value was chosen because it is the largest travel distance of the vortex for which data was acquired. The time $t$ it takes for the vortex to travel this distance is calculated based on the freestream velocity $U_\infty$, such that $t = x'/U_\infty$. This results in a travel time $t$ that is equal to 3.33 seconds. Using the equation described above yields a growth factor of 1.03 over a travel distance of 5 chords of the wing. In essence, this means that the maximally unstable long wavelength Crow instability, which has a length of 8.6$b$, has grown by 3%. For reference, the wavelengths employed in these studies are of 0.75$b$, 2$b$ and 6$b$, so it is doubtful that excitation of the Crow wavelength occurs. Based on the foregoing calculation, it is evident that the influence that the long wavelength Crow instability has on the vortex, especially in comparison the forced oscillations, under consideration is insignificant.

# VITA

Author Greg Fishman was born to Gary and Joni Fishman in Brooklyn, NY on December 13th, 1990. The family moved to Manalapan, NJ when Greg was 1 year old, where he was raised. He will be marrying Nicole Beletz in August 2018. In May 2013, he graduated cum laude with his Bachelor of Science degree in Mechanical Engineering from Lehigh University. He continued his studies at Lehigh University in September 2013 to pursue his Ph.D. in Mechanical Engineering. During his doctoral study at Lehigh University, he worked as a teaching assistant in various courses and as a researcher in Dr. Donald Rockwell's fluids group. He received his Master of Engineering degree in Mechanical Engineering in May 2015. He has given several talks at scientific conferences and has published the following journal articles:

FISHMAN, G., WOLFINGER, M. & ROCKWELL, D. 2017 The structure of a trailing vortex from a perturbed wing. J. Fluid Mech. 824, 701-721.

FISHMAN, G. & ROCKWELL, D. 2018 Onset of orbital motion of a trailing vortex from an oscillating wing. J. Fluid Mech. Under review.

FISHMAN, G., MCKENNA, C. & ROCKWELL, D. 2018 Interaction of a perturbed vortex with a wing. In preparation for submission.

McKENNA, C. K., FISHMAN, G. & ROCKWELL, D. 2018 Interaction of a trailing vortex with an oscillating wing. Exp. Fluids 59:18.